Declaration

The work described in this thesis was undertaken at the University of Sheffield, UK between October 2009 and November 2011, and at the Institute of Materials Research and Engineering (IMRE), A*STAR, Singapore between December 2011 and September 2013, under the supervision of Professor G. J. Leggett and Doctor K. S. L. Chong. Unless otherwise stated, it is the work of the author and has not been submitted in whole or any other part for any other degree at this or any other institute.

Signature: 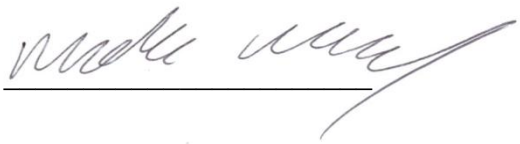

Mark Moxey September 2013

Acknowledgements

First of all I would like to thank my university supervisor, Professor Graham Leggett for his excellent guidance and support throughout my post-graduate studies. He has been a limitless pool of knowledge, from which I have learnt a lot. The continued support and encouragement that I received while on attachment in Singapore has been tremendous.

I would like to thank my co-supervisor, Doctor Karen Chong for her excellent support throughout my time at A*STAR. I much appreciate the level of freedom that she gave to carry out my research, offering advice and guidance when I needed it. I really enjoyed my time working in Singapore, which is a testament to her supervision.

I would like to thank all the past and present members of the Leggett group. Particular appreciation to: Dr Rob Ducker for his enthusiasm and experience, but mostly for his BBQ's and home brewed beer; Dr Claire R. Hurley for her help and training to use the XPS; Dr Shahrul Alang Ahmad for her advice and expertise with photocleavable protecting groups; Dr Osama el Zubir for his continued advice and extensive knowledge of almost everything; Dr Getachew Tizazu for his advice on using titanium films as well as his often quirky use of the English language; and Dr Zhenyu Zhang (AKA Jason) for his friction and diffusion work, i.e. finding a use for my "fancy" polymer patterns.

Dr Andrew Morse (Morsey!!) is thanked for his advice on ATRP and for being a general LAD. Dr Jennifer Ball is thanked for her support and advice with all things regarding organic synthesis.

I would like to thank the present members of the NIL group at IMRE. Particularly, Lee Yeong Yuh, for his help and advice and the countless number of favours that he did for me.

Dr Michael Stenbaek Schmidt (AKA Chet Masterson) is thanked for all the good times, memorable times and mostly drunken times spent whilst "working" in Singapore. Oh and some help with the RIE blah blah blah… The wolfpack and icepack are thanked also.

The lovely Tiffany Celice is thanked for her fantastic support and for putting up with me in the last few stressful months – she deserves a medal.

Lastly and most importantly I would like to thank my mother to whom this thesis is dedicated to. An amazing woman, whom I love so much, who as a single parent raised me to become the man I am today. Thank you Mum.

Publications

"Photocatalytic Nanolithography of Self-Assembled Monolayers and Proteins" Ehtsham Ul-Haq, Samson Patole, Mark Moxey, Esther Amstad, Cvetelin Vasilev, C. Neil Hunter, Graham J. Leggett, Nicholas D. Spencer, and Nicholas Hendrik Williams. *Accepted into ACS Nano.*

"Mechanical Properties of Nanostructured Polymer Brushes" Zhenyu Zhang, Mark Moxey, Abdullah Alswieleh, Steven P. Armes, Andrew L. Lewis, Mark Geoghegan, and Graham Leggett. *Manuscript in preparation.*

Oral presentations at conferences

"Nanostructured Arrays of Optically Active Proteins Assembled on Chemically Patterned Surfaces" Mark Moxey, Graham J. Leggett, Karen SL Chong. 7th International Conference on Materials for Advanced Technologies, Materials Research Society, 30th – 5th June 2013, Suntec SINGAPORE.

Poster presentations at conferences

"Nanostructured Arrays of Optically Active Proteins Assembled on Chemically Patterned Surfaces" Mark Moxey, Graham J. Leggett, Karen SL Chong. The Japan Society of Applied Physics – Materials Research Society Joint Symposia, 16th – 20th September 2013, Doshisha University, Kyoto, JAPAN.

Abstract

The integration of top-down (lithographic) and bottom-up (chemical synthesis) fabrication and the ability to fabricate over macroscopic areas, are both major challenges in nanoscience. Overcoming these challenges would offer significant advances in biological sciences and applications. In the present work, we investigate how large area nano-lithographic techniques, interference lithography and nanoimprint lithography, can be combined with the self-assembly of organic molecules to produce nanostructured functional arrays over macroscopic areas.

Organic films containing photocleavable protecting groups have been used as resists and patterned by photolithographic methods. Investigations into photodeprotection at 244 nm and 325 nm have been conducted. Contact angle analysis and X-ray photoelectron spectroscopy (XPS) confirmed that photodeprotection occurred much faster at 244 nm compared to 325 nm. A non-fouling polymer has been grown from exposed regions of the photo-reactive film by surface initiated atom transfer radical polymerisation (SI-ATRP). Mask patterns of the polymer have been fabricated and were observed to pattern adsorbed proteins. Interference lithography has fabricated periodic arrays over a macroscopic area by irradiating at 244 nm. Atomic force microscopy (AFM) confirmed an array of polymer features ca. 100 nm in width. Scanning near-field photolithography (SNP) has fabricated a multifunctional pattern; a pattern of 8 lines with varied exposure and a pattern of 6 lines with varied line width. AFM confirmed an increase in polymer line height with increasing exposure and no change in polymer line height with varied line width between 500 nm and 800 nm.

Nanoimprint lithography (NIL) has been used to fabricate a chemically patterned surface for the patterning of biological molecules over a macroscopic area. An imprinted film of poly(methyl methacrylate) PMMA resist has been etched to remove the residual layer and used to direct the adsorption of (3-aminopropyl)triethoxysilane (APTES) and 2-[Methoxy(polyethyleneoxy)propyl]-trichlorosilane (PEG-silane) onto the substrate. Fluorescence microscopy confirmed protein adsorption with a high degree of control over the proteins spatial organisation on micro-scale patterns. AFM confirmed the fabrication of an array of APTES dots within a film of PEG-silane with diameters of 70 nm, and the subsequent attachment of streptavidin through bioconjugation with biotin.

Finally both photolithographic methods and NIL have fabricated arrays of TiO_2 that have been demonstrated as switchable platforms for protein adsorption and protein degradation.

Wet and dry etching methods were used to form TiO_2 structures that, in combination with an adsorbed film of PEG-silane, adsorbed protein with control over the spatial organisation of the protein. Fluorescence microscopy suggested degradation of the proteins following UV exposure and then the re-adsorption of a second protein following emersion in a protein solution. An array pattern fabricated by NIL has demonstrated as many as 10 cycles of protein adsorption and protein degradation without exhibiting a change in fluorescence or non-specific adsorption.

Contents

List of Tables

List of Figures

Abbreviations

AFM – Atomic force microscopy

APS – Aminopropylsiloxane

APTES – (3-aminopropyl)triethoxysilane

BIBB – Bromoisobutyryl bromide

CA – Contact angle

CMPS – 4-chloromethylphenylsiloxane

Cy3, Cy5 – Cyanine dyes

DNA – Deoxyribonucleic acid

DOF – Depth of focus

DPN – Dip-pen nanolithography

EBL – Electron beam lithography

EDC – N-(3-Dimethylaminopropyl)-N-ethylcarbodiimide hydrochloride

ESEM – Environmental scanning electron microscopy

ETL – Edge-transfer lithography

EUV-IL – Extreme ultra-violet interference lithography

FFM – Friction force microscopy

FIBL – Focused ion beam lithography

FITC – Fluorescein isothiocyanate

IgG – Immunoglobulin G

IL – Interference lithography

ITRS – International Technology Roadmap for Semiconductors

NIL – Nanoimprint lithography

NPPOC – Nitrophenylpropyloxycarbonyl

NPPOC-silane – {N-[2-(2-Nitrophenyl)propan-1-oxycarbonyl]-3-aminopropyl}-triethoxysilane

NTA – Nitrilotriacetic acid

ODPA – Octadecylphosphonic acid

ODT – 1-octadecanethiol

OEG – Oligo(ethylene glycol)

OEGMA – Oligo(ethylene glycol)methyl methacrylate

PDMS – Polydimethylsiloxane

PEG – Poly(ethylene glycol)

PEG-silane – 2-[Methoxy(polyethyleneoxy)propyl]-trichlorosilane

PMMA – Poly(methyl methacrylate)

pMPC – Poly(methacryloyloxyethyl phosphorylcholine)

R2RNIL – Roll to roll nanoimprint lithography

RIE – Reactive ion etch

SAM – Self assembled monolayer

SE – Secondary electron

SEI – Secondary electron imaging

SEM – Scanning electron microscopy

SI-ATRP – Surface initiated atom transfer radical polymerisation

SIMS – Secondary ion mass spectrometry

SNOM – Scanning near-field optical microscope

SNP – Scanning near-field photolithography

SOL – Super-oscillatory lens

SPL – Scanning probe lithography

SPM – Scanning probe microscopy

SSIL – Step and stamp imprint lithography

STED – Stimulated emission depletion microscopy

STM – Scanning tunnelling microscopy

STORM – Stochastic optical reconstruction microscopy

TEA – Triethylamine

TEM – Transmission electron microscopy

T-NIL – Thermal nanoimprint lithography

UV-NIL – Ultra-violet nanoimprint lithography

WGA – Wheat germ agglutinin

XPS – X-ray photoelectron spectroscopy

μCP – Microcontact printing

Chapter One

1 Introduction

1.1 Introduction to Nanofabrication

Nanofabrication refers to a collection of technologies for the fabrication of functional structures with one or more active dimensions smaller than 100 nm[1-4]. Spurred on by the semiconductor industry, sophisticated lithographic techniques have improved and will continue to improve as a result of the large scale commercialisation of products requiring nanofabrication[4]. Commercial processes rely heavily on photolithographic methods, sometimes referred to as "conventional methods". In research laboratories there is a plethora of unconventional lithographic techniques that have yet to prove themselves suitable for commercial large-scale production, although increasingly, the distinction between conventional and unconventional is becoming less distinct. Although conventional methods serve their purpose very well they are restricted to the fabrication of very specific types of structures. Moreover their ability to serve a wider field of applications is constrained by their relative high cost and by the limited availability of the expensive infrastructure of which they depend.

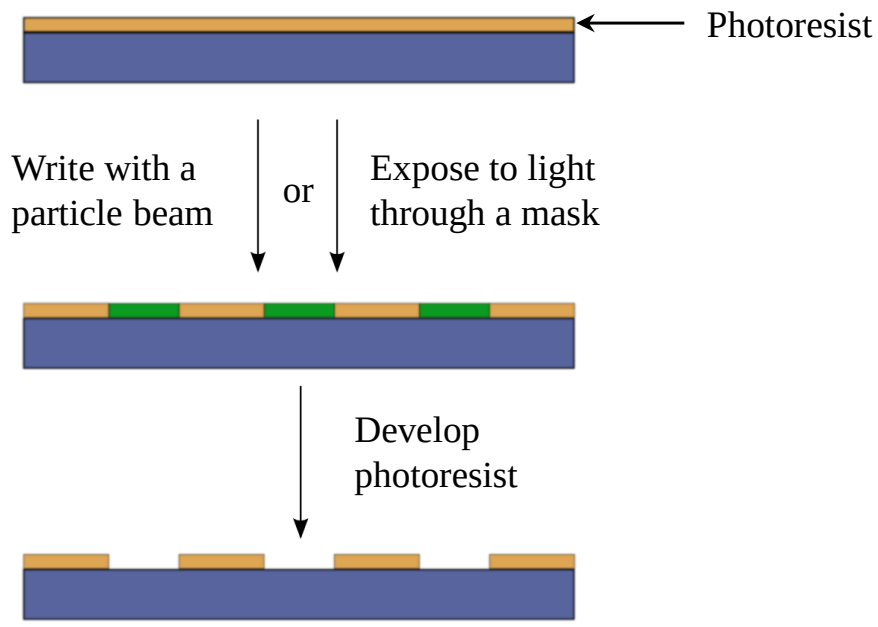

Figure 1.1: Schematic of a typical 3 step photolithographic process

Unconventional methods, on the other hand, can often be cheaper and easier to use. They also offer suitability for a wider range of applications, in particular biological ones. The methods used to produce nanoscale structures are commonly categorised as either "top-down" or "bottom-up". The top-down approach uses various lithographic techniques to form patterns on a substrate. This approach includes serial and parallel techniques and is typically in two-

dimensions. A typical lithographic process shown in Figure 1.1 consists of three successive steps: (i) coating a substrate with a photo-sensitive polymer layer (resist), (ii) exposing the resist to light, electrons or an ion beam, (iii) developing the resist in a suitable chemical[3]. Conventional methods are exclusively top-down. The bottom-up approach uses specific interactions between molecules or colloids to assemble discrete nanoscale structures in two and three dimensions. Methods also exist that combine both the top-down and bottom-up approaches including those involving novel resists such as self assembled monolayers (SAMs).

Nanofabrication is having an increasing impact within the biological sciences[5]. The ability to pattern biological molecules such as nucleic acids and proteins on sub-micron length scales is important for producing biodiagnostic devices. Within the field of biodiagnostics there is currently a need for a more practical, robust and highly sensitive and selective biodevice. Nanofabrication can offer significant advantages over conventional diagnostic systems including increased sensitivity, selectivity and practicality[6]. The advantages of miniaturisation and multiplexing have already been realised for the analysis of nucleic acids[7]. However, advancements in the miniaturisation of protein analysis have been much slower. Patterning specific proteins is important for many applications from the development of biosensors for the detection and diagnosis of diseases[8], to investigating the fundamental properties of individual proteins such as protein-receptor interactions[9], protein folding and unfolding[10], and molecular motors[11]. However, controlling the spatial positioning of proteins is challenging. Proteins can adhere to most surfaces because they are able to undergo many conformational changes, entropically driven by the minimisation of the interfacial free energy. In order to confine proteins to desired regions on a surface, non-specific adsorption must be controlled. The most widely reported method for resisting protein adsorption is by chemically modifying a surface with ethylene glycol (EG) or poly(ethylene glycol) (PEG)[12-15]. Other materials have also been shown to limit protein adsorption, for instance other hydrophilic polymers including polysaccharides[16] and polyamides[17], and zwitterionic polymers such as poly(methacryloyloxyethyl phosphorylcholine) (pMPC)[18, 19]. The ability of the polyhydrophilic and polyzwitterionic materials to resist the adsorption of proteins is hypothesised to be strongly linked with a hydration layer that resides on top and penetrates into the material[20]. Strong water-polymer interactions exist that lead to a strongly solvated surface. While the adsorption of proteins is entropically favoured, the enthalpic cost of displacement of surface bound water renders the adsorption of protein unfavourable. As well

as controlling spatial confinement, it is also important to retain the proteins functionality when immobilised onto a surface, whether the function is sensing, mechanical, catalytic, or signalling. Factors including hydrophobic, electrostatic and Van Der Waals interactions all contribute to the complicated behaviour observed when proteins adsorb to at surfaces. A variety of immobilisation techniques have been developed, which are mainly based on physical, covalent, or bioaffinity mechanisms[21]. However, some degree of conformational change is inevitable as the protein interacts with an interface.

1.2 Photolithography

The term photolithography, which literally means *light-stone-writing* in Greek, refers to a process where photons are used to induce chemical transformations in a material. Photolithography is the method of choice for the manufacture of integrated circuits[22].

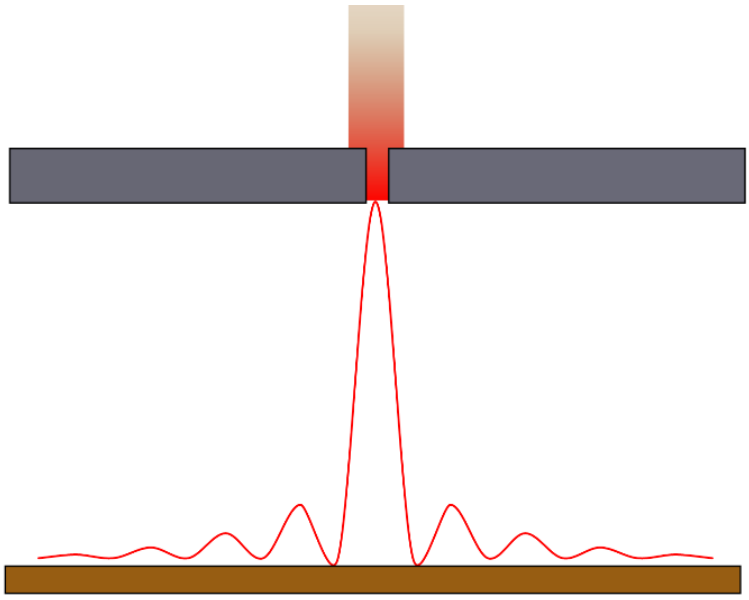

Figure 1.2: Schematic representing the diffraction of light passing through a single aperture

In the mass production of integrated circuits typically a photoresist is exposed to UV light through a quartz plate that is coated with an opaque material such as chromium. In transparent regions light passes through the mask and modifies the resist. A lens is used to form an image of the mask on the photoresist with reduced dimensions. The photoresist is altered chemically by the light and can be developed in an appropriate solution to afford the desired pattern[23]. On exposure to UV light the photoresist can either become cross-linked, making it more insoluble (negative photoresist), or chemically altered, making it more

soluble (positive photoresist). The resolution of photolithography is limited by the diffraction of light (Figure 1.2), defined by the Rayleigh criterion:

$$\mathrm{r} = \frac{K1\lambda}{n.sin\theta} \quad (1)$$

where K_1 is an empirical parameter that depends on the experimental conditions (commonly 0.61[24]), λ is the wavelength of light used and n.sinθ is the numerical aperture (NA). Another important parameter in photolithography the depth of focus:

$$\mathrm{DOF} = \frac{K_2\lambda}{NA^2} \quad (2)$$

In high volume manufacturing, the parameters K_1 and K_2 are typically 0.6 or greater. However values of 0.5 can be achieved[25]. This means that practically, the maximum resolution is approximately equal to half the wavelength of light. The Rayleigh criterion (1) dictates that the resolution can be reduced by increasing the NA or decreasing the wavelength. However equation (2) shows that by increasing NA leads to a dramatically reduction in the DOF which can become problematic. Due to an ever increasing demand for smaller circuits the semiconductor industry has made every effort to follow Moore's Law (the number of transistors on an integrated circuit will double approx. every 2 years). Reducing the wavelength has been one of the main methods for this. Previously the industry had worked with wavelengths as large as 450 nm, but this has been decreased down to deep UV at 248 nm, 193 nm[26] and 157 nm[27]. There are even possibilities of going even further down the spectrum to soft X-rays (also known as extreme UV) at 13.4 nm[22, 25, 28]. As well as reducing the wavelength new mask technologies such as phase-shifting masks have been employed[29]. These masks have transparent regions of different thicknesses necessary to induce a phase-shift in the light as it is transmitted. Destructive interference between waves from adjacent apertures cancels some diffraction effects improving the contrast and ultimately the resolution of the features recoded into a resist.

Commonly, the resists used in photolithography are in the form of polymer films that are spin-coated onto surfaces. However, monomolecular films can be achieved with SAMs, which offer a much thinner and flatter resist layer to spin-coated polymer films. Additionally, the molecular film can act as a foundation for further chemical transformations of the surface,

facilitating the integration of top-down and bottom-up fabrication. The use of SAMs in optical lithography is well studied[24, 30-32]. Certain monolayers will undergo chemical transformations when exposed to light of the correct wavelength. Monolayers of strongly bonded alkylthiolates on gold can be oxidised to weakly bonded alkyl sulfonates by exposure to UV light. The sulfonates may be removed by rinsing with ethanol, to expose the gold substrate, or are replaced by a second thiol in a solution phase process.

$$Au - SR + \frac{3}{2}O_2 + e^- \rightarrow Au + RSO_3^-$$

There has been interest in patterning monolayers of alkyl silanes on silicon dioxide surface too[32]. Alkylsilanes are more stable than alkylsulfonates and require irradiation with deep-UV to remove them from the SiO_2 surface[33, 34]. The stability of the Si-C bond has allowed for a variety of chemical transformations of the alkylsilane monolayers. It has been shown that when SAMs of 4-chloromethylphenylsiloxane are exposed to UV light the C-Cl bond is cleaved and the carbon radical is oxidised to an aldehyde, further exposure will yield a carboxylic acid as shown in Figure 1.3[35].

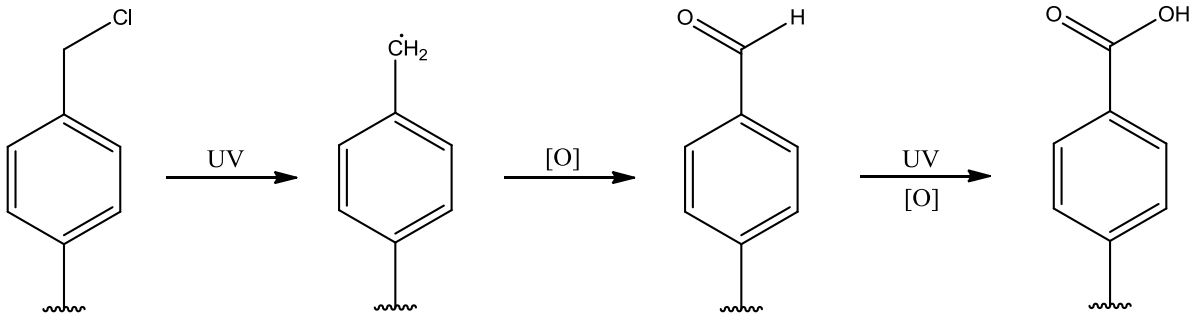

Figure 1.3: Schematic showing oxidation of the terminal alkylhalide group, initiated by exposure to UV light.

Organic chemistry has provided various other photochemical reactions that have proved useful for lithography. One example is the so called Photo-Fries Rearrangement, in which an aryl ester is transformed into a hydroxylketone when exposed to UV light[36]. The hydroxyl group can act as a nucleophile and be further derivatised. Another example utilises a common strategy employed in the synthesis of peptides, in which o-nitrobenzyl derivatives are used as photocleavable protecting groups that can be removed by irradiation with UV light[37]. Fodor *et al* was first to demonstrate the combination of such a strategy with solid-phase chemistry and photolithographic techniques to develop what they called “light-directed chemical

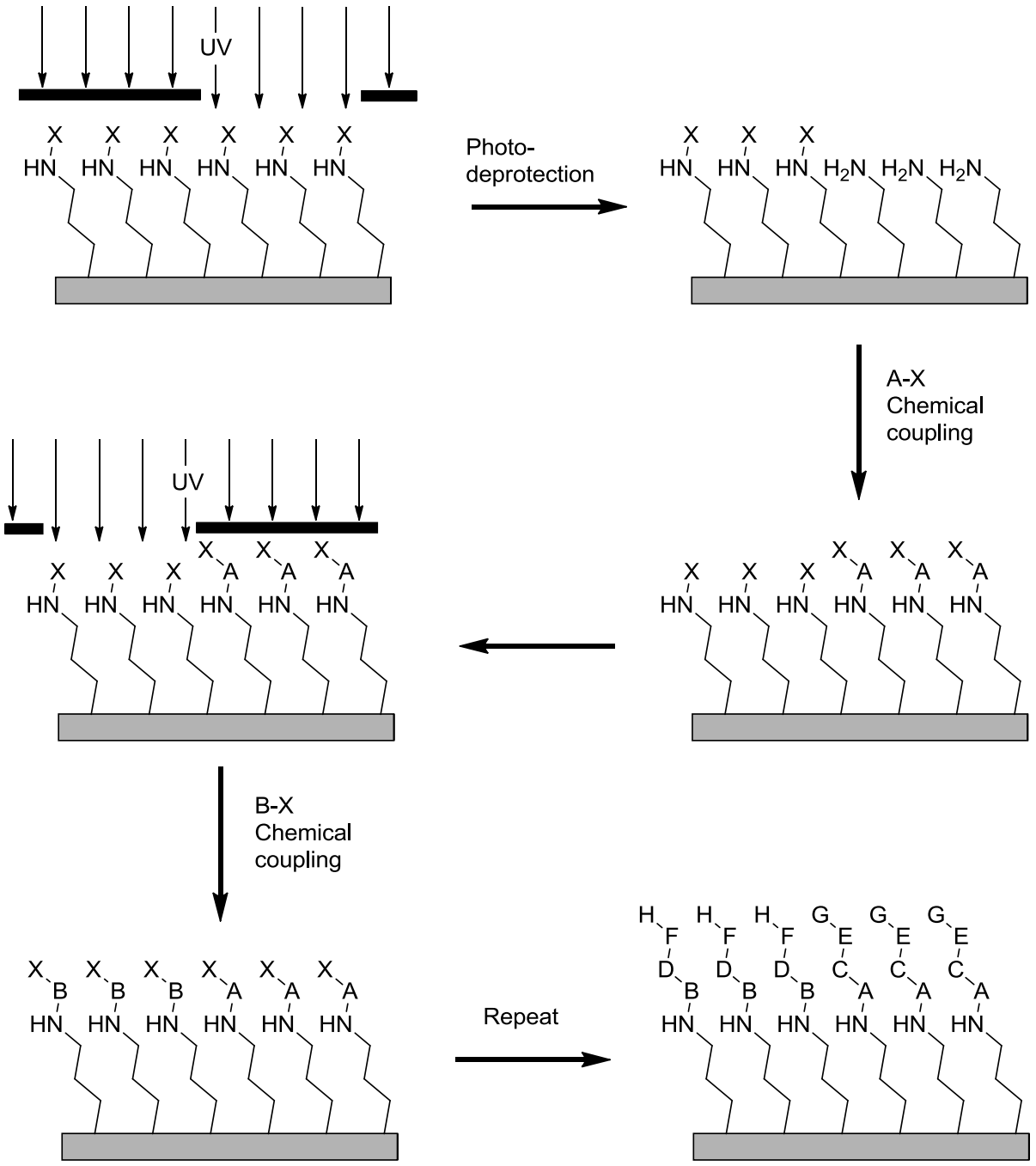

Figure 1.4: Process steps laid out by Fodor et al[38], illustrating the method of light-directed chemical synthesis.

synthesis"[38]. Figure 1.4 shows the basic concept of light-directed chemical synthesis. An amine surface blocked with a photolabile protecting group X, is selectively exposed to UV light using a mask leading to the removal of the protecting group X within the exposed regions. The subsequent surface of 'un-blocked' amine can be coupled to chemical A-X, which itself has a reactive site blocked by a photolabile protecting group. A second UV exposed of the surface using a different mask, enables deprotection of a different region of

the substrate, which in turn can be coupled to chemical B-X. Additional cycles of photo-deprotection and coupling are carried out to produce the desired product.

Interference Lithography

There is a need to develop low cost methods for mass producing nano-structures over macroscopic areas[39, 40]. One promising technique is interference lithography (IL)[41, 42], also referred to as holographic lithography or interferometric lithography. When two or more coherent optical beams interfere with each other, a sinusoidal pattern of intensity results, which can be used to expose a photoresist or photosensitive monolayer. Two common IL configurations[43, 44] are shown in Figure 1.5. The Lloyd's mirror, (a) is very simple and uses inexpensive components. However it is not suitable for lasers with a low transverse coherence due to the two halves of the beam not being equivalent; in some circumstances it will not produce a clear interference pattern. The alternate configuration (b) uses a beam splitter, which makes it a little more complex.

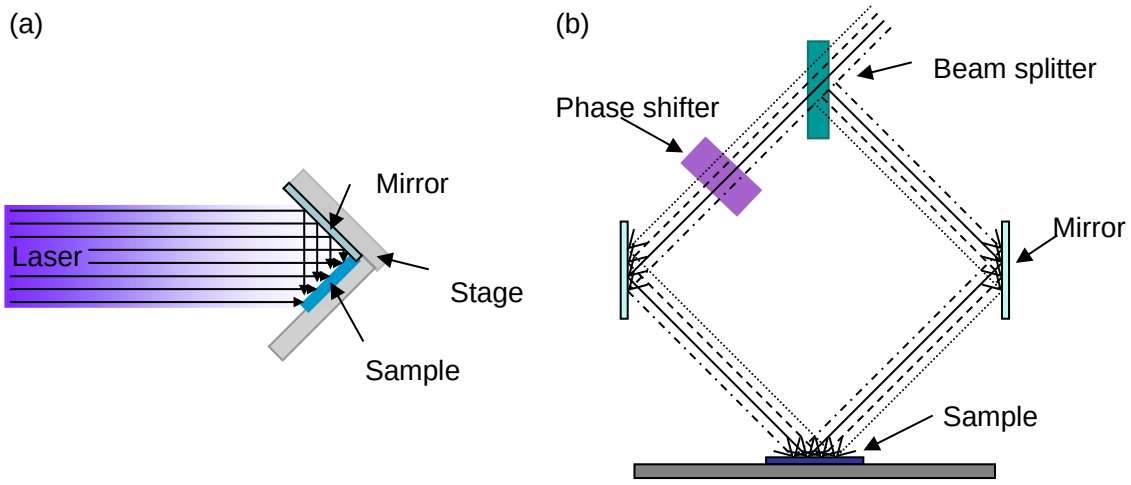

Figure 1.5: Schematic of two common IL set-ups.

The two beams then follow different paths of different lengths; in this case one beam passes through a phase shifter, before the beams are realigned over the sample. This method allows for lasers with a lower transverse coherence to be used because, at the point where the beams meet, each area of the beam is overlapped with the corresponding same area of the second beam. A single exposure using a two-beam interferometer yields parallel lines. However, a range of patterns is accessible by varying the number of beams or exposures. The simplest form of IL is two-beam IL, which produces a grating. The period of which, d, is expressed in

equation (3) where λ is the wavelength of light used, n is the refractive index of the medium (in most cases the medium is air where n = 1) and θ is the angle at which the two beams interfere:

$$d = \frac{\lambda}{2n \cdot \sin(\theta)} \qquad (3)$$

IL can be used to make periodic patterns from the micro scale down to the sub-50 nm scale[45, 46]. The resolution can be simply tuned by adjusting the angle θ at which the beams interact or by changing the wavelength of the beams. The ultimate resolution of IL is limited by diffraction like most optical lithography. However, skilful selection of development conditions and the use of new technologies such as immersion lithography enable very small structures to be formed. By immersing the sample in a medium with a refractive index greater than air *cf* 1 a smaller resolution can be obtained. At 193 nm water has a refractive index of 1.44 and is commonly used in immersion IL. By simply introducing a drop of water to the sample and then by placing a prism on top a thin film of water is produced which covers the sample and effectively reduces the period of the interference pattern. It has been shown that immersion IL can produce gratings of 22 nm half-pitch by using a 157 nm laser and a hydrocarbon based fluid with a refractive index of 1.82[46].

Scanning Near-Field Photolithography

Scanning near-field photolithography (SNP) refers to the process of surface patterning using near-field optical methods. SNP can be achieved by coupling a UV laser to a scanning near-field optical microscope (SNOM) to expose a SAM of photo-reactive molecules to initiate a chemical reaction[47]. Monolayers of alkylthiols on gold have been patterned by SNP. The probe is traced over the sample exposing the absorbate molecules to UV light, which oxidises them to alkylsulfonates. Subsequent immersion in a contrasting thiol solution results in the alkylsulfonates being displaced by the alkyl thiols in solution. This process has been shown to be influenced by the grain-size of the underlying gold[24]. Coupling a SNOM probe to a frequency-doubled ion argon laser (emitting at a wavelength of 244 nm) resolutions of 20 nm have been shown to be readily repeatable[47] and a resolution as small as 9 nm has been

produced[48]. The patterned alkylthiol SAMs have also been shown to be useful resists for nanoscale etching of metals. Instead of immersion in a thiol solution the samples are placed in an etchant. The etchant displaces the alkylsulfonates and erodes the underlying metal[30, 49]. The SNP technique can be applied to other monolayers for example, it has been show to oxidise 4-chloromethylphenylsiloxane (CMPS) monolayers to carboxylic acids[35] (Figure 1.3). One drawback to SNP is the slow writing speeds and therefore impractical for producing nano-patterns over a microscopic area. The development of the "Millipede" parallel cantilever device has provided a model for addressing the intrinsically serial nature of local probe techniques[50]. Adaptation of millipede-style parallisation has enabled the development of a prototype "Snomipede" which consists of 16 probes scanning in parallel[51]. The snomipede was shown to write lines in photoresist in parallel with widths as small as 70 nm.

1.3 Particle Beam Lithography

Electron Beam Lithography (EBL)

EBL uses a beam of electrons to scan across a surface in order to pattern a resist layer in either a positive or negative fashion. EBL is able to achieve high resolutions relative to photolithography because the diffraction limit for electrons is very much smaller than it is for light. The resolution of EBL is limited by the high energy secondary electrons and by the scattering of electrons within the resist and substrate causing a 'plume' of excitation that is larger than the diffraction limit for electrons, although much smaller than the diffraction limit for UV light. In most cases edge roughness dictates the resolution limit of ELB to be >10 nm[52]. Due to the effects of scattering of electrons, resist technology is important for producing sub-100 nm resolution. The resist should be very thin and highly sensitive to the electron beam to reduce the volume of scattering [53]. Although EBL can produce very high resolutions it is expensive and has a very low throughput because of its serial nature. Thus EBL is not a practical technique for large scale nanofabrication, but is instead used to fabricate the photo-masks used in conventional photolithography as well as being a valuable lithographic tool in lab-based research.

Focused Ion Beam Lithography (FIBL)

FIBL is analogous to EBL in operation, but uses a beam of ions instead of electrons to pattern a sample. Ions are much heavier than electrons and consequently FIBL has several

advantages over EBL. The ions collide with the sample with more momentum and thus can pattern directly into hard materials such as semiconductors and metals as opposed to EBL which can only pattern soft materials. There is a significant reduction in scattering compared with EBL, therefore sub-100nm resolutions are easier and faster to produce. Sub-10 nm resolution is attainable[54]. The FIBL process can also be referred to as "direct writing" and incorporates a collection of approaches, including milling (removing the material from the substrate), implantation (changing the properties of the substrate) and ion-induced deposition (addition of material onto the substrate). The ability of FIBL to add or remove material from a predefined area in a controllable manner permits that high-precision and complex 3D nanostructures can be fabricated[55].

1.4 Dip-Pen Nanolithography

Dip pen nanolithography (DPN) is a direct-scanning probe based lithography that uses an AFM tip to write chemicals onto a surface in a style analogous to writing with a quill and ink on paper. DPN was first introduced in 1999 by Mirkin and his colleagues. They demonstrated the writing of patterns of alkanethiols on a gold thin film with resolutions ranging from 1 μm to 30 nm[56]. The transfer of molecules to the surface relies on a liquid meniscus forming between the tip and the surface; capillary forces then transport the molecules onto the surface as illustrated in Figure 1.6. The resolution of DPN is dependent on the humidity, roughness, writing rate and nature of the ink-substrate interaction. Under optimum conditions 14 nm resolution can be achieved[57]. DPN is compatible with a variety of molecular inks for instance small organic molecules (alkanethiols[56, 58, 59], alkoxysilanes[60], biotin[61], nitrilotriacetic acid (NTA)[62]), polymers[63, 64], biological molecules (DNA[65, 66], proteins[66-68], peptides[69]), colloids[70, 71] and sol-gels[72] have all been deposited on substrates ranging from metals to insulators. DPN has become one of the most used scanning probe lithographic (SPL) techniques[73]. Because of its capability to produce high registration and resolution patterns, and also its ability to integrate many different chemical functionalities onto a single surface without the risk of chemical cross-contamination, DPN has become an important tool for fabricating protein nanoarrays[74, 75]. In 2002 Lee et al reported the fabrication of arrays of Immunoglobulin G (IgG) with feature sizes of 350 – 100 nm, with negligible non-specific binding[67]. The researchers achieved this by first writing line or dot patterns of a carboxylic acid terminated alkylthiol onto a gold film using DPN. The surrounding areas were then filled in with an oligoethylene glycol (OEG) terminated thiol to

minimise non-specific adsorption. Immobilisation of the IgG and subsequent binding to anti-IgG were monitored using AFM. A massively parallel DPN device has been developed, in which 55,000 tips are able to write in parallel[76]. Each tip is separated by 90 and 20 µm in the x and y axes, respectively, and occupies a 1 cm^2 area. To ensure all the tips can write in unison, the tips must all be aligned. This is done not by the use of a complex feed-back system, but simply by the use of gravity to bring all the tips into contact with a sacrificial substrate prior to use. This approach increases the throughput of DPN to a point where as many as 450,000,000 sub-100 nm features have been patterned in less than 30 min[74]. This method has also been used to pattern biologically important molecules such as phospholipids with feature sizes ranging from ~100 nm to several microns by Lenhert et al[77]. The researchers wrote the letters "INT" in phospholipids 55,000 times over a 1 cm^2 area in 12 s on a glass substrate. The substrate was left in a water solution overnight and the fluorescence was still visible, demonstrating the stability of the resulting lipid membranes on the surface.

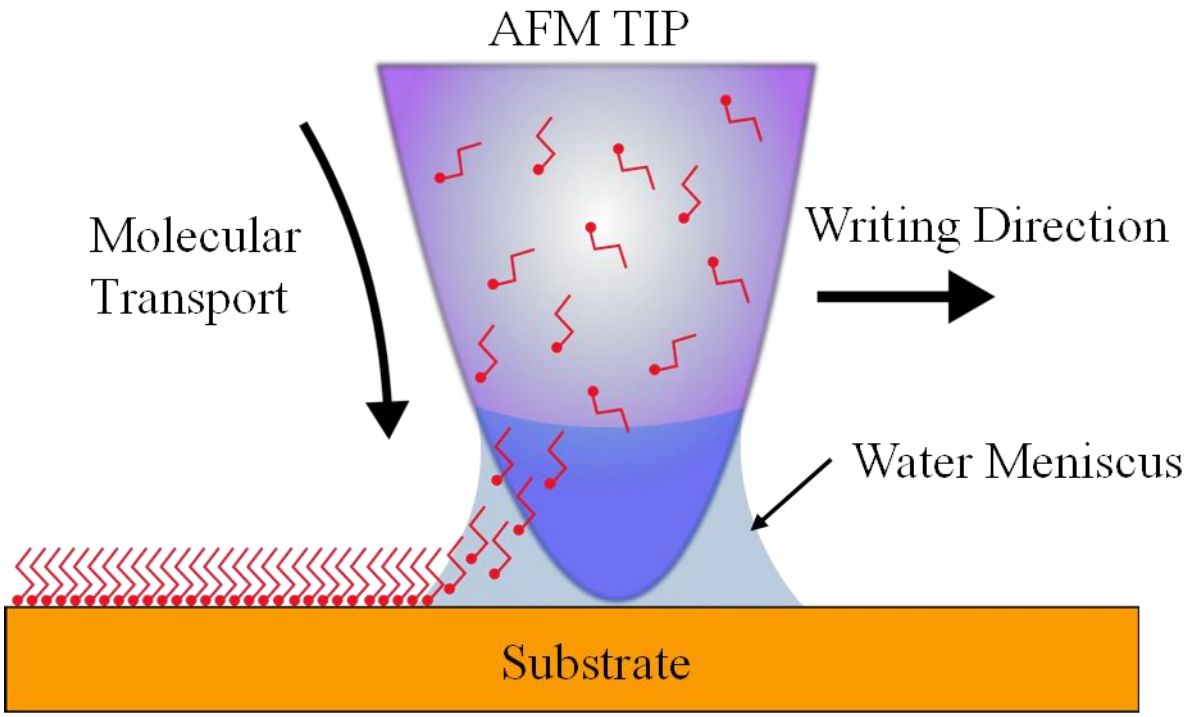

Figure 1.6: Schematic of DPN showing the transport of molecule to the substrate via the water meniscus.

1.5 Nanografting and Nanoshaving

Nanografting and nanoshaving share the same basic principle shown in Figure 1.7. An AFM tip is used to mechanically remove the absorbates from the substrate. Nanografting is done in

a solution of a contrasting adsorbate which fills the areas made by the tip. Nanoshaving simply removes the absorbate leaving the underlying substrate. These techniques have been applied to both gold-alkylthiol[78] and oxide-alkylsilane[79] systems to produce edge resolutions as good as to 2 nm.

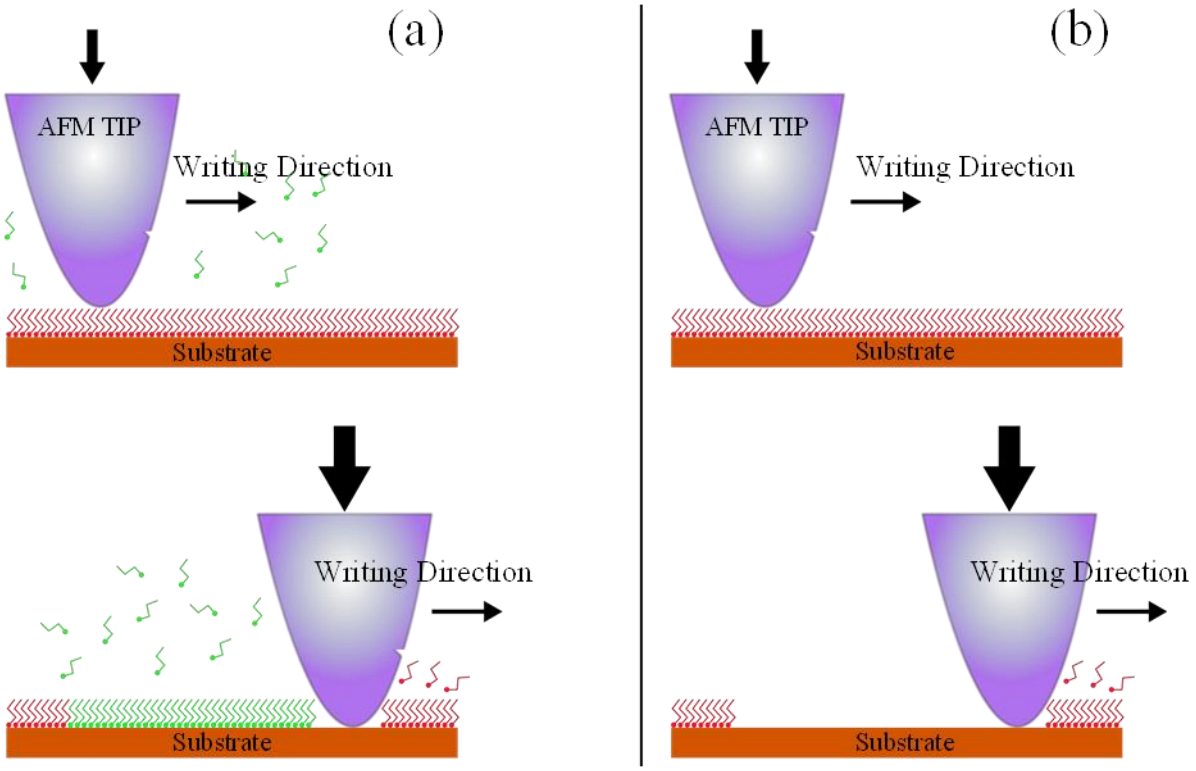

Figure 1.7: schematic of (a) the nanografting technique where the lithography takes place in the presence of a contrasting thiol. (b) the nanoshaving technique where the AFM tip removes the adsorbate to reveal the underlying substrate.

1.6 Local Oxidation

When an AFM probe is brought close to a surface a meniscus of water forms. Application of a potential difference between the tip and the surface can cause localised oxidation. The approach, known as local oxidation or as constructive nanolithography differs from the previously mentioned techniques (DPN and nanoshaving) since it allows for specific chemical reactions to take place at the surface of a pre-existing monolayer (Figure 1.8) [80].

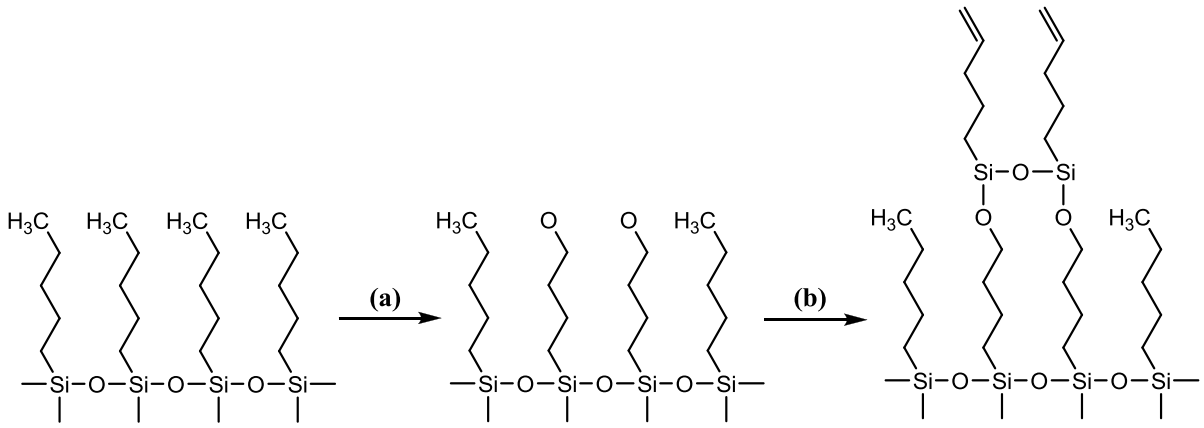

Figure 1.8: Schematic representation of local oxidation of an organic monolayer: (a) non-destructive patterning by an electrically biased AFM tip; (b) treatment with a vinyl terminated silane (NTS).

1.7 Microcontact Printing

Microcontact printing (μCP) uses an elastomeric stamp, typically PDMS, with surface relief structures to transfer an "inked" material onto a substrate. The general procedure is simple: a PDMS stamp is wetted with a solution of molecules that possess a specific affinity to the substrate, and the stamp is then held into contact with the surface of the substrate for a length of time, with the result that molecules then bind to the surface at the points of contact. μCP is one of the most useful techniques for producing patterns of functional organic molecules on surfaces over large areas[1, 81, 82]. μCP was first described by Whitesides' group in 1993. They used a PDMS stamp to pattern an alkanethiol onto a gold thin film, subsequent etching led to the formation of electrically conducting gold structures on the surface as small as 1 μm[83]. Since then μCP has been used to pattern a variety of materials including alkylsilanes[84, 85], phosphonic acid SAMs[86, 87], polymers[88-90], proteins[91-93], DNA[93, 94] and cells[93, 95]. Zschieschang et al have developed a process to fabricate organic thin-film transistors and organic complementary circuits using μCP, in which indirect-printing and direct-printing are combined in the same step[87]. A phosphonic acid SAM is patterned onto an aluminium thin film. The SAM is first employed as a resist to pattern the aluminium layer in a wet etching step, and secondly the SAM is retained on the underlying metal to act as a gate dielectric. The resolution of μCP is limited by the mechanical properties of the elastomeric stamp and the mechanism of transfer[96], a PDMS stamp provides sufficient mechanical strength for printing features as small as 500 nm[97]. However, a modification of the μCP process has led to the invention of edge-transfer lithography (ETL), which is able to pattern feature with sizes of

100 nm[98]. This is achieved by discontinuously dewetting the stamp, confining the ink to only the recessed areas of the stamp. When the stamp is put into contact with the substrate, the molecules are transferred from the edges of the relief structures.

1.8 Nanoimprint Lithography

Nanoimprint lithography (NIL)[39, 99] is a high throughput non-conventional lithographic technique that is capable of producing high resolution parallel patterns over large areas. The process involves using a hard mould to mechanically deform a polymer to produce a replica pattern. A main advantage of NIL is that it is a mechanical process, thus the minimum resolution is not limited by the diffraction of light. The two main types of NIL are thermal-NIL (T-NIL) and UV-NIL. T-NIL works by heating a polymer resist to above its T_g before applying pressure to the mould. The polymer resist is then cooled to below its T_g before the mould is removed. Whereas, UV-NIL works by using a liquid resist that is imprinted by a UV-transparent mould. A pulse of UV light is used to cure the liquid resist before the mould is removed. UV-NIL has advantages such as, absence of thermal expansion, low imprint pressure and low viscosity of the uncured resist. However, T-NIL is more commonly used for nano- and micro-patterning because it is more straightforward, it works with a broad range of polymers and the anti-stick layer, used for effective demoulding, is not degraded by heat as it is by UV-NIL[100]. Other variants of NIL, which offer an increased throughput, also exist, including step and stamp imprint lithography (SSIL)[101] and roll to roll nanoimprint lithography (R2RNIL)[102]. NIL has become an attractive and widely researched technology because of early demonstrations of very high resolution. In 1997 Chou's group reported a 10 nm hole array imprinted into PMMA[99]. The ultrahigh resolution in combination with the development of higher throughput technologies such as SFIL has made NIL appealing to the semi-conductor industry. In 2003 the International Technology Roadmap for Semiconductors (ITRS) announced the inclusion of NIL onto their roadmap as a candidate for the 32 nm node and beyond. However, NIL faces significant challenges in meeting the stringent requirements of the semi-conductor industry, in terms of defect control and throughput capability. Nevertheless, due to the simplicity of NIL, it has found applications in semiconductor fabrication[103], photonic crystals[104], MEMS[105], nanofluidic channels[106], biochip nanoarrays[107] and biodevices[108].

Thermal-NIL

In T-NIL a polymer is heated to above its T_g. At temperatures above a polymer's T_g, it will transform from a hard and brittle state into a molten or rubbery state. It is at this point that a rigid mould, typically formed from silicon, can be pressed into the polymer to mechanically deform it. The basic T-NIL process is illustrated in Figure 1.9. T-NIL is the earliest NIL technique and was developed by Chou's group who reported producing sub-25 nm features in PMMA in 1995[39]. Subsequently they fabricated patterns of holes as small as 6 nm[109]. Research into the mould filling[110] and the effect of polymer molecular weight on imprint defects[111] has helped to understand the imprinting process and further develop it. Advancements into new resists have led to a liquid thermal polymerisation resist, which can be imprinted at room temperature and low pressures. The resist consists of a mixture of methacrylate monomers and polymers as well as a radical initiator, which will cure into a solid polymer upon heating[112].

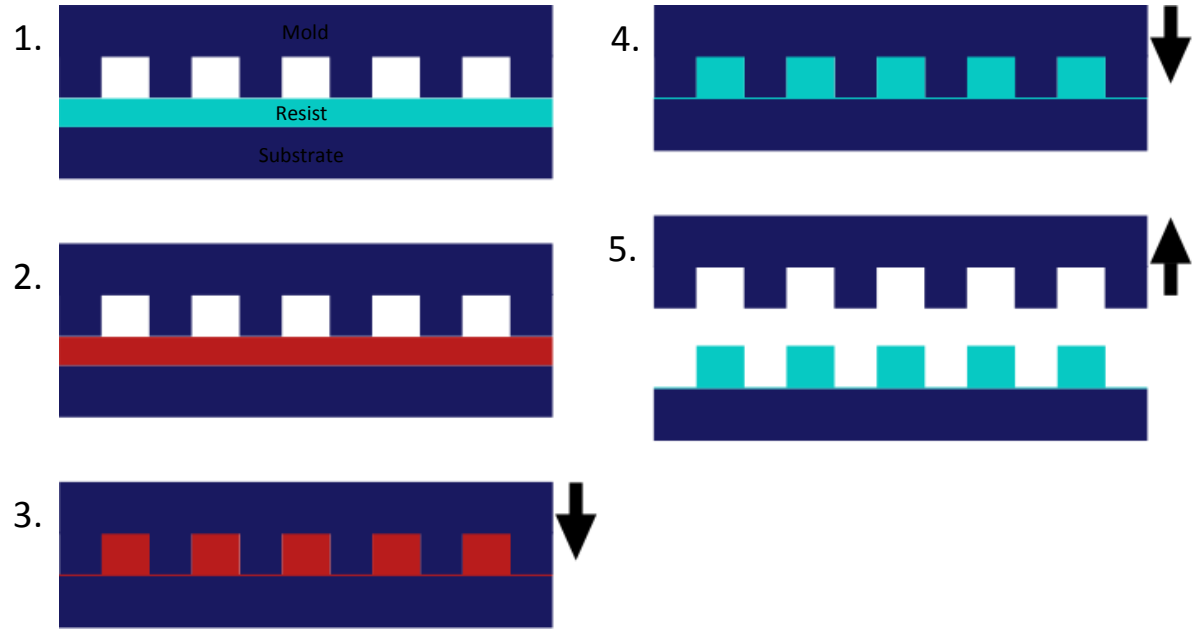

Figure 1.9: Schematic representation of the steps involved in T-NIL, 1. the mould is placed in contact with the resist layer, 2. the system is heated to temperatures above the T_g of the resist, 3. downward pressure is applied, displacing the liquid resist, which conforms to the shape of the mould, 4. the system is cooled to below the T_g of the resist, 5. the pressure is released and the mould is removed.

UV-NIL

UV-NIL is carried out at room temperature using a UV-transparent mould and a liquid resist precursor. When the mould is pressed into the resist precursor, the structural features of the mould displace the liquid, at which point a UV light floods the sample, curing the liquid precursor. This process is illustrated in Figure 1.10. In contrast to T-NIL, UV-NIL is carried out at low pressures and at room temperature. UV-NIL was first demonstrated by Haisma et al in 1996. They fabricated sub-100 nm features by imprinting a liquid acrylate monomer solution that was then polymerised by UV irradiation[113]. A variation of the standard UV-NIL process, SFIL, is tailored towards the high throughput production of low cost, high aspect ratio, high resolution patterns for the fabrication of semiconductor devices[114]. SFIL is based on a bilayer imprint scheme, which utilises an oxide-etch-resistant, photo-polymerisable monomer solution (an organosilicon derivative) to transfer a pattern into an underlying organic transfer layer[114, 115]. SFIL is considered to be the most suitable imprint technique for fulfilling the requirements of IC fabrication[116].

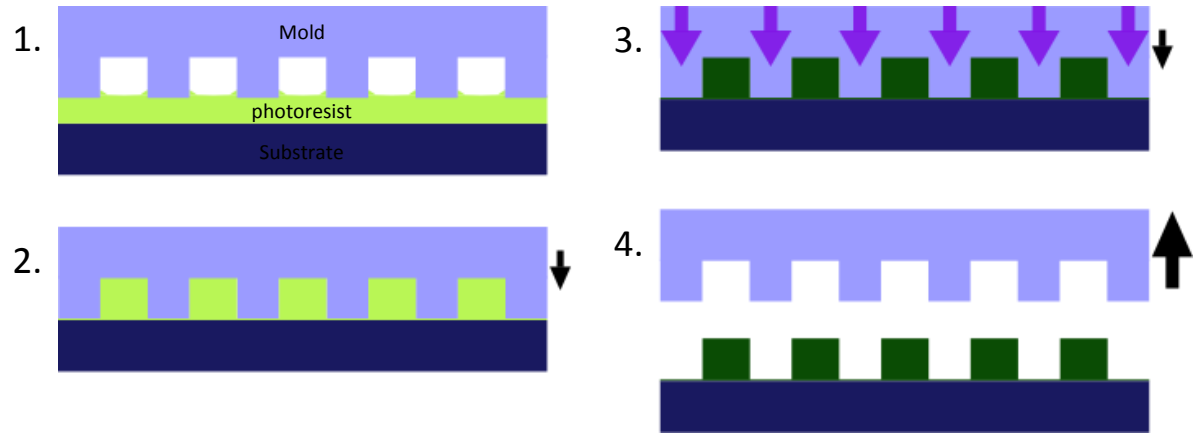

Figure 1.10: Schematic representation of the steps involved in UV-NIL, 1. the UV-transparent mould is placed in contact with the liquid photoresist layer, 2. a relatively small pressure load is applied, displacing the low viscosity photoresist, 3. the photoresist is cured by UV exposure through the mould, 4. the pressure is released and the mould is removed.

Reactive Ion Etching

After the polymer has been imprinted, it is sometimes necessary to remove the residual layer[99]. The residual layer is the remaining imprinted material in the trenches of the pattern, the thickness of which is determined by the original thickness of the polymer layer before

imprinting[117] and the imprint parameters, such as pressure, temperature and time. Most commonly a reactive ion etch (RIE) process is used to remove the unwanted material because, in contrast to wet etching, RIE is anisotropic[118]. Anisotropy is the property of being directionally dependant, as opposed to isotropy, which implies no directional dependants. With regards to etching, RIE is described as being anisotropic because the majority of the etching occurs in the vertical direction. In RIE electrodes create a strong electric field, which accelerates gas ions into the sample surface. The vertical bombardment by the ions leads to the anisotropic removal of material.

Mould Fabrication

The moulds used in NIL ultimately determine the resolution, therefore they are a critical part of the process. High resolution moulds are usually made by electron beam lithography and dry etching[119, 120]. The moulds are normally made in silicon, dielectric materials such as silicon dioxide or silicon nitride, metals such as Ni, or polymeric materials. NIL moulds must be hard and have high mechanical strength, to enable patterning of nanoscale features without the mould deforming or buckling during imprinting even at elevated temperatures. The fabrication of a silicon mould is straightforward. First a resist material is spin-coated onto the surface of the silicon, followed by lithography to define the mould pattern. Several lithographic techniques can be used including UV lithography for relatively large features, electron-beam lithography for very small features, interference lithography for large area periodic features, or NIL itself. A metal masking layer can then be deposited over the patterned resist, followed by a lift-off step which removes the resist and the metal on top, leaving a patterned mask layer behind. An RIE process is used to etch the unmasked silicon, producing the surface relief structures required for NIL.

1.9 Self Assembled Monolayers

SAMs are formed when surfactant molecules spontaneously adsorb onto a solid surface. The surfactant molecule consist of two end groups, typically connected by an alkylchain, one of which (the head) has a favourable and specific interaction with the substrate and the other (the tail) has a desired functionality (Figure 1.11). Selection of the tail group provides a simple means by which the surface properties can be controlled. The molecular self-assembly is governed by competing mechanisms, such as chemisorption, molecule-solvent interaction as well as molecular attraction and repulsion[121]. The two most widely studied SAM systems

are alkylthiolates on gold and alkylsilanes on oxide surface[122]. Research into alkylthiol SAMs and alkylsilane SAMs was pioneered by Allara and Nuzzo in 1983[123] and Sagiv in 1980[124] respectively. In both cases SAM formation is complex and involves many processes[122].

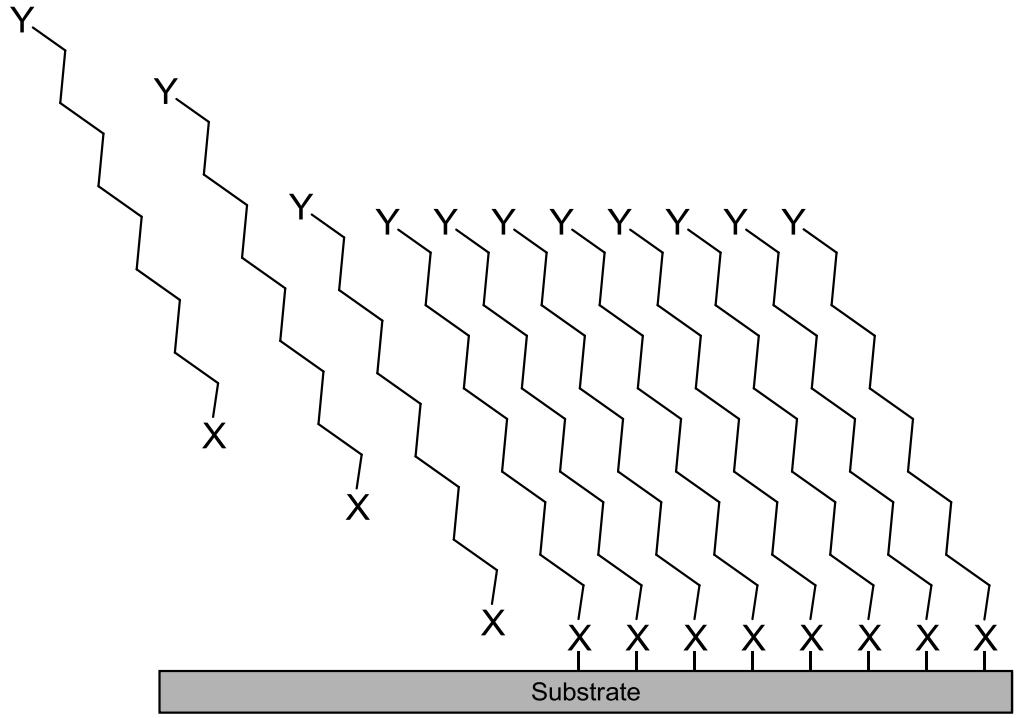

Figure 1.11: Schematic showing a simplified representation of a SAM, where X has a favourable and specific interaction with the substrate and Y has a desired functionality.

Au-Alkylthiolate SAMs

Thiols, RSH, or disulfides, RSSR, adsorb spontaneously on the surface of a gold substrate to yield the same alkylthiolate product[123, 125]. The general reaction scheme is shown below:

$Au + RSH \rightarrow AuSR + ½ H_2$

During polycrystalline Au film growth, the (111) termination is thermodynamically preferred. Delamarche et al found that for dodecanethiol ($C_{12}H_{25}SH$) adsorbed on a Au (111) surface, the molecule is canted 33° from the surface normal and is twisted about the chain by 55°. The conformation is an average as the results showed that there were several molecular conformations coexisting at room temperature, all of almost equal energies[121].

Monolayers of alkylthiolates on gold have been well studied. This is most likely due to the straightforward formation of high quality close packed monolayers and extensive range of monolayer functionalities available. The alkylthiolate SAMs are stable in air or in contact with water or ethanol, but they desorb at temperatures above 70 °C[126]. UV light can be used to photo-oxidise alkylthiolate monolayers in the presence of oxygen, to yield alkanesulfonates. The alkanesulfonates are only weakly bound to the gold substrate and can be removed or replaced with other alkylthiol molecules[127]. This property of the alkylthiolate SAMs makes them ideal for patterning, consequently increasing the possible applications

Oxide-Alkylsilane SAMs

Films may be formed on oxide surfaces by the adsorption of alkyl substituted silanes of the general formula, $RSiX_3$, where X = Cl, OMe or OEt and R is an alkyl chain, which may contain hetero atoms[128]. Alkylsilane SAMs are relatively stable. The stability is thought to be partly due to the cross polymerisation of molecular chains via the formation of Si-O-Si linkages[124, 129-131], although it has been shown that it is impossible for cross polymerisation to occur at full coverage of the substrate because the Si-O-Si cross links are too short to avoid major steric hindrances of the alkyl chains. It was concluded that in order to form dense monolayers of complete coverage, a means of preventing cross polymerisation was critical[132]. This suggested that for alkylsilane films, the formation and stability of the monolayer are due to a specific interaction between the head group and substrate and not the cross polymerisation. The chemical reaction involved in alkylsilane SAM formation is not a trivial one. The preparation of a good monolayer with uniform thickness depends on a variety of parameters, consequently reproducibility is an issue[133-135]. The presence of water is advantageous for monolayer formation, but only in trace amounts[131, 133]. The water acts as a catalyst by hydrolysing the Si-X bonds yielding an alkylsilanol, $RSi(OH)_3$, which is then able to condense with surface hydroxyl groups or other surface bound silanols releasing up to three molecules of water which will go onto react with other alkylsilanes[131, 136]. Because water is the catalyst and is not lost in the reaction, only a small amount is needed. It is important that the amount of water present is low otherwise silanols will start to form in solution and condense with other silanols. This can produce polymers which will eventually attach to the surface which can lead to an uneven surface and multilayers (Figure 1.12).

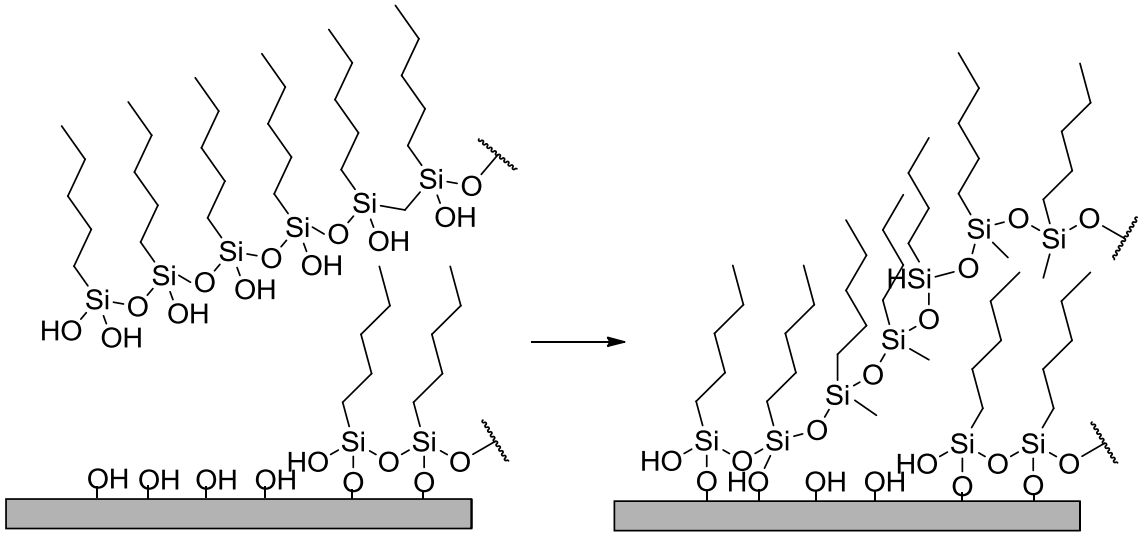

Figure 1.12: Example of how an alkylsilane polymer formed in solution can attach to the surface to form a multilayer.

1.10 Optical Microscopy

Optical microscopy is one of the most important scientific achievements in the history of mankind. Despite the incredible advancements in electron and scanning probe microscopy, the large majority of all microscopy investigations in the life sciences are still carried out using conventional lenses and white light. However, because of the diffraction limit, the ultimate resolution using a conventional optical microscope is approximately half the wavelength of the illuminating light. The diffraction limit was discovered in the 1873 by Ernst Abbe, and later refined by Lord Rayleigh in 1896. A consequence of diffraction is that features closer than ~200 nm cannot be resolved by lens-based light microscopy. However recent developments have begun to break through the diffraction barrier. In 2000, a theory that described a lens that produces perfect diffraction-free images was published by Pendry[137]. Such lenses were made from a slab of material possessing a negative refractive index in which the evanescent waves are enhanced rather than decaying across the slab. These lenses were dubbed "superlenses". The first example was made of a thin slab of Ag and was demonstrated to record features as small as 60 nm into a photoresist using a 365 nm light source[138]. Although these lenses amplify the evanescent waves and thus in principle enable their detection, the waves cannot be processed by conventional optics[139]. Another type of superlens, called a "hyperlens" relies on artificial anisotropic materials placed in multilayer stacks. The hyperlens is able to magnify the subwavelength features using cylindrical geometry, transforming the evanescent waves into propagating waves. The

propagating waves can then be processed by conventional optics[140]. Zhaowei Liu *et al* demonstrated a resolution of 130 nm using a 365 nm light source using a hyperlens consisting of a periodic stack of 35 nm Ag and Al_2O_3[141]. However, these superlenses must be illuminated with a specific laser source and would not function under a standard white-light source. Various other ways have now been found to achieve optical resolution far beyond the diffraction limit using white-light. One surprisingly simple way, is to use microspheres[142]. The microsphere nanoscope utilises small SiO_2 spheres to convert the evanescent waves into propagating waves. The spheres produce a virtual image of the subwavelength features that can be viewed in the far-field. Another more recent development has been to use a super-oscillatory lens (SOL). The SOL is a nanostructured mask, which on illumination with coherent light, creates a focus at a distance beyond the near-field that is able to resolve subwavelength features[143].

Fluorescent Microscopy

Fluorescent tagging or staining is widely used in the life sciences as a non-destructive way of analysing biological molecules. The vast majority of fluorescent microscopy is carried out by wide-field or confocal microscopy methods. The confocal microscope itself is an improvement on the conventional wide-field microscope. Confocal imaging is carried out using a small spot produced by a laser beam that is raster scanned across the sample to build up a 2D image. The spot is viewed with a spatially restricted optical system, so that only signals emanating from the spot are detected. Furthermore the signal intensity drops dramatically with distance from the focal plane. Thus, in contrast with wide-field microscopy, signals from above and below the focal plane, which would normally cause a background glow, are eliminated[144]. However, wide-field and confocal methods are diffraction limited and in many fields of biology, an improvement of resolution would be heavily beneficial. Currently it is possible to achieve far-field super resolution with a number of different techniques. One example is stimulated emission depletion microscopy (STED)[145], which uses two super imposed laser beams. The first, an excitation laser pulse, is immediately followed by a red shifted pulse called the STED beam. The STED beam is modified to have zero intensity at the focal centre, but strong intensity at its periphery creating a "doughnut" shape. The effect of superimposing the two beams is illustrated in Figure 1.13. Fluorophores that are initially excited by the first beam are then immediately transferred back to the ground state by stimulated emission brought on by the STED beam.

The fluorophores close enough to the focal centre where the STED beam has zero intensity are unaffected by the STED beam and thus yields a sub-diffraction scanning spot. Initial results produced a scanning spot with a diameter of 100 nm[146]. Advancement meant that the size of the PSF decreased down to 16 nm in diameter, this setup was used to resolve features 72 nm apart[147].

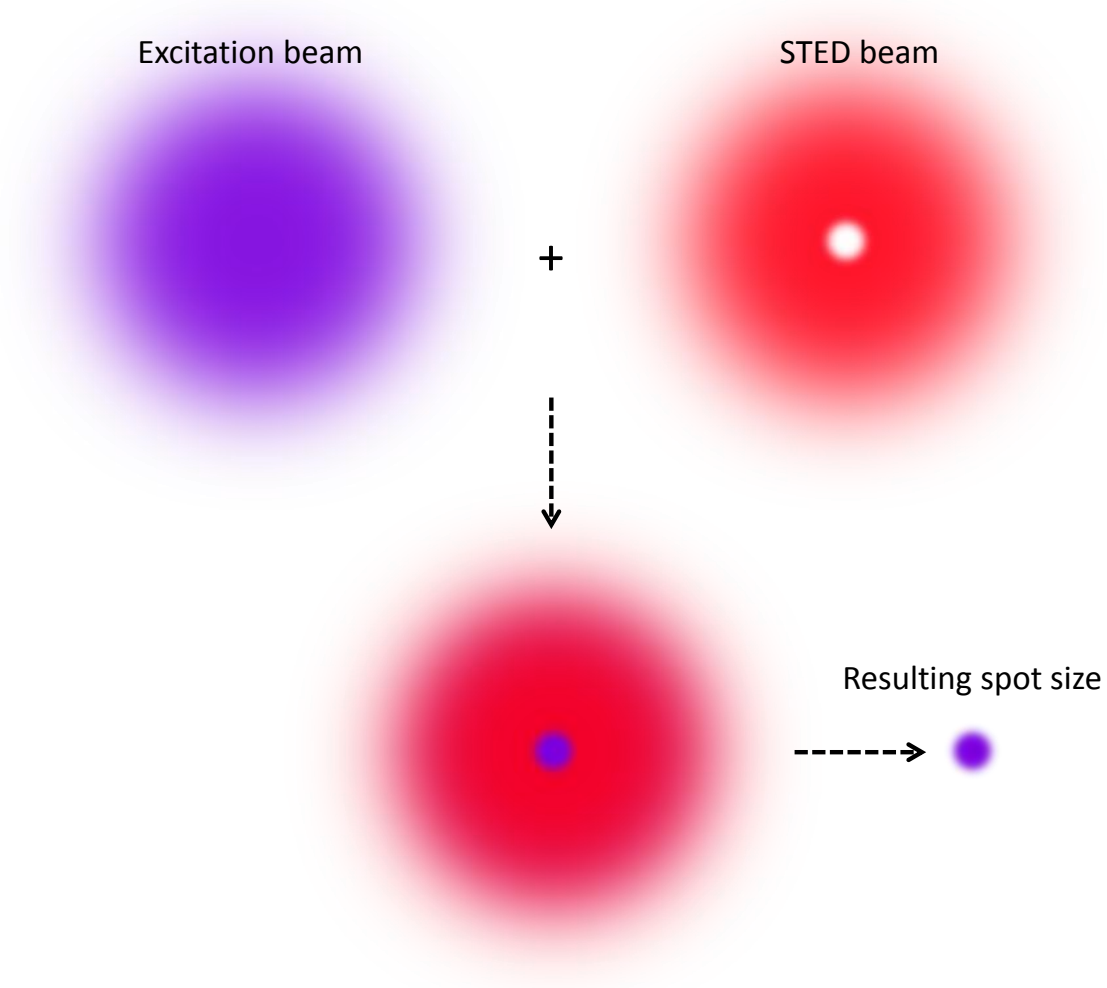

Figure 1.13: Schematic illustrating how the "doughnut shaped" STED beam when superimposed over the excitation beam, can dramatically reduce the effective size of the scanning laser spot.

Another method of achieving super resolution is stochastic optical reconstruction microscopy (STORM)[148] in which single molecules can be imaged. This can be achieved using photo-switchable fluorescent probes that can be switched between a fluorescent and a dark state. Emissions are detected from a sample area. Different molecules are turned on (made to fluoresce) at different times, so that at any one time it is probable that fluorescing probes will

be sufficiently far enough apart (> 200 nm) to resolve. Over time, an image can be built up that accurately depicts locations of the single fluorescent probes[149]. STORM can be achieved using a single fluorescent dye, but can be improved by using a paired dye that consists of a photo-switchable "reporter" fluorophore and an "activator" that facilitates photo-activation of the reporter. This method has been used to image mammalian cells with 20 to 30 nm resolution[150].

1.11 Scanning Electron Microscopy (SEM)

An electron microscope uses a beam of electrons to image a surface. In contrast to an optical microscope that uses a light beam, electrons have a much smaller wavelength than photons and consequently the electron microscope is less limited by diffraction. The SEM is a type of electron microscope that produces an image of a sample's topography by scanning a focused electron beam in a raster pattern. The most common mode of operation used is secondary electron imaging (SEI), where the beam of electrons interacts with the surface, emitting secondary electrons (SE) that can be detected. The energies of the SE that are detected are used to produce the image of the surface. Sample preparation can be an important part of SEM, because the sample needs to be electronically conductive. Therefore any non-conductive samples must first be coated in a thin layer of conducting material (usually Au). However, a variant technique exists called environmental SEM (ESEM), which permits deviations of the specimen chamber environment. Consequently, samples that are wet and or insulating may be analysed *in vivo* without preparation[151]. It is able to do this through two main alterations of the conventional SEM. Firstly, the column beam is separated from the specimen chamber by multiple pressure limiting apertures as opposed to just one. This allows the column to remain under a high vacuum while the chamber pressure can be as high as 50 torr[152]. Secondly, ESEM uses a detector that can operate within a non-vacuum environment. A positive potential is applied to the detector, thus the SE are accelerated towards it, and any collisions with gas molecules result in ionisation. This yields additional electrons, amplifying the SE signal, and positive ions. When scanning an insulating sample, surface charging is supressed by the build-up of positive ions on the surface.

1.12 Scanning Probe Microscopy

In a scanning probe microscope (SPM) a sharp tip is scanned across a surface in a raster pattern. Data recoded by the tip's interaction with the surface can be transformed into an

image. The field of scanning probe microscopy was born with the invention of the scanning tunnelling microscope (STM) in 1981 by Binnig and Rohrer[153] (who in 1986 received the Nobel Prize in Physics for their efforts). The STM measures the current that results from electron tunnelling between an atomically sharp tip and a conductive surface at small separations under the influence of a potential difference. The tunnel current depends exponentially on the tip-surface separation. As the tip is scanned across a surface, the changes in height cause a change in current which can be measured and mapped to yield an image[154]. It was realised early on that mechanical forces acted at the tip-sample contact and these could be measured. This led to the development of the atomic force microscope (AFM) in 1985 by the same team at IBM[155]. Around about the same time it was also demonstrated that the near-field associated with a sub-wavelength aperture could be used as a kind of proximal optical probe, by taking advantage of similar scanning systems to those used in the STM. This type of SPM is called a SNOM, also known as a near-field scanning optical microscope (NSOM)[156, 157]. In all cases the performance of the microscope is heavily dependent on the sharpness and quality of the probe as well as the piezoelectric scanner, which enables precision movements of the probe.

Atomic Force Microscopy

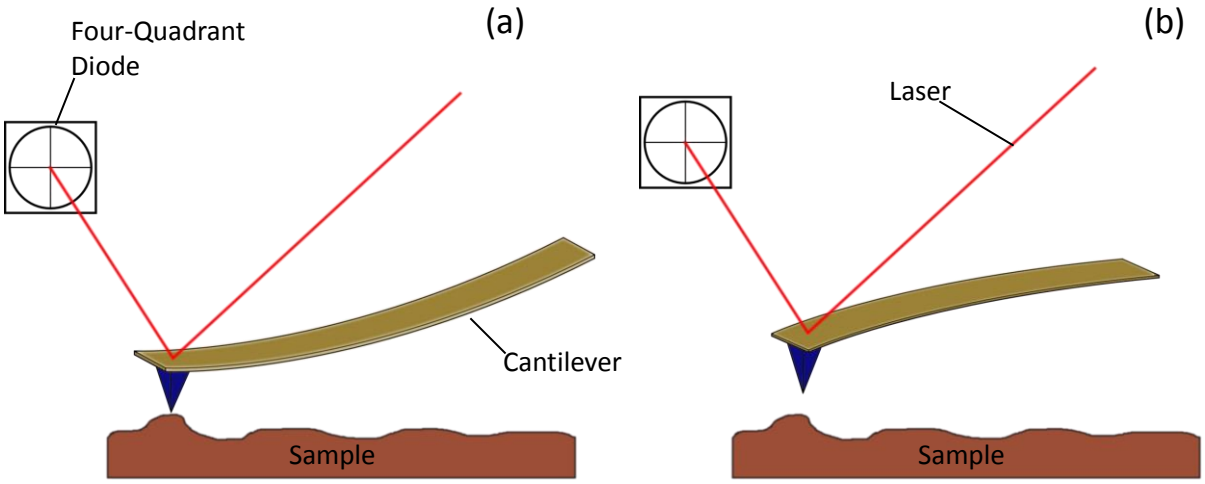

Figure 1.14: Schematic showing the principles of an AFM in (a) contact mode (b) non-contact mode. As the tip is scanned across the sample (or vice versa) the cantilever bends relative to the surface topography. The movement is recorded by the deflection of a laser beam.

An AFM consists of a sharp tip that is attached to a cantilever, which is scanned across a surface. The basic principles are illustrated in Figure 1.14. In its most common realisation, a laser beam is deflected off the back of the cantilever onto a photodiode. The cantilever can be treated as a Hookean spring, for which F = -kx, where F is the force, k is the spring constant and x is the deflection. Any movement in the cantilever alters the angle of deflection and is recorded by the photodiode. The cantilever effective height is controlled by a piezoelectric crystal that can either move the cantilever or the sample up and down. In constant height mode the cantilever height remains fixed and variations in the deflection are measured. In constant force mode the cantilever height is adjusted to maintain a constant, pre-set cantilever deflection. Constant force mode is certainly the more widely used of the two and provides the most accurate data on sample topography[158].

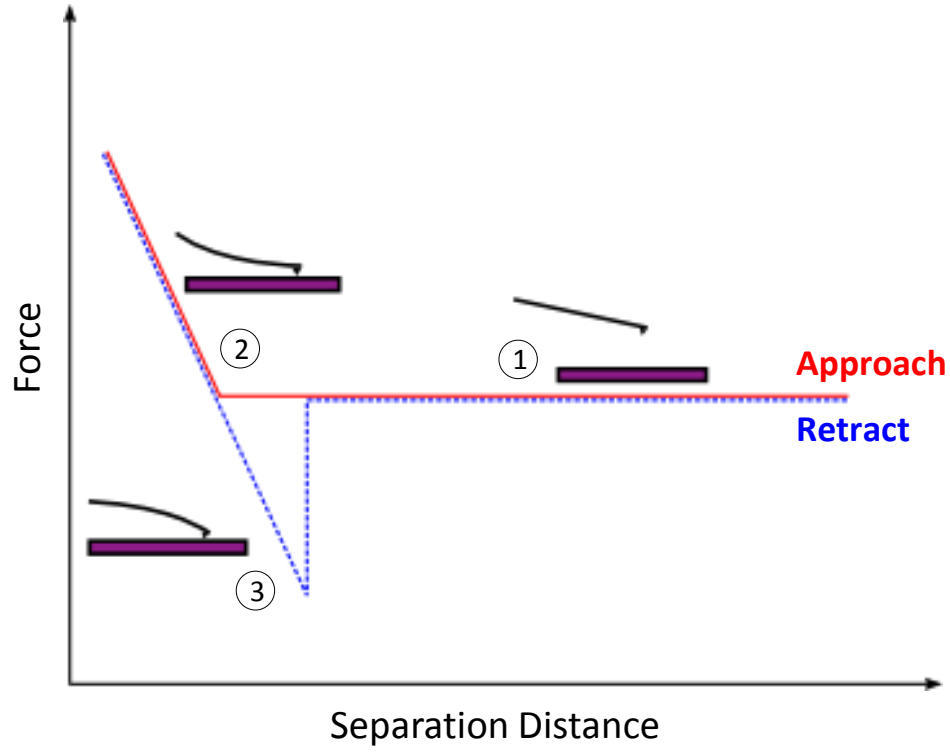

Figure 1.15: Force-distance curve illustrating the interaction of the probe with the sample surface.

An AFM can operate in one of two modes, which exploit either the short-range repulsive interaction (contact and tapping) or the long-range attractive interaction (non-contact). Figure 1.15 shows an illustration of the interaction of the AFM tip with the sample surface. (1) At large tip-sample separations, there is no detectable interaction force. (2) At some point close to the sample, the tip "snaps" into contact, as the tip is moved closer a repulsive force is

measured due to the quantum mechanical repulsion between the interpenetrating electron clouds of the tip and sample. (3) On retracting the tip, the attractive forces are measured until at some point the forces exerted by the bending of the cantilever overcome those of attraction and the tip breaks away from the sample.

Modes of Operation

In contact (repulsive) mode (Figure 1.14 (a)) the tip is positioned in physical contact with the sample before being scanned across it. The relatively low spring constant of the cantilever (typically in the region of 0.06 - 0.35 Nm^{-1}) allows for it to bend in the vertical plane in response to surface height changes. Generally the feed-back electronics are set to a constant force, in which the deflected laser is kept in the horizontal plane of the detection sensor by the piezoelectric crystal. The voltage applied to the crystal is translated into a two-dimensional image of surface topography.

In tapping mode the tip and the cantilever are oscillated near or at the resonant frequency of the cantilever, such that the tip is only intermittently in contact with the surface[159]. Because the tip is only in contact with the surface for a short period of time the lateral forces applied to the surface are minimal, making it a more suitable imagine techniques for samples containing biological specimens or polymers.

In non-contact (ac imaging) mode the tip is positioned within the attractive regime of the force curve ((3) in Figure 1.15) relative to the sample and is oscillated at a high frequency, close to the resonant frequency of the cantilever. This allows for the tip to interact with the surface without being in contact with it. The technique is more challenging than the other modes mentioned (contact and tapping) but is sometimes required when imaging particularly delicate specimens that would be otherwise be destroyed through contact with the tip[158]. In addition non-contact mode is the only AFM mode that can image a specimen with true atomic resolution[160].

Friction Force Microscopy

In contact mode, a variety of types of images may be acquired besides the topographical data that yield the physical contours of the sample. In a friction force microscope (FFM) or lateral force microscope (LFM), the deflection of the laser beam is detected in the horizontal plane of the photodiode[158]. Frictional interaction between the tip and the surface cause torsional

bending in the cantilever which is detected by the sensor as movements of the laser beam right or left of the centre. The twisting of the cantilever is negligible when scanned parallel to the axis of the cantilever but is maximised when sample is scanned perpendicular to the axis. Thus, accurate lateral force measurements are constrained to the perpendicular scan direction[161]. The intensity of the lateral force applied to the tip depends on the strength of the interactions between the tip and the surface. Hence the degree of horizontal movement of the deflected laser beam provides a measure of the frictional interactions of the sample with the tip. However when imaging non-planar surfaces topography-induced lateral forces are superimposed onto the true lateral force signal[162]. This can be rectified, however, by subtracting the scans in the forward and backward directions from each other, which removes the topographic component to a large extent. This also has the effect of enhancing the contrast by a factor of two[162]. FFM has been used to study SAMs containing regions terminated with carboxylic acid groups and regions terminated with methyl groups on length scales of only a few microns[163]. The acid functionalised regions yielded much greater contrast compared to the methyl functionalised regions, reflecting the much higher surface free-energy.

Scanning Near-Field Optical Microscopy

In fields such as biological science and materials science, optical microscopy is widely used for viewing and studying samples under high magnification given there non-invasiveness, ease of use and low cost. However the maximum spatial resolution that can be attained by conventional optical microscopy is limited to approximately half the wavelength of the light being used. Subsequently the theoretical resolution is limited to 200 nm, which is restrictive for many applications. In the early 20th century, Synge published a series of papers suggesting that near-field exposure could provide a solution to the diffraction limit[164, 165]. The idea was to pass high intensity light through a small, sub-wavelength sized hole in an opaque screen. The screen would be positioned in close proximity to the sample surface so the emerging light could be used to image the sample before it had time to diffract out. Getting the screen in close enough proximity with the samples surface was a major challenge in Synge's idea. Dust particles and surface defects would create relatively large separations between the aperture and the sample, resulting in diffraction of the passing light. It was not until the mid-1980's that sub-diffraction limited optical measurements were first reported[157, 166]. The work led to the development of the modern day SNOM. Instead of using a

macroscopic screen with a small hole, the SNOM employed an opaque tip with a sub-wavelength aperture at its apex. Using a probe allows the aperture to be positioned close to the surface without being affected by dust particles or surface defects. The probe is generally made from a glass or silica fibre and is coated in an opaque metal such as Al. The end is etched using HF, or heated and pulled, to form a sharp tip. In the shear-force feedback system, the probe is fixed to one leg of a small tuning fork. As the probe interacts with the surface the oscillations of the tuning fork is damped. This effect is detected and the height of the probe adjusted by the piezoelectric scanner[24]. Alternatively, a probe similar to the type used in the AFM is employed, but with a hollow tip that has an aperture at its apex, is used. In this case, light is focused onto the back of the probe. The probe is then brought into close proximity with the surface as it is in an AFM, and a beam of light is reflected off of the back of the cantilever onto a detector. Feedback from the detector is used to maintain the probe at a constant distance close to the surface. The applications of SNOM include single molecule studies, thin film analysis and probing biological samples[167]. However, SNOM has largely struggled to realise its potential as a nanoscale characterisation tool, possibly because it is perceived as a difficult technique[24].

1.13 Chemically Patterned Surfaces and their Applications

Chemically patterned surfaces play a unique role in analytical chemistry. Molecular films can be used to tailor interfacial properties such as adhesion, lubrication, wettability and biocompatibility. They can serve as supports to immobilise biological and chemical reagents to create functional patterns for fundamental studies and selective chemical sensing.

A multitude of lithographic techniques can be used to pattern a molecular film, creating chemical patterns of terminal functional groups such as amines and carboxylic acids. These reactive groups can be used to covalently attach other chemicals with a desired function or property. A common approach is to use molecular films of (3-aminopropyl)triethoxysilane (APTES) formed on glass or silicon substrate. The formation of the APTES film is not straightforward; the thickness, morphology and structure of the resulting film can be heavily affected by the deposition method, solvent, presence of water and curing method[131, 168]. The terminal amine group allows for a wide range of chemical reagents to be covalently bonded to the surface. The incorporation of a photocleavable protecting group onto APTES molecules allows for the fabrication of chemical patterns by photolithographic methods.

The very high binding affinity that exists between biotin and avidin is one of the most exploited in bioconjugation chemistry. Functionalisation of an APTES film with biotin is not complex, however does require a coupling agent such as N,N'-dicyclohexylcarbodiimide, or an activating agent such as N-hydroxysuccinimide to enhance the reactivity of the biotin's carboxylic acid towards the terminal amine of the APTS film. The biotin molecules attached to the surface can then be used to specifically immobilise avidin or streptavidin proteins on the surface. The ability to bind proteins with high affinity and excellent selectivity for specific targets is important for applications such as nanoscale biosensors[6].

1.14 Outline of this Thesis

This thesis focuses on the fabrication of chemically patterned surfaces using both photolithographic methods and NIL for the patterning of biological molecules. The different lithographic techniques are used to pattern biocompatible molecules on both the micron and nano-scale, but with an emphasis to fabricate nanostructures over a macroscopic area.

Chapter 2 reports the process and analysis steps involved in the fabrication and characterization of patterned surfaces including interference lithography, SNP and NIL. It focuses on the synthesis of an aminosilane with an o-nitrobenzyl photo-cleavable protecting group, the formation and derivatisation of SAMs including grafting of a polymer brush, and the surface analysis techniques used such as contact angle, AFM, XPS and confocal microscopy.

Chapter 3 demonstrates the integration of top-down and bottom-up nanofabrication techniques by the photolithographic patterning of a photo-sensitive monolayer and subsequent growth of a non-fouling polymer brush from the exposed areas. Interference lithography was used to fabricate periodic nanostructures over macroscopic areas and SNP was used to fabricate arbitrary nanostructures over a microscopic area.

Chapter 4 investigates the combination of NIL and molecular self-assembly for fabricating nanostructured arrays of proteins on a chemically patterned surface over a macroscopic area and with high control over the spatial organization of the proteins on the surface.

Chapter 5 reports a novel approach to a reusable biodevice. NIL is used to pattern TiO_2 metal using a methacrylate precursor resist. The pattern structures of TiO_2 act as switchable

platforms for protein adsorption and degradation, allowing for a protein array to be reused many times.

Chapter 6 summarises the results of all the work described in this thesis, and suggestions for future work are made.

Chapter Two

2 Experimental

2.1 Materials

Synthesis

{N-[2-(2-Nitrophenyl)propan-1-oxycarbonyl]-3-aminopropyl}-triethoxysilane

Paraformaldehyde (>95%), 2-ethylnitrobenzene (purum >98% GC), hydrochloric acid (puris plus p.a. >30%), benzyltrimethyl ammonium hydroxide (triton B) (40 wt. % in methanol), 3-(triethoxysilyl)propyl isocyanate (95%), triethylamine (>99%), potassium dihydrogen phosphate (A.C.S 99+%) were supplied by Sigma-Aldrich and used as received. Magnesium sulfate $MgSO_4$ (dried), Dichloromethane (HPLC grade), petroleum ether (40-60), ethyl acetate (HPLC grade), diethyl ether (anhydrous grade) were supplied by Fisher Scientific and used as received.

Self Assembled Monolayer Formation

(3-Aminopropyl)triethoxysilane (APTES) (99%), ammonium hydroxide solution (A.C.S. 28-30% NH_3 basis) were supplied by Sigma-Aldrich and used as received. 2-[Methoxy(polyethyleneoxy)propyl]-trichlorosilane (PEG-silane) was supplied by Fluorochem and used as received. Sulfuric acid (1.83 S.G. 95+%), hydrogen peroxide solution (100 volumes 30+%), ethyl alcohol absolute (99.8+%) were supplied by Fisher Scientific and used as received. Silicon wafers (reclaimed, p-type, <100>) were supplied by Compart Technology. Cover slips (22 mm x 64 mm No. 1.5) were supplied by Menzel-Gläser. Electron microscope grids (1000 - 2000 Mesh Cu) used for micropatterning were obtained from Agar Scientific.

Surface Derivatisations

Bromoisobutyryl bromide (BIBB) (98%), Biotin (≥99%), N-(3-Dimethylaminopropyl)-N-ethylcarbodiimide hydrochloride (EDC) (purum ≥98%), Triethylamine (TEA) (>99%), adipoylchlorid (98%) were supplied by Sigma-Aldrich and used as received apart from triethylamine which was distilled over calcium hydride (93%, Fisher Scientific) and stored over molecular sieves (4Å, Sigma-Aldrich). Dichloromethane was supplied by the Grubbs dry solvent system.

Surface Initiated Atom Transfer Radical Polymerisation (SI-ATRP)

Poly(ethylene glycol) methyl ether methacrylate (OEGMA) (M_n 475), 2,2'-bipyridyl (puriss. P.a., >99%), copper(I) bromide (99.999%), copper(II) bromide (99%) were purchased from Sigma-Aldrich. methanol (HPLC grade), aluminium oxide (basic) were purchased from Fisher scientific.

Protein Immobilisation

Streptavidin-Cy3, -Cy5, -FITC, IgG-FITC and phosphate buffered saline (PBS) were purchased from Sigma-Aldrich. PBS came in tablet form, 1 tablet was dissolved in 200 mL de-ionised water and stored for no longer than 1 month. Wheat germ agglutinin-fluorescein was purchased from Vector Labs, USA.

Nanoimprint Lithography

PMMA resists were purchased from Micro Resist Technology, Germany and used as received. NIL moulds were purchased from NTT Advanced Technology Corporation, Japan. Moulds were cleaned in piranha solution and coated in an anti-adhesive film before use.

2.2 Synthesis

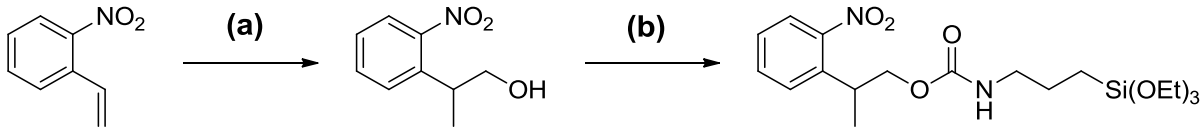

1 **2** **3**

Reagents and conditions: (a) paraformaldehyde, benzyltrimethylammonium hydroxide (Triton B), MeOH, 80 °C, 20 h, 36%; (b) 3-isocyanatopropyltriethoxysilane, Et3N (9% mol equiv), DCM, 60 °C, 24 h, 72%.

2-(2-Nitrophenyl)propan-1-ol, 2

This was first synthesized according to previously reported procedures[169, 170]. To a 40% benzyltrimethylammonium hydroxide (Triton B) solution in MeOH (27.7 mL of solution, 61 mmol) was added 2-ethylnitrobenzene **1** (8.1 mL, 60.0 mmol) followed by paraformaldehyde (1830 mg, 61 mmol). The mixture was refluxed at 80 °C for 20 h, evaporated under reduced pressure to a small volume, and adjusted to pH 7 with 1 M aq HCl (~40 mL). The mixture

was extracted thrice with EtOAc (60 mL each), and the organic layers were combined, dried with $MgSO_4$, and evaporated under reduced pressure to give a dark brown oil. This was purified by flash column chromatography (hexanes/EtOAc, 4:1 2:1) to yield the desired product as a deep orange oil (3912 mg, 21.6 mmol, 36%); *Rf* 0.1 (hexanes/EtOAc, 4:1); δH (400 MHz, $CDCl_3$) 1.34 (3H, d, *J* 7, C***H***$_3$CH), 1.70 (1H, s(br), O*H*), 3.52 (1H, m, CH_3C***H***), 3.81 (2H, m, CHC***H***$_2$O), 7.39 (1H, dd, *J* 8 and 8, 5-Ph), 7.50 (1H, d, *J* 8, 3-Ph), 7.59 (1H, dd, *J* 8 and 8, 4-Ph), 7.76 (1H, d, *J* 8, 6-Ph).

{*N*-[2-(2-Nitrophenyl)propan-1-oxycarbonyl]-3-aminopropyl}-triethoxysilane, 3

This was first synthesized according to previously reported procedures[170]. 2-(2-Nitrophenyl)propan-1-ol **2** (3518 mg, 19.42 mmol) was dissolved in DCM (18 mL), 3-isocyanatopropyltriethoxysilane (5.5 mL, 22.2 mmol) was added, followed by triethylamine (250 μL, 1.8 mmol), and the mixture refluxed at 60 °C for 24 h. Et_2O (25 mL) was added, and the mixture extracted with 0.1 M potassium phosphate buffer pH 7 (50 mL thrice). The organic layer was dried with $MgSO_4$ and evaporated under reduced pressure, and the residual yellow oil was purified by flash column chromatography (hexanes/EtOAc, 3:1 2:1) to yield the desired product as a yellow oil (6020 mg, 14.05 mmol, 72%); *Rf* 0.50 (hexanes/EtOAc, 1:1); δH (400 MHz, $CDCl_3$) 0.59 (2H, t, *J* 8, C***H***$_2$Si), 1.21 (9H, t, *J* 7, OCH_2C***H***$_3$), 1.34 (3H, d, *J* 7, C***H***$_3$CH), 1.58 (2H, tt, *J* 7 and 8, CH_2C***H***$_2CH_2$), 3.12 (2H, td, *J* 7 and 6, NHC***H***$_2$), 3.70 (1H, m, CH_3C***H***), 3.81 (6H, q, *J* 7, SiOC***H***$_2$), 4.10 (1H, m, CHC***H***$_2$O), 4.23 (1H, m, CHC***H***$_2$O), 4.85 (1H, s(br), CON***H***CH_2), 7.36 (1H, dd, *J* 8 and 8, 5-Ph), 7.47 (1H, d, *J* 8, 3-Ph), 7.56 (1H, dd, *J* 8 and 8, 4-Ph), 7.73 (1H, d, *J* 8, 6-Ph).

2.3 Cleaning Glassware and Substrates

All glassware used in the formation of SAMs was first cleaned by submersion in piranha solution, a mixture of 30% hydrogen peroxide and 95% concentrated sulphuric acid in the ratio 3:7 for at least 40 min. (***Caution:*** *piranha solution is an extremely strong oxidising agent which has been known to detonate spontaneously upon contact with organic material*). The glassware was rinsed thoroughly with de-ionised water (Elgar nanopure, 18.2 MΩ) for a minimum of 6 times and then sonicated for 10 min before placing in the oven (approx. 80 °C) and left over night to dry.

Extra attention was made for the substrates (glass slides/silicon wafers). Before submersion in piranha solution the substrates were first cut to size using a diamond tipped scribe and then sonicated in toluene, acetone and de-ionised water for 15 min respectively. After treatment with piranha the substrates were rinsed with de-ionised water and then submerged in the RCA (Radio Cooperative America) 1 clean. A 1:1:5 mixture of 30% hydrogen peroxide, ammonium hydroxide (28-30% NH_3 basis) and de-ionised water at 80 °C. The substrates are then rinsed thoroughly again before placing in the oven to dry.

2.4 Preparation of Self Assembled Monolayers

NPPOC-siloxane SAM formation

To reduce any chances for the silanes to polymerise in solution and subsequently form an uneven multilayer the preparations were carried out in moisture controlled conditions. All glassware and substrates were dried in the oven over night before use. The substrate (glass slide/silicon wafer) was placed in a Schlenk tube fitted with a suba seal. The tube was vacuum purge cycled with nitrogen three times. Dry toluene was degassed with nitrogen for approximately 20 min. The substrates were then immersed in a 1 mM solution of NPPOC-siloxane in toluene. The Schlenk tubes were wrapped in foil to illuminate light exposure and left for 48 h. The substrates were then rinsed with ethanol, sonicated in toluene for 10 min and rinsed again with ethanol. Substrates were then dried under a stream of nitrogen and then placed in a vacuum oven for 1 h at 120 °C.

3-(Aminopropyl)triethoxysilane (APTES)

Substrates were placed in vials and immersed in a 1% solution of APTES in ethanol and left for 30 min. The substrates were then rinsed and sonicated in ethanol, dried under a stream of nitrogen and then placed in a vacuum oven for 1 h at 120 °C.

2-[Methoxy(polyethyleneoxy)propyl]-trichlorosilane (PEG-silane)

Substrates were placed in Schlenk tubes and fitted with suba seals. . The tubes were vacuum purge cycled with nitrogen three times. Dry toluene was degassed with nitrogen for approximately 20 min. The toluene was then added to the tubes making sure to completely cover the substrates. A volume of PEG-silane was added to make a 1 mM solution. The reaction was left for 2 h under nitrogen. The substrates were then rinsed with ethanol,

sonicated in toluene for 10 min and rinsed again with ethanol. Substrates were then dried under a stream of nitrogen and then placed in a vacuum oven for 1 h at 120 °C.

Octadecylphosphonic acid (ODPA)

Clean glass slides were submitted to evaporation of approximately 15 nm titanium. The titanium coated substrates were then immersed in a 10 mM solution of ODPA in toluene for 12 h. The substrates were sonicated in toluene and rinsed with ethanol, before being dried under a stream of nitrogen.

2.5 Surface Derivatisations

Bromoisobutyryl bromide (BIBB)

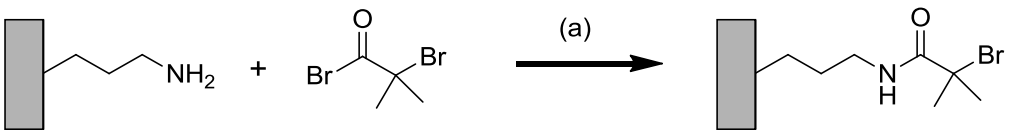

Reagents and conditions: (a) Triethylamine, dichloromethane, RT, 30 min.

The attachment of the ATRP initiator, BIBB, to the amine functionalised surface was carried out under dry conditions in a nitrogen atmosphere. Samples were immersed into a solution of BIBB (162 mM) and TEA (181 mM) in DCM and left to react for 30 min. The samples were then rinsed with DCM and ethanol and then sonicated in DCM. Then dried under a stream of nitrogen.

Adipoyl Chloride

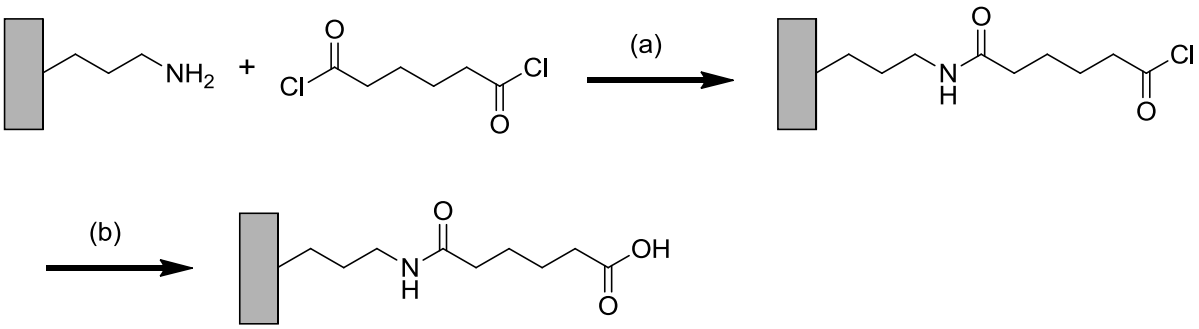

Reagents and conditions: (a) Triethylamine, dichloromethane, RT, 1 h; (b) water, RT, 10 min.

Derivatisation of surface amine groups with adipoyl chloride was carried out initially under dry conditions. Samples were immersed into a solution of adipoyl chloride (100 mM) and TEA (150 mM) in DCM and left to react for 1 h. The samples were then incubated in DI water for 10 min to convert the terminal acid chloride into a carboxylic acid group.

Biotin

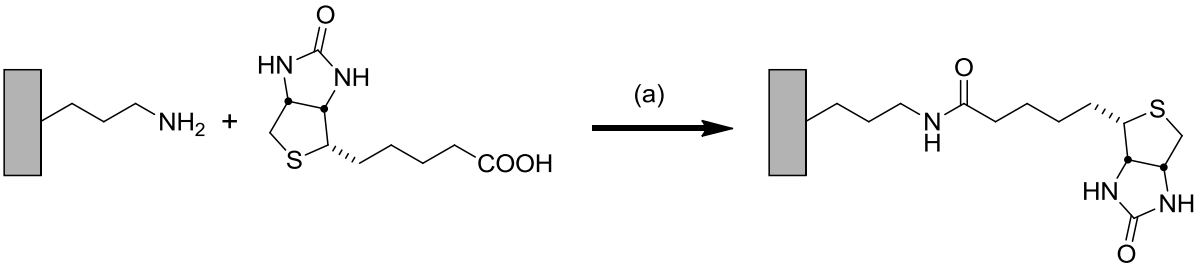

Reagents and conditions: (a) 1-Ethyl-3-(3-dimethylaminopropyl)carbodiimide, water, RT, 2 h.

Attachment of biotin to the amine functionalised surface was performed in the presents of the peptide coupling agent, 1-Ethyl-3-(3-dimethylaminopropyl)carbodiimide (EDC). Because the carboxylic acid of biotin is not electrophilic enough to react with an amine to form an amide, EDC first reacts with the carboxylic acid forming an amine reactive O-acylisourea intermediate. Samples were immersed in a solution of biotin (1mM) and EDC (I mM) in de-ionised water for 2 h. Samples were then rinsed thoroughly in de-ionised water and ethanol and then dried under a stream of nitrogen.

2.6 Surface Initiated Atom Transfer Radical Polymerisation (SI-ATRP)

ATRP uses a Cu(I) complex as the active catalyst in the formation and trapping of the alkyl radical as shown in Figure 2.1, thus all reaction solvents were thoroughly degassed with nitrogen before and after addition of the Cu(I) catalyst. This is necessary in order to avoid the Cu(I) oxidising to the inactive form, Cu(II). However a small amount of Cu(II) is added, which helps control the polymerisation[171, 172]. Cu(II) is added in place of a sacrificial initiator, which causes polymerisation in solution[173].

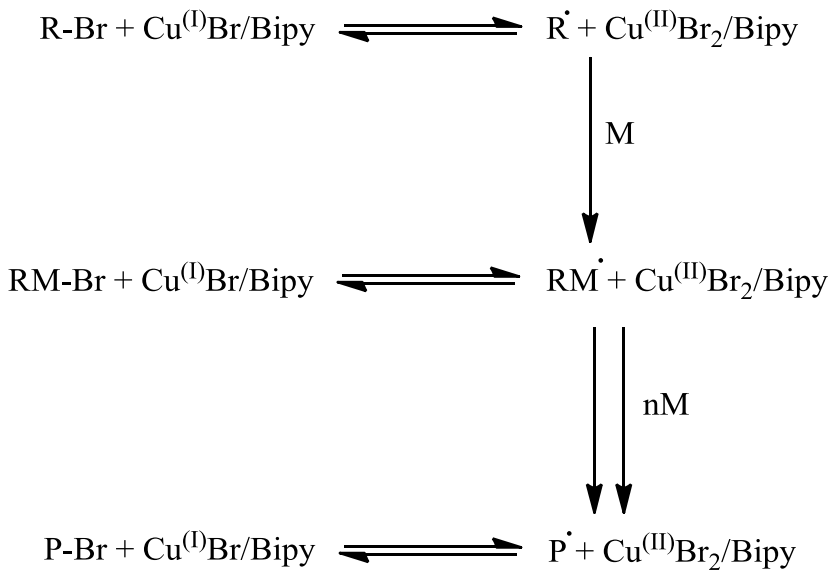

Figure 2.1: Reaction route for the initiation and propagation steps of a polymer grown by ATRP.

Samples were placed in Schlenk tubes and stoppered with a suba seal. The tubes were evacuated and then nitrogen purged, this cycle was repeated three times. In separated flasks, the solvent and monomer were degassed with nitrogen for 30 min. To the monomer, 2'2-bipyridine (bipy), Cu(I)Br and Cu(II)Br_2 were added. The mixture was degassed for 5 min before the solvent was added. The solid compounds were dissolved with aid of sonication. The solution was further degassed for 5 min before being added to the samples and left for varying time periods. The samples were rinsed and sonicated in the same solvent as used in the polymerisation solution.

2.7 Protein Immobilisation

Protein solutions were prepared by adding 10 uL of protein to 1 mL of PBS solution (10 mM). Immobilisation of the protein was carried out by submerging the sample into the protein solution. Samples were rinsed with PBS and de-ionised water to remove any non-adsorbed material and then dried under a stream of nitrogen.

2.8 Surface Patterning

Mask based photolithography

The micron-scale patterning of SAM substrates was performed with a HeCd laser (325 nm) and with a coherent Innova frequency doubled argon ion laser (244 nm). For both lasers, the beams were expanded to approximately 0.8 cm^2. After beam expansion the power output of the HeCd laser was measured as 12 mW and argon ion laser was measured as varied values between approximately 5 mW and 10 mW. Samples were rinsed with ethanol and dried with nitrogen before being placed under the laser beam. Square patterned electron microscope grids (Agar, Cambridge, UK), of sizes 2000 and 1000 (lines per inch), were place flat on top of the sample. A quartz disc was placed on top of the samples to hold the grids in position during the exposure.

Interference Lithography (IL)

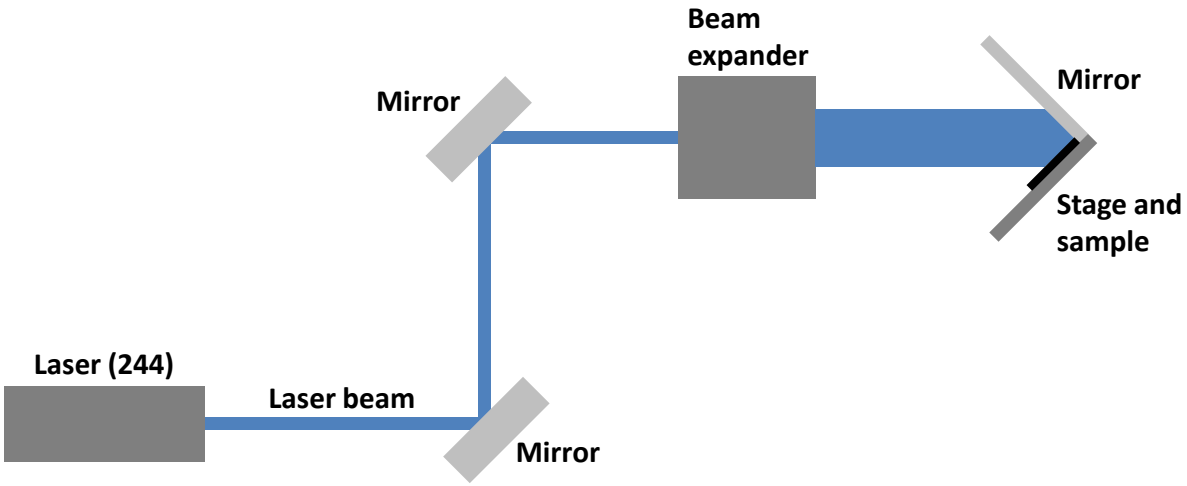

Figure 2.2: Schematic of the experimental setup used for interference lithography.

A frequency doubled argon ion laser limiting at 244 nm was used for IL. The power of the expanded beam was measured at varying values between 2 mW and 5mW. The experimental setup is shown in Figure 2.2. The sample is placed next to a mirror at a specified angle, the expanded laser beam is aligned so that only half of it lies on the samples and the other half hits the mirror and is reflected back onto the sample. The overlapping of the two halves of the beam produces an interference pattern of maximum and minimum intensities that can be

recorded in the photo-reactive NPPOC-silane monolayer. The period is dependent on the wavelength of light used as well as the angle at which it interferes.

Scanning Near-field Photolithography (SNP)

To perform SNP, a Witec SNOM alpha300 S, was coupled to a HeCd laser (325 nm). The laser is then aligned with the probe. Using a shutter, the laser beam is shut off while the sample is placed on the stage and the probe is moved into close proximity with the samples surface. A pre-designed pattern is selected on the Witec software, the laser shutter is opened manually when the probe starts to scan. Once scanning is finished, the probe is withdrawn and the sample is removed.

Nanoimprint Lithography (NIL)

Before the polymer is imprinted, it is first spin-coated onto a clean silicon or glass substrate. The mould being used also has to be coated with perfluorodecyltrichlorosilane (FDTS) by vapour deposition in a vacuum desiccator. This acts as a non-stick layer to ensure efficient separation of the mould and substrate after imprinting. NIL was performed using an Obducat Eitre® nano imprint system. The substrate is place on the loading tray with the mould placed on top of it, so that the polymer coated side of the substrate is in contact with the patterned face of the mould. A polycarbonate sleeve is placed on top. The temperature, pressure and time parameters are set, and then the imprinting is started. After imprinting the substrate is removed from the machine and then, using a sharp blade, the mould is carefully removed from the substrate.

2.9 Etching

Wet Etching

Wet etching methods were used to etch titanium after patterning of the ODPA resist layer by photolithography had occurred. Samples were immersed in cold piranha solution and kept at 30 °C using a water bath for approximately 25 min. The samples were then rinsed thoroughly with ultra-pure de-ionised water and ethanol. The end point of the etching was roughly determined by eye and then later confirmed by AFM.

Reactive Ion Etching (RIE)

RIE was used to etch patterned samples fabricated using NIL. Samples were etched using an Oxford Plasmalab 80 Plus. The samples are placed inside the chamber and then it is sealed and the air is evacuated to 5.5×10^{-5} torr. The pressure, power, time and gas flow parameters are set. The required gas(es) are pumped in and the process starts when the pressure is reached. The chamber is then vented and the samples removed.

2.10 Surface Analysis

Contact Angle

When a liquid drop is placed on a solid surface, the shape of the drop depends on the chemical interactions between the two materials and surrounding gas. At equilibrium the drop may be described by the Young's equation:

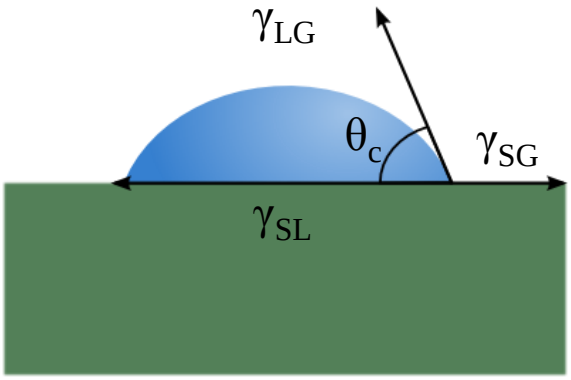

$$\gamma_{LG} cos\theta_C = \gamma_{SG} - \gamma_{SL}$$

Where θ_C is the contact angle and γ_{LG}, γ_{SG} and γ_{SL} are the free energies of the liquid-gas/vapour interface, solid-gas/vapour interface and solid-liquid interface respectively. The contact angle of a water drop can give a measure of how wetting the surface is. Figure 2.3 (a) represents a non-wetting, or hydrophobic surface. The contact angle is relatively large (> 90°) because the interaction between the liquid and the solid is unfavourable and hence it is more favourable for the liquid to resist the surface in the most efficient way. Figure 2.3 (b) represents a wetting, or hydrophilic surface. The contact angle in this case is relatively small (< 90°) because the interactions between the surface and liquid are more thermodynamically favourable.

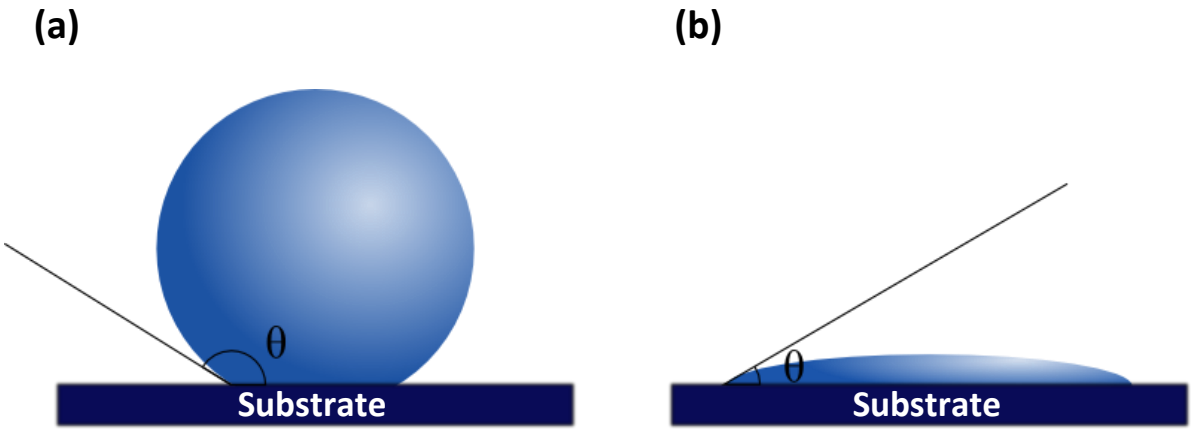

Figure 2.3: Schematic illustration of the variation in advancing water contact angle for (a) a hydrophobic surface and (b) a hydrophilic surface.

Contact angles were measured using a Rame-Hart goniometer by the sessile drop method. The sample stage was made level using a bulls-eye level, the sample was then placed on the stage. A water droplet (2 µL) was formed on the surface with a microliter syringe. The angle of the liquid-solid-gas/vapour interface was measure. Three measurements were taken for each sample in separate areas of the sample and the average value recorded.

Atomic Force Microscopy

AFM and FFM data was obtained with Digital Instruments Ltd Multimode Nanoscope IIIA and Nanoscope IV Atomic Microscope (Veeco, Santa Barbara, USA), equipped with a J scanner. Silicon nitride probes (Veeco Ltd) with an average spring constant of 0.06 Nm^{-1}, or 0.12 Nm^{-1} were used for contact mode. Crystal silicon probes (Veeco Ltd) with a spring constant of 20 – 80 Nm^{-1} were used for tapping mode.

Samples were rinsed with ethanol and dried under a stream of nitrogen, before being fixed to a specimen disc (12 mm, Ager) with adhesive tape. The samples were then mounted onto the magnetic scanner head. A probe was inserted onto the cantilever holder and clamped into position above the sample. The laser was then aligned with the end of the cantilever and the photo-detector. For tapping mode, the cantilever was tuned to acquire its resonant frequency. The sample was then moved into contact with the tip and the scan was initiated.

X-ray Photoelectron Spectroscopy (XPS)

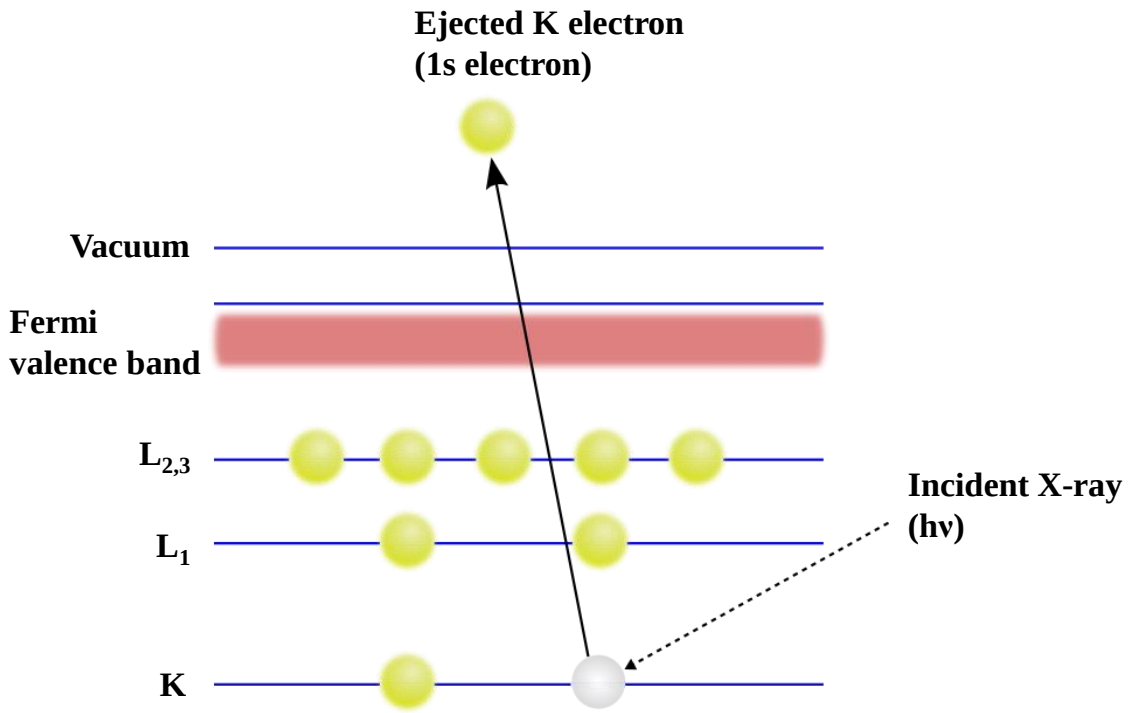

Figure 2.4: Schematic diagram of the XPS process, showing photoionisation of an atom by ejection of a 1s electron.

XPS, also known as electron spectroscopy for chemical analysis (ESCA), is one of the most widely used surface characterisation methods[158]. It can provide quantitative and qualitative information on all the elements (except H and He). In XPS an electron is ejected from a core level by an X-ray photon of energy (hν). The energy of the emitted photoelectrons is then detected and analysed by an electron spectrometer. The spectrometer measures the kinetic energy (E_k) of the electron, however this value is dependent on the energy of the X-ray photon which displaced the electron. The binding energy of the electron (E_B) is the parameter which is identifies the electron specifically[174]. The binding energy can be calculated from the relationship shown below:

$$E_B = h\nu - E_K - W$$

where hν is the photon energy, E_K is the kinetic energy of the electron and W is the spectrometer work function. The process of photoemission is illustrated in Figure 2.4. An electron from the K shell (i.e. 1s) is ejected from the atom and is then detected by the spectrometer. Electrons that escape without energy loss contribute to the characteristic peaks

in the spectrum. The electrons that suffer energy loss and inelastic scattering contribute to the background spectrum.

XPS analysis was performed using an Axis Ultra DLD equipped with a monochromated Al-K_α X-ray source. Samples 1 cm^2 or smaller were stuck to the specimen holder with double sided tape (for non-conducting samples, double sided carbon tape was used). The holder was then inserted into the loading chamber of the XPS machine and pumped down to a reduced pressure. When a low enough pressure is reached the holder is moved into the specimen chamber. Using the XPS software, the analysis possessions on each sample are recorded along with scan parameters. Once set up the spectrometer can be left to run. When completed the holder is moved from the specimen chamber back into the loading chamber and then removed.

Secondary Ion Mass Spectrometry (SIMS)

SIMS analysis and imaging was performed using a TOF.SIMS 5 equipped with an optimised Bi_n ion source.

Scanning Electron Microscopy (SEM)

SEM images were taken using a JEOL FESEM JSM6700F. Samples are first fixed onto a holder with double sided copper sticky-tape. Non-conductive samples are then sputter coated with a thin layer (approx. 20 nm) of gold. The holder is then placed into the exchange chamber, the chamber is evacuated. Once evacuated the holder is pushed manually into the specimen chamber. The sample can now be imaged in high resolution. After the images have been acquired, the holder is moved back into the exchange chamber and then removed from the machine.

Confocal Microscopy

A confocal microscope uses suitably positioned pinholes that only allow light from the plane of focus to reach the detector (see schematic Figure 2.5). This removes “out of focus” light, therefore improves the contrast and resolution of the images obtained compared to a conventional microscope.

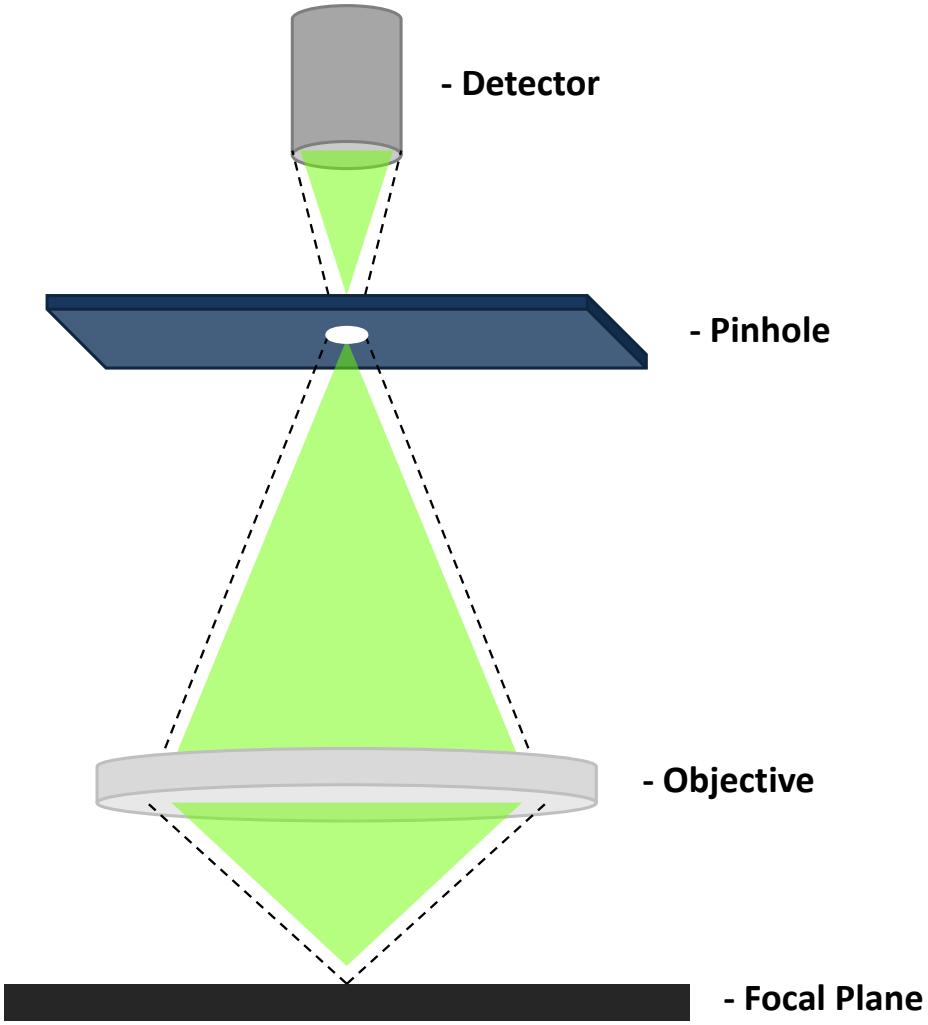

Figure 2.5: Schematic of a confocal pinhole.

Fluorescence images were acquired with a LSM 510 meta laser scanning confocal microscope (Carl Zeiss, Welwyn Garden City, UK). The sample was placed on a microscope slide followed by a drop of Citifluor, used as an antifade reagent (glycerol-PBS solution, AF1) (Citifluor Ltd., London, United Kingdom). Then a cover slip was placed on top, followed by a drop of immersion oil (Immersol 518 F, Zeiss) placed directly above the area of interest. 40x and 63x magnification oil dipping lens were used for imaging with numerical apertures of 1.30 and 1.40, respectively. The 488, 543 and 633 nm bands of Ar and HeNe lasers were used to excite the different fluorescent probes used. All fluorescence images were analysed using Zeiss LSM image browser software.

Chapter Three

3 Micro- and Nanoscale Fabrication of Non-Fouling Polymer Brushes by the Selective Deprotection of NPPOC-Silane Films

3.1 Introduction

Molecular nanolithography has continued to break new barriers with the development of new methodologies. However, major challenges still exist within the field, including the integration of top-down (lithographic) and bottom up (synthetic) fabrication at length scales between 100 nm and 1 nm. Scanning probe techniques such as DPN[56] and nanoshaving/nanografting[175] have demonstrated the ability to pattern molecules on length scales below 100 nm by physically depositing or removing material. However, they do not offer the ability to perform specific chemical transformations. One approach, developed by Sagiv and co-workers has been the development of constructive nanolithography,[80, 176] in which a potential difference is applied between an AFM tip and a surface to carry out oxidative modifications of organic films. Another approach is to use photochemical methods. Photocleavable protecting groups, specifically nitrobenzyl-based chemistry's, have been demonstrated as useful tools in synthesis[177, 178]. The development of light-directed chemical synthesis[38] by Fodor *et al*, combined photocleavable protecting groups with photolithographic methods to carry out spatially defined solid-state synthesis. SNP has demonstrated the ability to pattern photo-reactive molecules with sub-100 nm[47]. A scanning probe is used to illuminate a surface in the near-field, thus beating the diffraction limit. Although the technique is serial in nature, it is able to produce 2D patterns with a wide range of geometries, limited only in size by the scanning area of the machine. Additionally, control over the scan speed can add 3D characteristics to a pattern. One non-serial technique that can potentially perform specific chemical transformations with nanometre resolution over relatively large areas is IL[41], in which two overlapping beams of light interfere to yield an interference pattern composed of regions of high and low intensity that can be used to modify a photo-reactive film. For an adequately powerful laser, expansion of the beam to expose a large area is feasible. Using IL in conjunction with photo-chemical methods can offer a way to pattern molecules and biomolecules with nanoscale resolution over macroscopic areas. Additionally, it is a relatively cheap, easy and fast process. However, a main limitation is that it is only possible to fabricate periodic arrays.

Currently there is a significant demand for the development of non-fouling materials for applications such as drug delivery, biomaterials and biosensors[179]. Some of the most widely studied non-fouling materials including poly(ethylene glycol) (PEG) and materials based on oligomeric(ethylene glycol) (OEG), such as OEG-terminated self assembled monolayers[14,

[180]. A common way to fabricate a PEG surface is to first coat the surface in gold and then use a OEG-thiol SAM to coat the surface, but they have limited robustness[181]. Another approach which offers more flexibility is to covalently attach a PEG chain capped with a reactive functional group to a complimentary capped surface (grafting-to). This allows for a range of different PEG molecules to be used and tested. However, the grafting-to approach can lead to a low density of coverage which can affect the non-fouling properties of the PEG layer[182]. Another grafting method that produces high density coverage is the grafting-from approach. This method is commonly carried out by SI-ATRP. SI-ATRP has been well studied and there are many examples in the literature[183-186]. A surface can be functionalised with a radical initiator, often in the form of an alkyl halide, from which a polymer can grow. The grafting-from approach offers a much higher density of PEG coverage, because it involves the repeated addition of small monomers rather than a large and sterically bulky oligomer or polymer, as in the grafting-to approach. A polymer *brush* structure is not a direct consequence of the grafting-from approach. The formation of a brush is dependent on the grafting density of the polymer chains. A transition exists between a single grafted chain (at low grafting density), referred to as a "mushroom" structure, and a brush structure (at high grafting density). It is generally recognised that three regimes occur in brush formation: (1) the mushroom regime, (2) the cross-over or transition regime, and (3) the highly stretched brush regime[187]. In real systems the transition between a single grafted polymer and a brush is not sharp, because of the statistical characteristics of grafting and polydispersity of the tethered chains, resulting in fluctuation across a surface in the average distance between grafting points[188]. The issue of grafting density has been addressed by Wu *et al*[189, 190]. They formed a density gradient of initiator on a silicon wafer and from it grow polyacrylamide (PAAm) by ATRP. Their results showed that at low grafting densities the PAAm thickness was independent of grafting density, indicating that the polymer chains were in the mushroom regime. Conversely at high grafting densities the thickness of the PAAm film increased with increasing grafting density, indicating a brush regime. The effects of initiator density on polymer brush growth has also been addressed by Jones *et al*[191]. They used a system of mixed SAMs to create surfaces with varying initiator concentrations on gold coated mica and from them grow PMMA by ATRP. They observed an almost linear increase in PMMA thickness with increasing initiator concentration. However, when the cross-sectional area of the polymer chains was measured they found that on a surface of 100% initiator each polymer chain was expected to cover 10-12 initiator molecules. If this was true, then the

PMMA thickness on mixed SAMs between 10% and 100% initiator, should be similar[192]. They concluded that this discrepancy could possibly be explained by poor initiator efficiency at the start of the reaction.

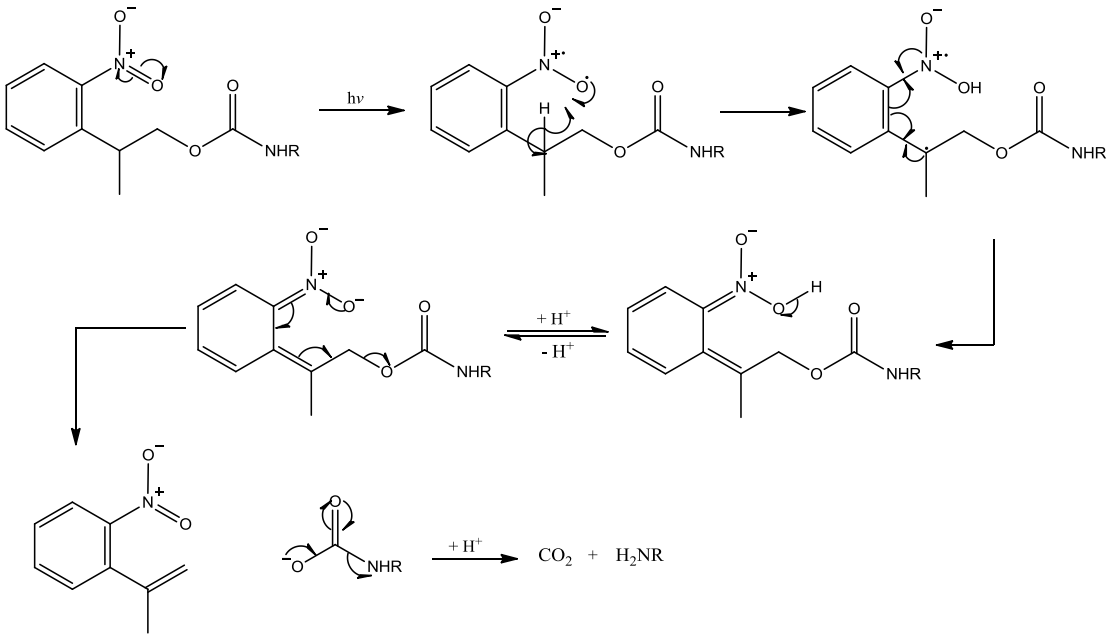

Figure 3.1: Supposed mechanism for the deprotection of the NPPOC group by a β-hydride elimination reaction initiated by irradiation of UV light.

Nitrophenylpropyloxycarbonyl (NPPOC) photocleavable protecting groups can be used to block amines[193]. Films of NPPOC protected aminosilanes (NPPOC-silane) can be formed on a substrate and photo-patterned with UV light. The proposed mechanism of deprotection is shown in *Figure 3.1*. From the deprotected regions of the film the resulting aminopropylsiloxane (APS) can be derivatised with a radical initiator and then a polymer grown from the regions by ATRP (see schematic Figure 3.2).

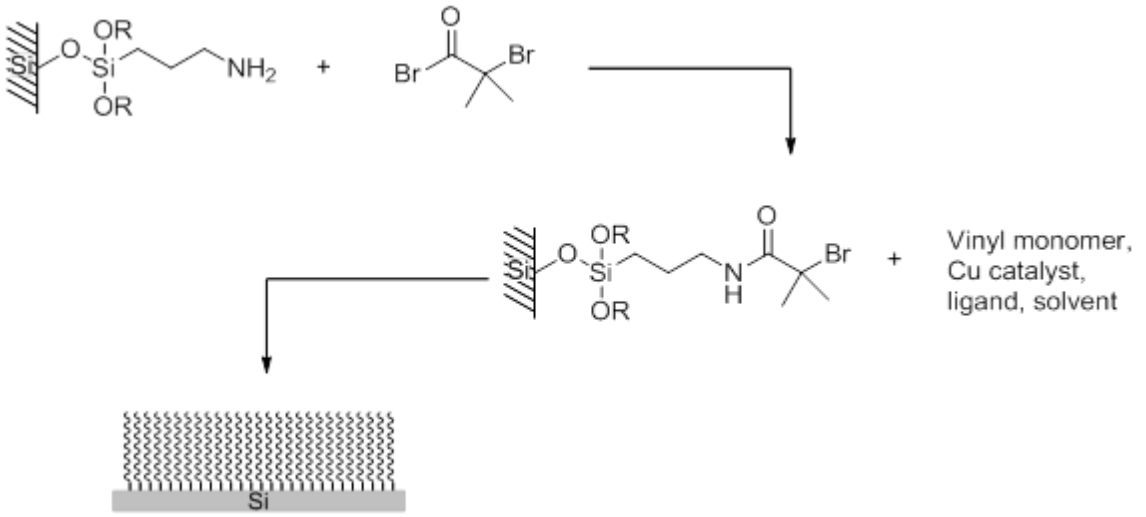

Figure 3.2: Schematic showing an established route to grow polymer brushes via SI-ATRP. An amino functionalised surface is derivatised with BIBB and then immersed into a polymerisation solution.

In the present chapter photolithographic methods are used to pattern an NPPOC-silane film for use as a template for the fabrication of polyOEGMA structures. PolyOEGMA is based on a methacrylate backbone with OEG side chains that extend out, relative to the backbone. Deprotection of the NPPOC group at 244 nm and 325 nm wavelengths is compared. The polymerisation of OEGMA by SI-ATRP is examined in both water and methanol solutions. Micro- and nanoscale polymer brush patterns are fabricated and characterised by AFM. The use of IL to fabricate periodic nanoscale regions of polyOEGMA over macroscopic areas is examined. SNP is used to form dual-functional patterns, in order to study the polymers structure with varying grafting density and size.

3.2 Experimental

NPPOC-silane Film Formation

A detailed explanation of the reaction steps and procedures involved in the synthesis of NPPOC-silane are described in section 2.2.

Glass slides were cleaned by piranha and RCA solutions as described in section 2.3. The NPPOC-silane films were formed on glass substrates by immersion in a solution of the adsorbate in dry toluene under a nitrogen atmosphere for 48 h, as described in section 2.4.

Surface photochemistry and Patterning

Photodeprotection and patterning were carried out by exposing samples to light with wavelengths of either 325 nm or 244 nm from a He-Cd (Kimmon IK3202R-D) laser and a Coherent Innova 300C frequency doubled argon ion laser respectively. For unpatterned exposure and mask patterns, the power was 50.4 mW cm^{-2} at 325 nm light and 21.0 mW cm^{-2} at 244 nm. TEM grids were used as masks, and were held in place by a quartz crystal placed between the sample and the light source.

Interferometric patterns were made using a Lloyd's mirror setup irradiating at 244 nm, which consisted of a sample stage and a mirror set at approximately 80° to each other and an expanded laser beam (1 cm diameter approx.) positioned so that half was exposing the sample and half illuminating the mirror.

SNP was conducted by coupling a 325 nm light source to an AlphaSNOM scanning near-field optical microscope (WiTec, Ulm, Germany). WiTec AlphaSNOM cantilever-type probes were used (WiTec, Ulm, Germany).

Surface Initiated Atom Transfer Radical Polymerisation

The initiator molecule, BIBB, was covalently bonded to the primary amines on the surface as described in section 2.5.

Reagent/Reactant	Molecular Weight / g	Molar Ratio	Amount (for 1 g of monomer) / mg
OEGMA	475	60	1000
Bipy	156.2	2.8	15.3
$Cu^{(I)}Br$	143.5	1	5
$Cu^{(II)}Br_2$	223.5	0.3	2.5

Table 3.1: Molar ratios and quantities of reactants used in the SI-ATRP of OEGMA.

Polymer was grown form the initiator terminated surface by submersion of the substrate into a polymerisation solution. The contents and ratios of the polymerisation solution are given in Table 3.1. All vessels and liquids were thoroughly degassed with nitrogen before the addition of the $Cu^{(I)}$ catalyst.

Protein Adsorption

Samples were immersed in a solution of IgG-FITC in PBS for up to 2 h and rinsed thoroughly with PBS. A more detailed procedure is described in section 2.7.

Surface Characterisation

Contact angle measurement were carried out in triplicates and averaged. In XPS analysis, wide scans were collected at 160 eV and narrow scans at 80 eV. All AFM analysis was carry out in dry conditions using Si_3N_4 tips.

3.3 Results and Discussion

The contact angle of a clean glass slide was found to be 10°. Following film formation with NPPOC-silane the water contact angle was measured to be 76°, which is consistent with formation of an organic film. Figure 3.3 (a) shows the C 1s region of a glass slide after deposition of NPPOC-silane. Three components were fitted to the C 1s spectrum, corresponding to ring and aliphatic carbons (285.0 eV), carbons singularly bonded to nitrogen or oxygen (286.3) and the carboxylate carbon. The relative areas of the three components are displayed in Table 3.2, together with the calculated composition.

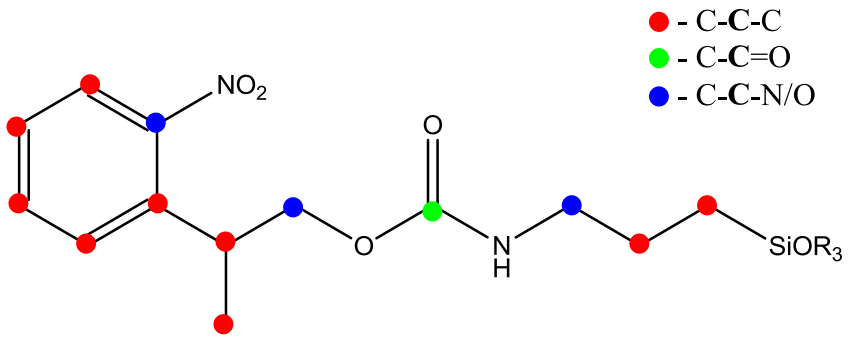

The two carbons bonded to nitrogens and the one carbon bonded to oxygen have been treated as having the same environment in this case, because there is a small difference between their chemical shifts so two separate peaks could not be fitted accurately. The percentage composition measured by XPS is in good agreement with the expected values determined by the structure.

Carbon environment	% Composition	Ratio	% Comp. Measured by XPS	Ratio
C-**C**-C	69.2	9	68.1	9
C-**C**-N/O	23.1	3	24.3	3
C-**C**=O	7.7	1	7.6	1

Table 3.2: Composition of different carbon environments in the NPPOC-silane molecule and the values measured by XPS.

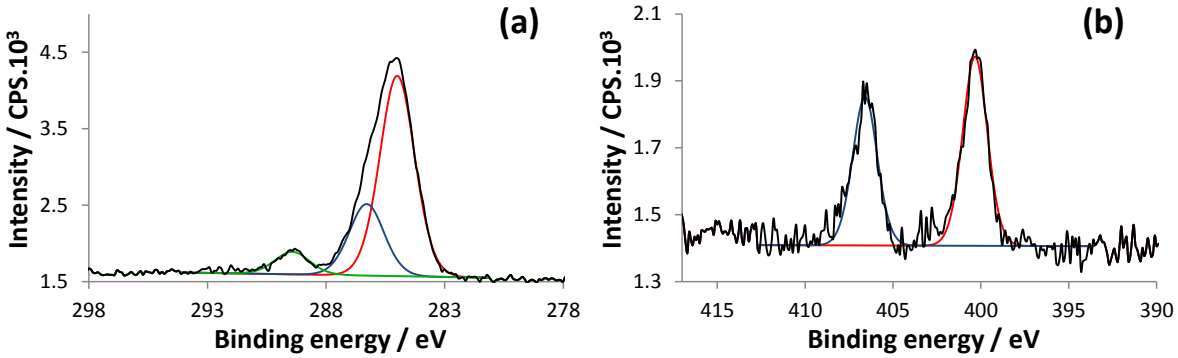

Figure 3.3: XPS narrow scans of an NPPOC-silane SAM on silicon oxide, showing the (a) C 1s region and (b) N 1s region.

Figure 3.3 (b) shows the N 1s region of the XPS spectrum. Two components are observed, corresponding to the nitrogen atoms in the nitro group (406.2 eV) and the carbamate group (400.0 eV). The ratio of the NHR, where R is either a carbon (protected form) or hydrogen (deprotected form), and NO_2 peaks is 0.78, but the calculated value is 1. This discrepancy is attributed to reduction of the NO_2 group under irradiation by X-rays[194, 195].

Photo-deprotection

Figure 3.4 (a) shows the variation in water contact angle of the NPPOC protected silane films following exposure to wavelengths of 244 nm and 325 nm. Following exposure to UV light, a drop in contact angle was observed for both wavelengths, consistent with the loss of the NPPOC group and production of an amine surface. It is clear from Figure 3.4 that the rate of photo-deprotection is much greater for exposure at 244 nm. After a dose of 0.63 J cm^{-2} at 244 nm the contact angle drops sharply from 73° to 58°. By comparison, a dose of 12.1 J cm^{-2} is required to achieve a similar contact angle while irradiating at 325 nm. It is also clear from the graph that irradiation with 244 nm produces a more hydrophilic surface. At 325 nm, the

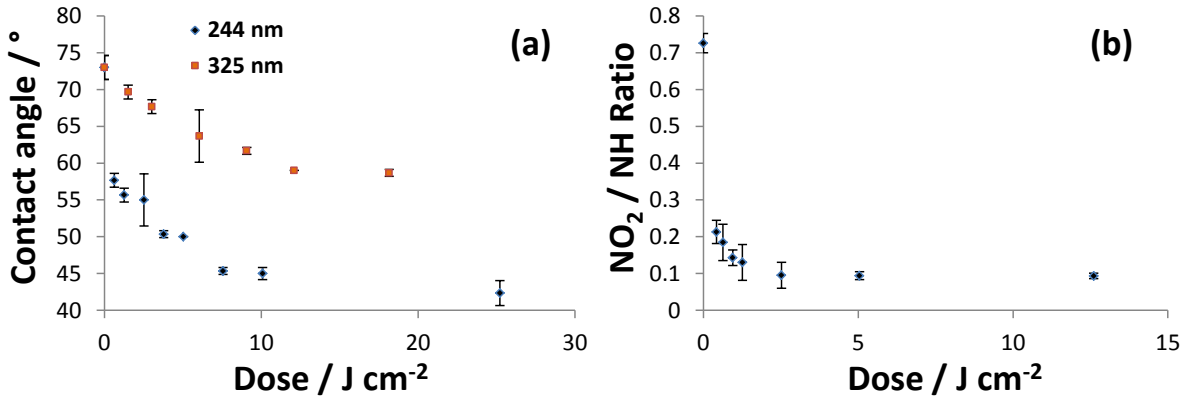

Figure 3.4: Graph showing (a) the drop in water contact angle after exposure to 244 nm light compared with exposure to 325 nm light (b) the variation in peak ratio of NO_2 to NH measured by XPS after continuous exposure to 244 nm.

contact angle reaches a minimum value of 57°, whereas exposures at 244 nm yields a limiting contact angle of 45°. The water contact angle measured from films of APTES, which are isostructural with the deprotected adsorbate under discussion, can range from 40° to 60° depending on the preparation conditions and therefore is not a good comparison for determining which wavelength produces the correct contact angle. One explanation for the difference in contact angles measured from the different wavelengths, is that during the deposition of the NPPOC protected silane SAMs, multi layers could form generating a rougher surface. The higher energy 244 nm wavelength could essentially "burn through" any multilayer regions producing a smoother surface making it more wetting[196, 197]. Another explanation is that on high exposures of 244 nm, a significant degree of photo-induced oxidation of the organic material could occur, producing oxygen bound species that would inevitably make the surface more hydrophilic and thus more wetting. This in fact is one of the main concerns with using 244 nm light, as it is of high enough energy to decompose organic material[198].

XPS analysis was used to quantify the loss of NPPOC and determine if there was any undesirable decomposition of the film or any photo-oxidation. The NPPOC-silane molecule has two distinctive nitrogen environments, a nitro group and a carbamate group (which is transformed to an amine following removal of the NPPOC protecting group). Since the nitro group is removed as part of the photo-deprotection process a clear way to quantify the removal of NPPOC is to track the loss of the nitro peak in the XPS spectrum. Figure 3.4 (b) shows the variation in peak ratio between the two nitrogen environments. It can be seen from

the graph that the ratio drops dramatically after only a small exposure, consistent with the contact angle measurements, and then reaches a minimum of about 0.1 after a dose of 2.52 J cm^{-2} which corresponds to a contact angle of 55°. Interestingly, although doses greater than 2.52 J cm^{-2} do not show a further reduction in the N 1s peak ratios, the contact angle continues to fall by a further 10°. This suggests that on continued exposure by 244 nm wavelengths, a side reaction that produces hydrophilic species may occur.

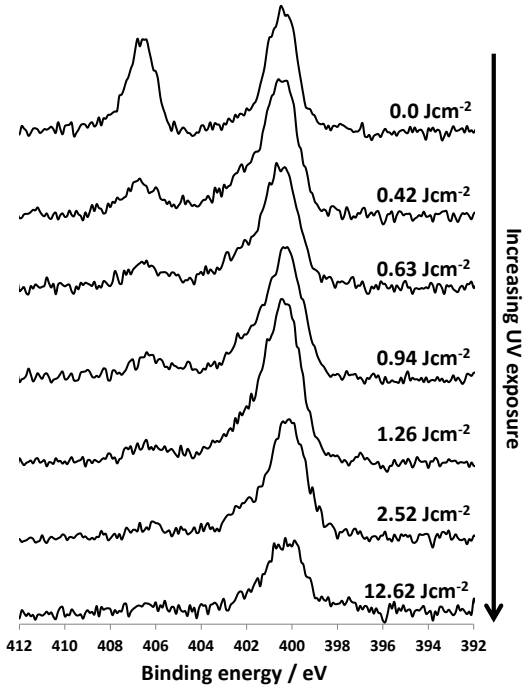

Figure 3.5: Variation in the N 1s region of the XPS spectrum as a function of UV exposure at 244 nm.

The variation of the N 1s region can clearly be seen in Figure 3.5, which shows the loss of the nitro peak at 406 eV with increasing exposure. To determine if there was any photo-degradation of the amine group by exposure to the 244 nm wavelengths, the area of the peaks at 400 eV were plotted against exposure dose and is shown in Figure 3.6. For exposure doses up to 2.52 J cm^{-2} there are no significant changes in the peak areas and no obvious trend in the data. At an exposure dose of 12.62 J cm^{-2} the peak area was measured to be substantially lower than the rest of the peaks, suggesting that there could have been some removal of the amine from the surface, induced by the high dose of 244 nm wavelengths.

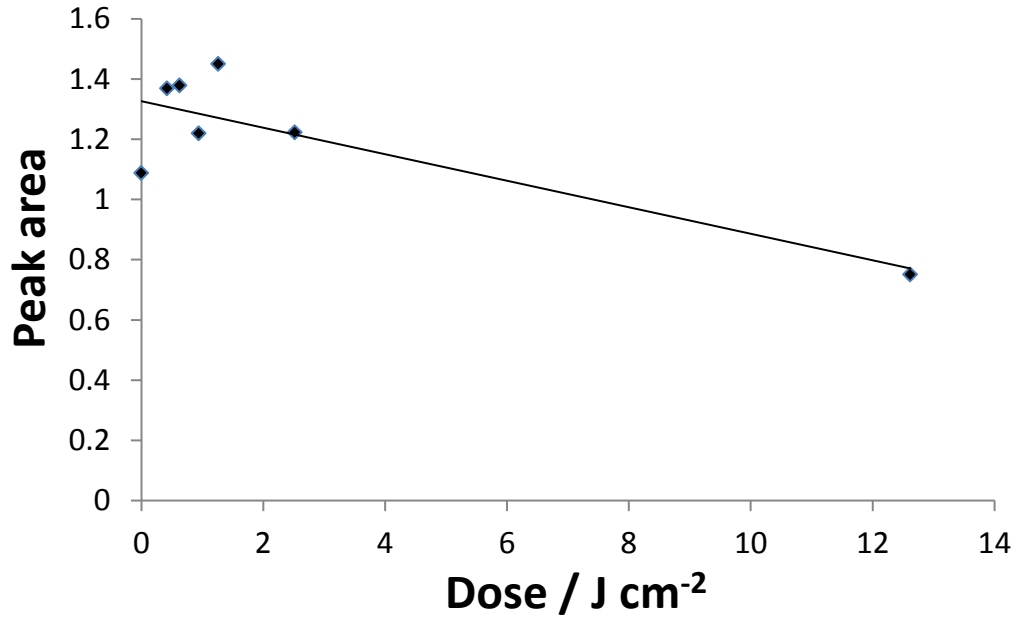

Figure 3.6: Graph plotting the area of the peak at 400 eV measured from XPS spectra against exposure dose.

Surface Initiator Attachment

Prior to derivatisation, the APS film gave a water contact angle of 55°. Following the reaction with the initiator, BIBB, the angle increased to an average of 67° which is consistent with the formation of a halogenated surface[199]. XPS was also used to study the initiator attachment. Figure 3.7 shows Br 3d regions of samples (a) before and (b) after derivatisation with BIBB. The substantial peak present in Figure 3.7 (b) at 70.9 eV, which corresponds to a bromine atom, confirms attachment of the ATRP initiator[200].

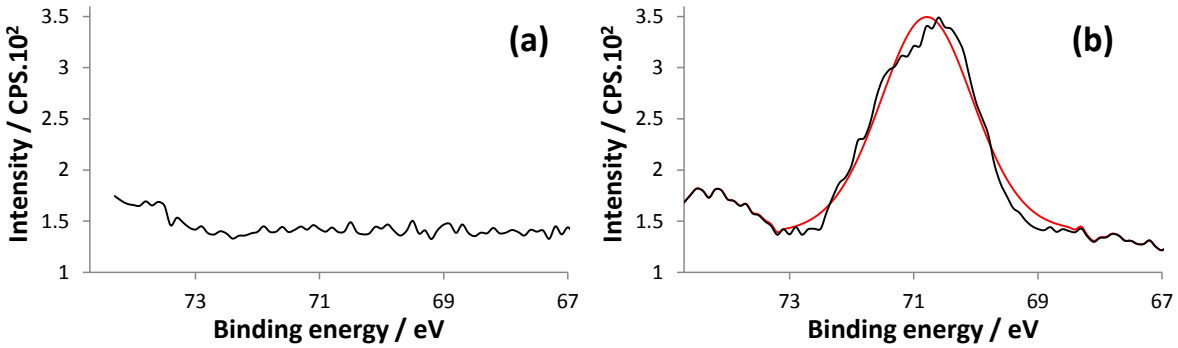

Figure 3.7: Br 3d region of an XPS spectrum of a sample of (a) photo-deprotected NPPOC-silane and (b) following derivatisation with BIBB.

Surface Initiated Atom Transfer Radical Polymerisation

Following initiator attachment to APS, the samples were immersed into a polymerisation solution consisting of OEGMA, bipy, $Cu^{(I)}Br$ and $Cu^{(II)}Br_2$. SI-ATRP was carried out in methanol and in water and the results analysed by XPS to compare the effect of the two solvents on the polymerisation yield and rate. Figure 3.8 (a) shows the C 1s region of the initiated surface prior to polymerisation. Figure 3.8 (b) shows the C 1s region measured from a sample after polymerisation in a water medium for 30 min. Three components were fitted, corresponding to aliphatic carbons (285.0 eV), ether carbons (286.5 eV) and the carboxylate carbon (288.8 eV). The percentage of composition of the three components is displayed in Table 3.3 along with the actual percentage composition determined from the structure of the poly-OEGMA unit shown below:

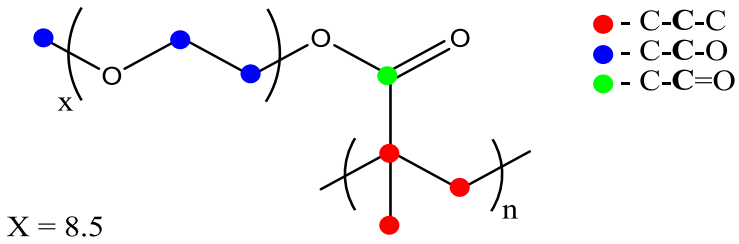

The percentages of composition measured by XPS are in good agreement with the actual values. However, when the ratios are compared, it becomes evident that ratio of ether carbons is less than expected for the OEGMA polymer. This suggested that there is a contribution from the underlying APS molecules to the detected signal. This could be either because the polymer film is not as thick as the vertical detection resolution of the XPS technique (ca. 10 nm), or that the polymer brush is of a low enough density to permit detection of the underlying surface through it.

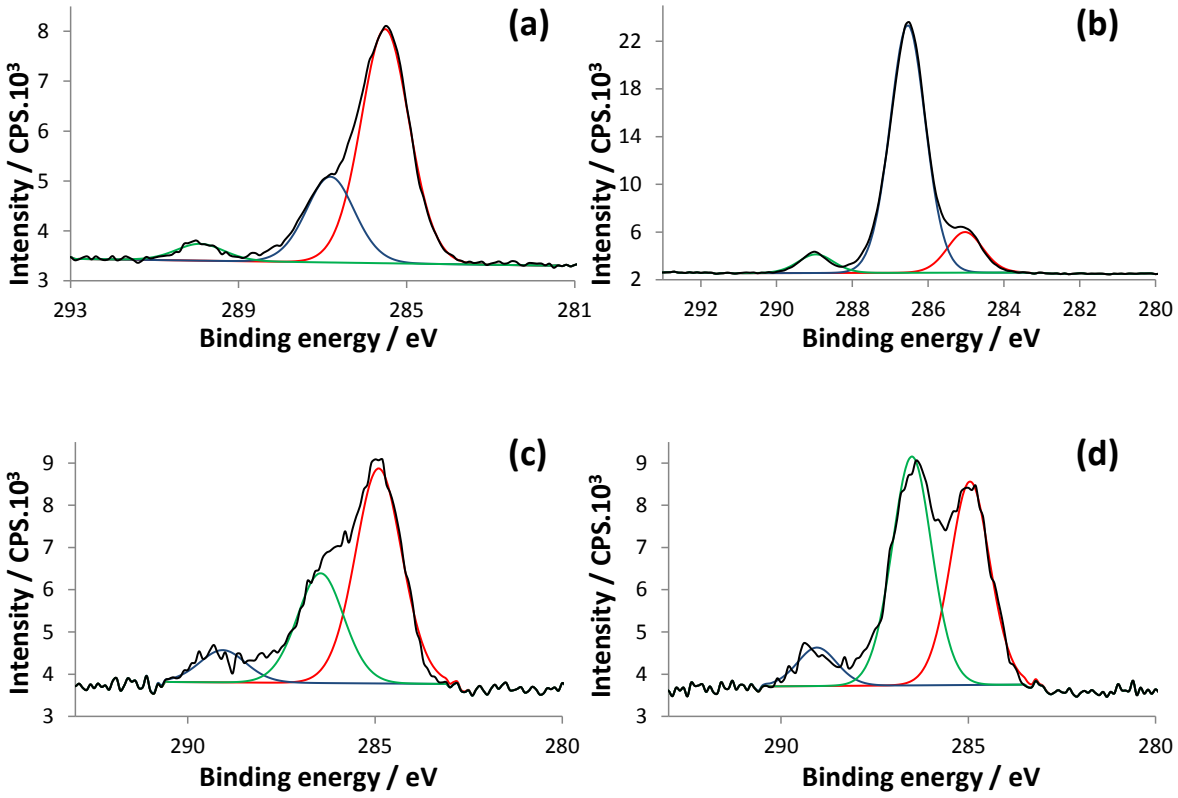

Figure 3.8: C 1s region of XPS spectra of (a) an APS film derivatised with BIBB, (b) following SI-ATRP of OEGMA in water for 30 min, (c) in methanol for 30 min and (d) in methanol for 150 min.

Polymerisation in methanol was carried out for the same reaction time of 30 min. The corresponding XPS C 1s spectrum is shown in Figure 3.8 (c) in which only a very small increase in the ether component is observed. Therefore, the polymerisation time was extended. Figure 3.8 (d) shows the C 1s region of an OEGMA brush grown in a methanol medium for 150 min. A clear increase of the size of the peak at 286.5 eV can be observed when compared to spectra (a) and (c), suggesting that some polymerisation has occurred. However, the size of the peak is considerably smaller than the equivalent peak measured in spectrum (b), even though the reaction time was 5 times as long. Consequently, all subsequent polymerisations were carried out using water as the solvent as it clearly gave the better polymerisation yield at a faster rate.

Carbon Environment	% Composition	Ratio	% Comp. Measured by XPS	Ratio
C-**C**-C	13.6	3	15.0	2.6
C-**C**-O	81.8	18	79.2	13.7
C-**C**=O	4.5	1	5.8	1

Table 3.3: Composition of carbon environments of poly(OEGMA) compared with the values measured by XPS of a brush grown in water for 30 min.

Mask Patterns

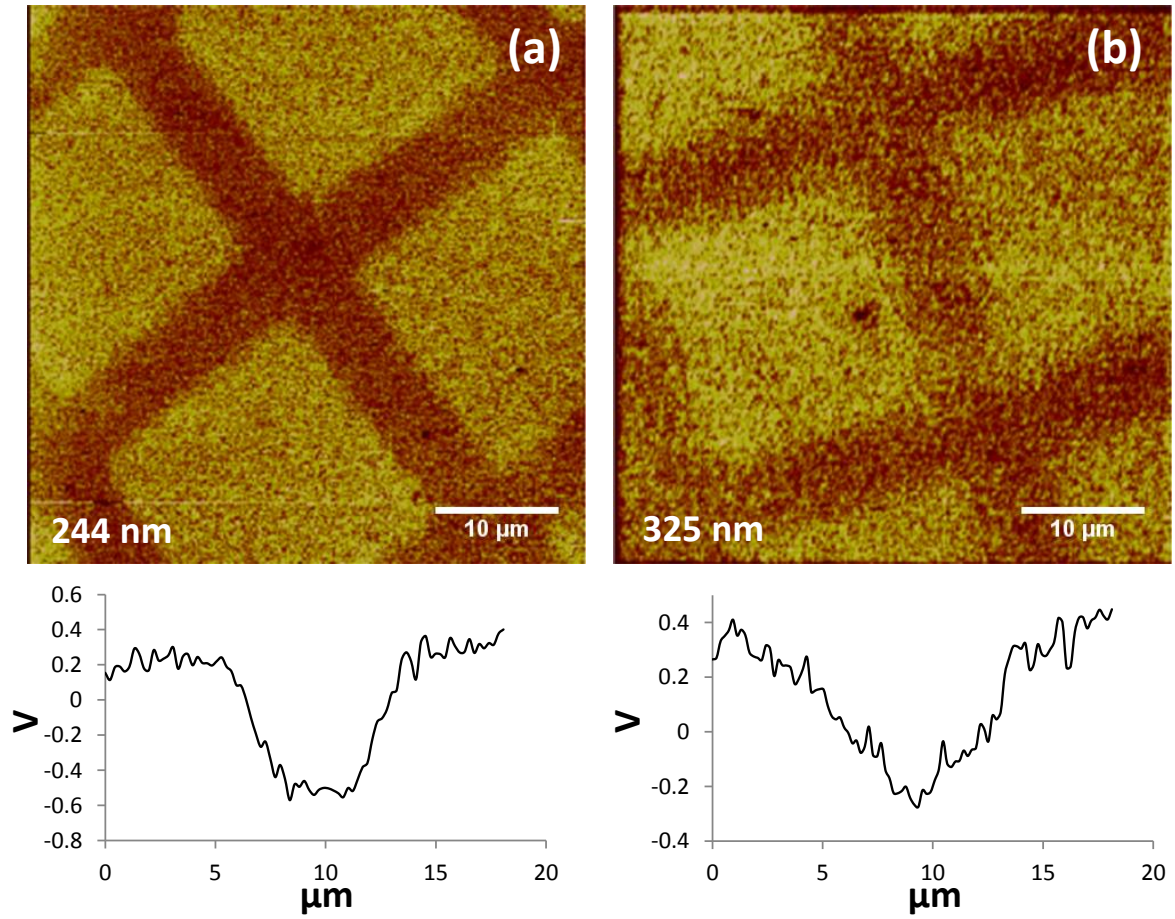

Figure 3.9: 45 µm x 45 µm FFM images of photo-patterned NPPOC-silane film exposed with (a) 244 nm for 1.89 J cm^{-2} (b) 325 nm for 9.09 J cm^{-2}.

NPPOC-silane samples were micropatterned by exposing the samples to UV light through a TEM grid. Areas of the sample exposed to the light are altered chemically, by removal of the NPPOC protecting group, yielding an amine surface. The exposed amine and NPPOC-

protected regions of the patterned surface were characterised by FFM and SIMS. Figure 3.9 (a) and (b) are FFM images and corresponding line-sections of two micropatterned NPPOC-silane films. Image (a) was produced by a 1.89 J cm^{-2} exposure with 244 nm light and image (b) was produced by a 9.09 J cm^{-2} exposure with 325 nm light. In both images, distinct regions of squares (UV exposed) and bars (masked) can be detected, indicating a difference in surface energy between the regions. The brighter contrast observed for the square regions relative to the bars, indicates a higher friction force interaction with the polar silicon nitride tip (Si_3N_4). This is consistent with the formation of an amine surface contrasted with an NPPOC surface since the amine surface is more polar (confirmed by a lower water contact angle) and will have more interaction with the polar tip. This is in agreement with a large body of literature correlating frictional behaviour with surface free energy of organic materials[201, 202]. The pattern produced by exposure to 244 nm wavelengths is significantly better defined, suggesting that there is a larger difference in fictional contrast between the two regions. From the line-sections (below image) the difference in friction between the square and bar regions was measured to be approx. 0.9 V and 0.5 V for the patterns produced by 244 nm and 325 nm wavelengths respectively. The larger difference, measured for the 244 nm patterned sample, is consistent with the contact angle data, shown in Figure 3.4 (a), in which the exposed surface yields a lower water contact angle when using 244 nm wavelengths relative to 325 nm wavelengths, suggesting more polar groups.

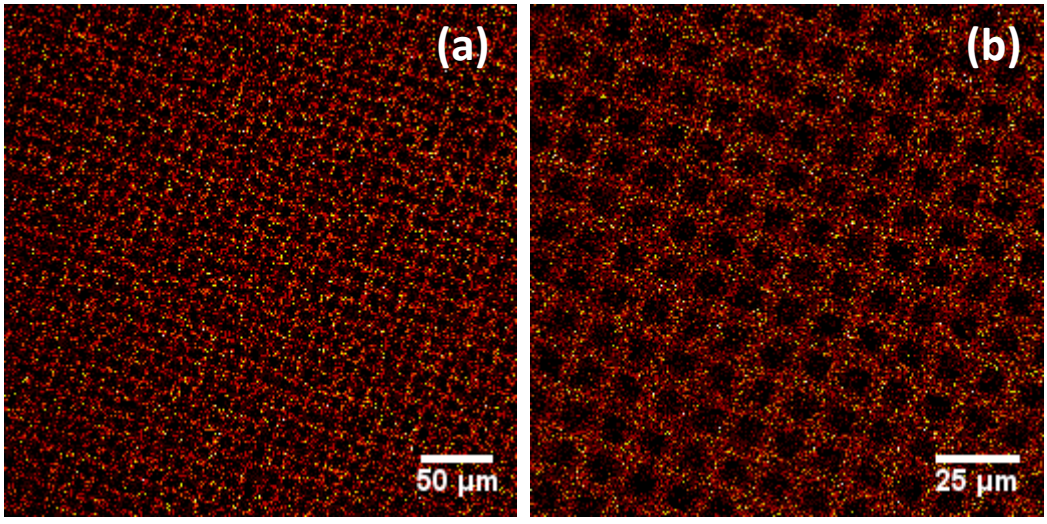

Figure 3.10: SIMS images of mask patterned NPPOC-silane film with 244 nm, showing m/z 46 which corresponds to the NO_2 group. (a) 350 µm x 350 µm (b) 150 µm x 150 µm.

Figure 3.10 shows SIMS images of the mask patterned NPPOC-silane films. The images display the distribution of the m/z 46 ion, NO_2^-, which is a good indication of the NPPOC functional group. The images show high concentrations of NO_2 along the bars and very low concentrations within the square regions, which is consistent with the loss of the NPPOC group within exposed areas. The signal detected in the square regions is extremely weak, and can be disregarded as noise because of the very high detection limit of SIMS.

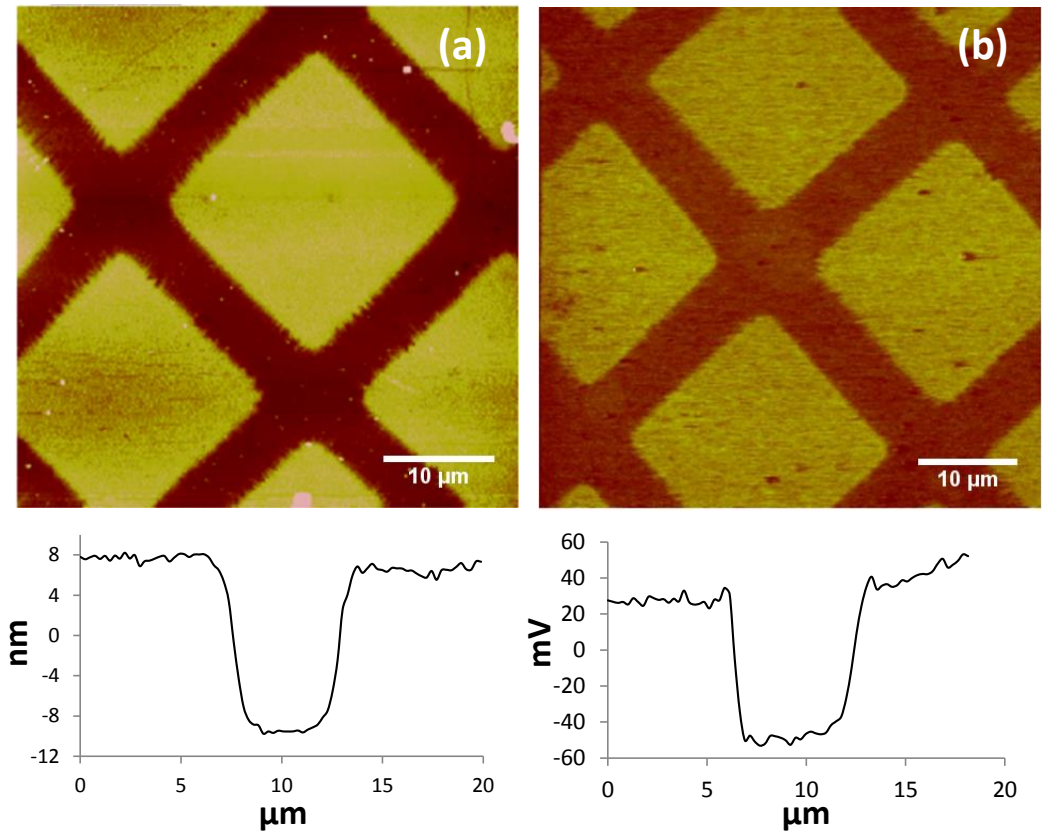

Figure 3.11: 50 µm x 50 µm AFM images and corresponding line-sections of an NPPOC-silane film mask patterned with UV light then derivatised with initiator and immersed into a polymerisation solution of OEGMA for 10 min, showing (a) tapping mode height contrast and (b) contact mode friction contrast.

Following patterning of the NPPOC-silane film, the deprotected regions can be derivatised with initiator and consequently, a polymer brush can be selectively grown from the initiated regions of the surface. Figure 3.11 (a) is a tapping mode AFM image of polyOEGMA brush grown from an NPPOC-silane film micropatterned by irradiation with 244 nm. The bright squares correspond to the regions of polymer brush, which are surrounded by darker bars containing unmodified NPPOC-silane. From the line-section (below image) the height

difference between the square and bar regions was measured to be approx. 17 nm. Figure 3.11 (b) is an FFM image of the same sample and shows a visible difference in contrast between the square and bar regions. The contrast difference between the exposed and unexposed areas was measured from the line-section (below image) to be approx. 80 mV. This value is more than 10x smaller than the frictional difference measure between the APS and NPPOC surface shown in Figure 3.9 (a), despite the water contact angles of the APS and polyOEGMA surfaces being very similar (ca. 45°). Explanations for this could include the deprotection of the NPPOC regions by ambient light during the reactions subsequent to mask patterning or contamination of the surface by polyOEGMA that has formed in solution. Both instances would result in a more homologous surface.

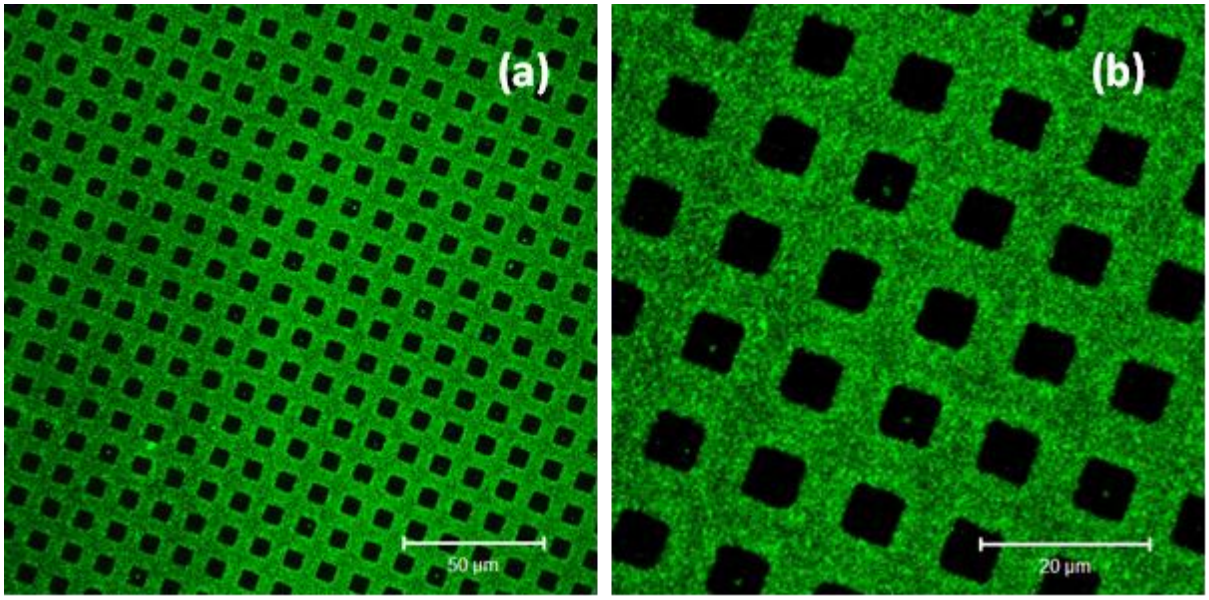

Figure 3.12: Fluorescent images of IgG-FITC protein adsorbed on an NPPOC sample mask patterned with 244 nm laser and polyOEGMA brush grown from exposed square regions. (a) 210 um x 210 um. (b) 70 um x 70 um.

An important property of the OEGMA brush structures is that they can resist the adsorption of proteins in solution. This ability was investigated by screening an unpatterned polyOEGMA brush sample for non-specific protein adsorption. After immersion in a protein solution, the surface was imaged by laser scanning confocal microscopy and as expected no fluorescents signal was observed. Fluorescent images of protein adsorbed onto a surface with patterned polyOEGMA brush structures have also been produced and are shown in Figure 3.12. Regions of green fluorescent bars, corresponding to the adsorbed protein, surrounding black squares, corresponding to the polyOEGMA brushes, are clearly defined. The high

degree of contrast in intensity between the bar and square regions indicates the protein adsorbed specifically to areas not containing polyOEGMA brushes.

IL Patterning

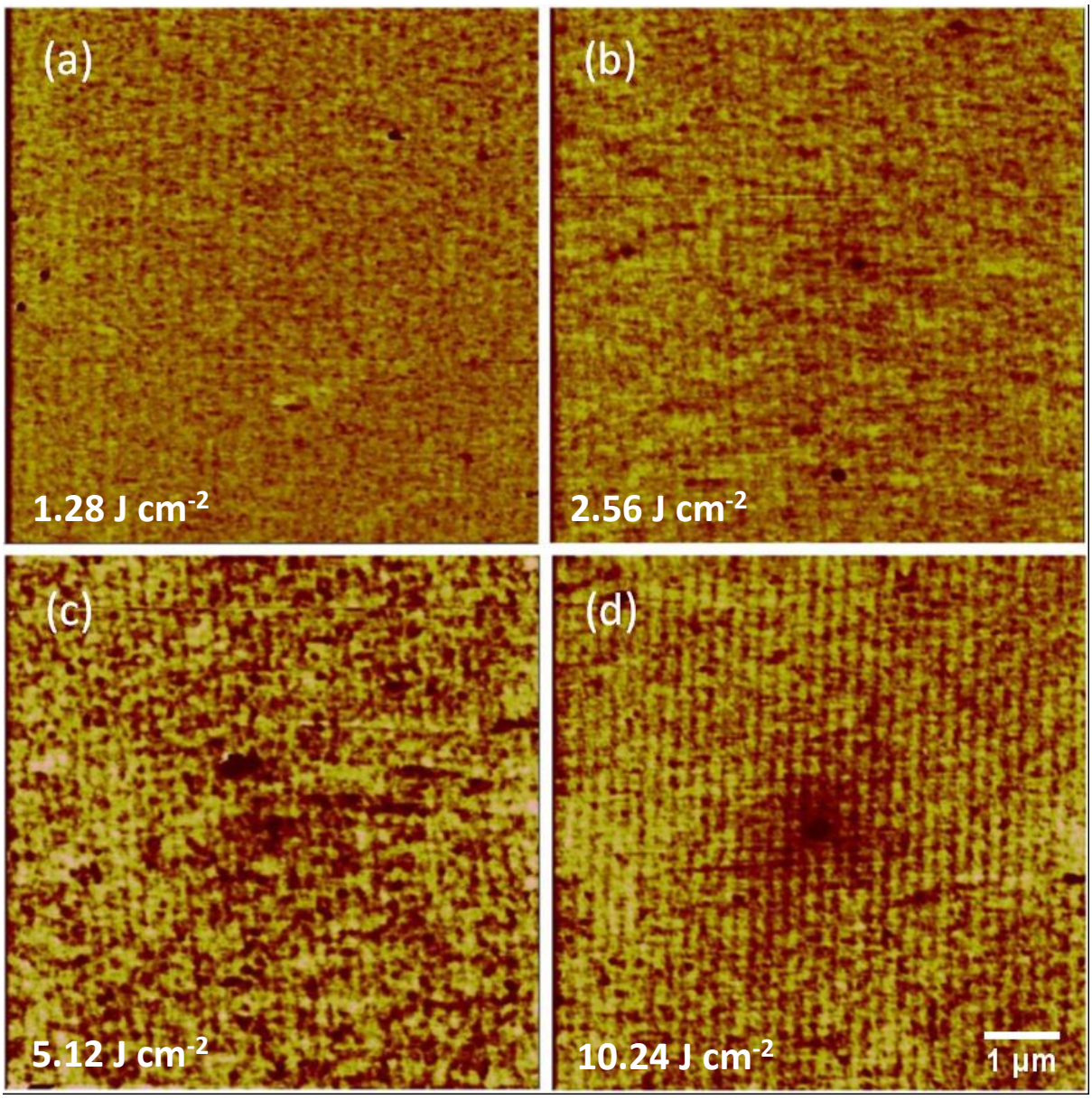

Figure 3.13: 7 µm x 7 µm FFM images taken at 0.3 V of IL patterned NPPOC-silane films with exposures of (a) 1.28 J cm^{-2} (b) 2.56 J cm^{-2} (c) 5.12 J cm^{-2} (d) 10.24 J cm^{-2} (the doses stated are for a laser powers recorded prior to interference. The interference of the beam will cause localised maxima and minima).

Large-area, periodic nano-patterns were produced by exposing samples of NPPOC-silane to an interferogram, produced by a Lloyd's Mirror from a beam of light from a frequency-

doubled argon ion laser (244 nm). The samples were irradiated at varying doses and the effects were analysed using FFM (Figure 3.13 (a – d)). The period was ca. 205 nm. The contrast between the exposed and unexposed lines becomes more pronounced with increasing exposure. This is because with increasing exposure the density of amines formed within the exposed regions increases. No significant change in the thickness is evident. However, the array of lines becomes clearer with increasing dose, there is no determinable change in the widths of the lines at the different exposure doses, which were measured to be approx. 135 nm for the exposed (bright contrast) and approx. 70 nm for the unexposed (darker contrast). Most likely this is because the majority of NPPOC is removed at relatively low exposures. Subsequently the deprotection rate drops and much larger exposures are required to remove the remaining NPPOC protecting group, as illustrated in Figure 3.4 (b), which shows that 80% of NPPOC is removed after an exposure of just 0.42 J cm^{-2}, but a further 2.12 J cm^{-2} is required to reach the minimum NPPOC level. This is a consequence of the sinusoidal variation in the intensities of illumination across the interferogram.

Following IL of the NPPOC-silane film, the deprotected regions were derivatised with the polymerisation initiator, BIBB, from which polyOEGMA chains were grown. Figure 3.14 (a – d) shows AFM height images of IL patterns of polyOEGMA brush grown from samples subjected to a range of exposures. Lines of bright contrast correspond to the polymer brushes grown from exposed regions of the pattern. Samples exposed to doses above 1.0 J cm^{-2} did not produce a pattern and exposures below 0.15 J cm^{-2} were not attempted. From image (a) to (d), the contrast difference between regions exposed to maxima and minima in the interferogram decreases. This suggests that the height difference between the two regions decreases. The explanation is that the width of the brush regions increases as the extent of the surface modification between maxima increases. Eventually, at large exposures, some brushes start to form close to the minima (see schematic Figure 3.15). Interestingly, the largest height measured for the polymer line was approx. 1.5 nm measured form the 0.15 J cm^{-2} exposure dose sample. This value is significantly smaller that the height difference measured for the micron pattern of 17 nm (shown in Figure 3.11 (a)), despite the samples being submitted to the same polymerisation conditions. This is thought to be because the nanometre lateral dimensions of the polymer lines in conjunction with the relatively low grafting density (a result of the low exposure doses used) effects the ability of the individual polymer chains to pack close enough to form a brush and consequently collapse down onto the surface.

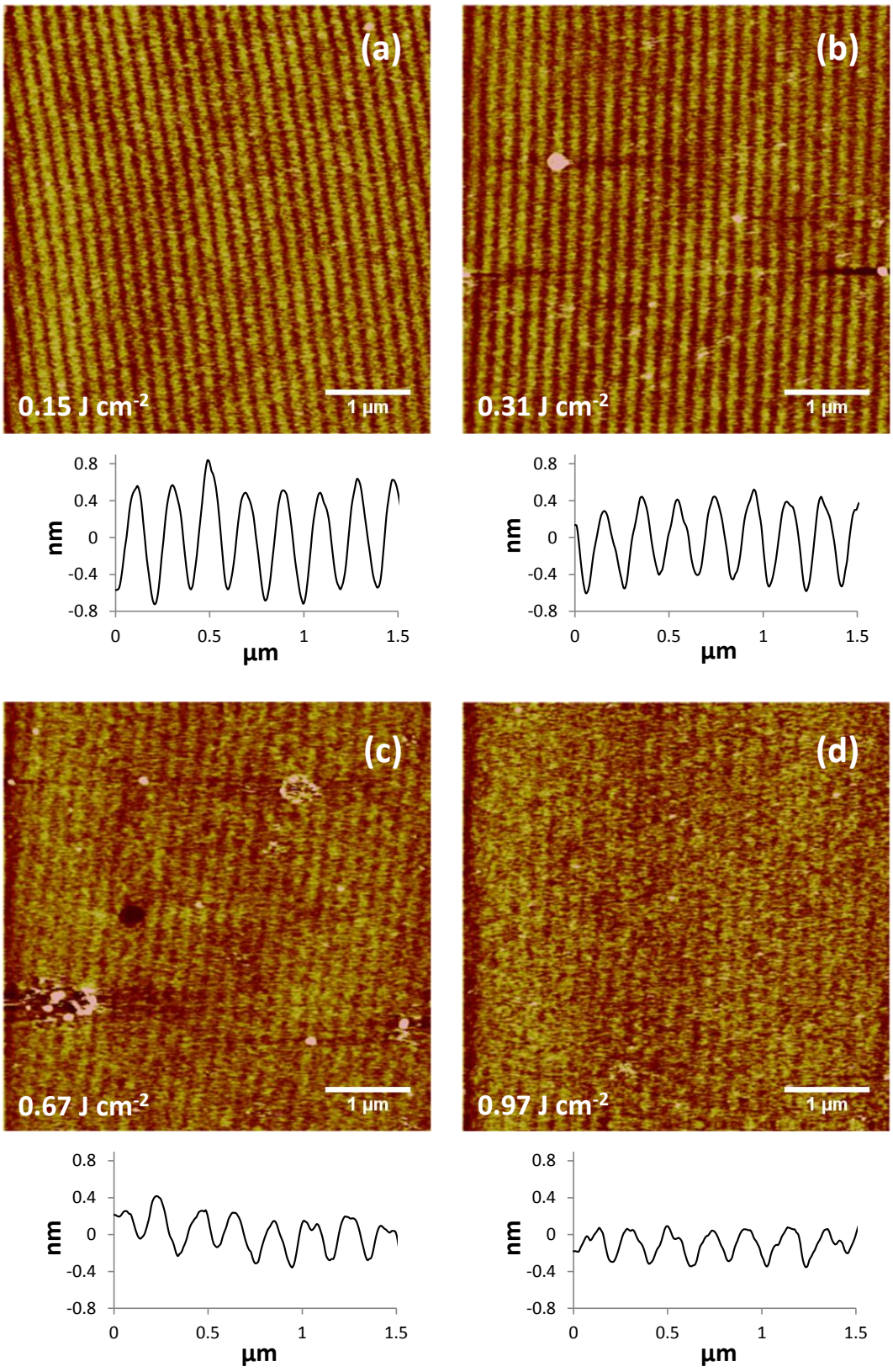

Figure 3.14: 5 µm x 5 µm AFM height images and corresponding line-sections of OEGMA brushes grown from IL patterned NPPOC-silane films at varying exposure doses of (a) 0.15 J cm^{-2}, (b) 0.31 J cm^{-2}, (c) 0.67 J cm^{-2} and (d) 0.97 J cm^{-2}.

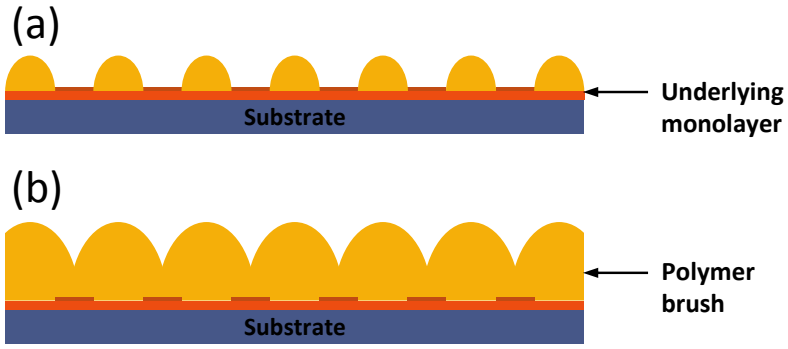

Figure 3.15: Schematic representation of two structures consistent with the AFM data. (a) individual polymer brush domains separated by regions of the underlying monolayer, (b) a continuous layer of polymer brush with topographic features mimicking the underlying patterned monolayer.

Patterns were also fabricated by repeated exposures, with the second exposure carried out at 90° to the first. The surface of patterned NPPOC-silane was characterised by FFM (image not shown). It was not possible to observe a periodic pattern in the photoreactive film, possibly because of the small contrast difference in friction observed between the NPPOC and APS regions, making detection of such small features challenging. However, following initiator attachment and subsequent growth of polyOEGMA the surface was characterised by tapping mode AFM which yielded height contrast showing a periodic pattern (Figure 3.16 (a) and (b)). Image (a) and (b) show patterns produced from two perpendicular exposures of 0.15 J cm^{-2} and 0.31 J cm^{-2} respectively. In both images, an array of connected bright dots surrounded by darker dots can be deduced. The brighter contrast in the images corresponds to the polymer brush grown from the exposed regions. The pattern forms dots of polymer, rather than two sets of parallel lines perpendicular to each other, because at the points where the two perpendicular exposures cross, the NPPOC-silane film receives a double dose of intensity, resulting in a broader area of exposure and a greater density of deprotection. The corresponding line-sections (below images) show a similar trend, as seen in Figure 3.14, of decreasing polymer height with increasing exposure dose, which can be explained by the same reasoning given previously.

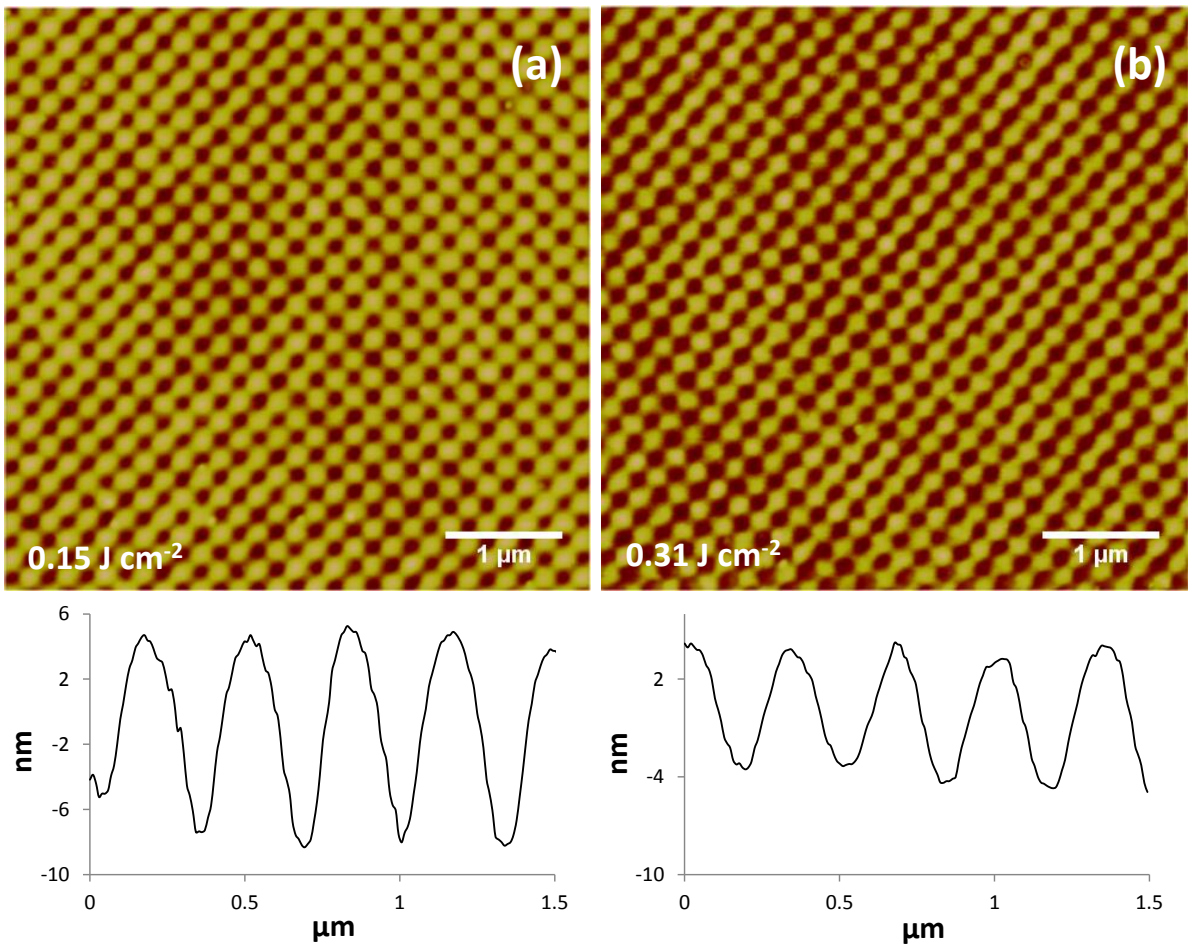

Figure 3.16: 5 µm x 5 µm AFM height images and corresponding line-sections of an OEGMA brush grown from an initiated NPPOC-silane film patterned by a double exposure at 90°, with doses of (a) 0.15 J cm^{-2} and (b)0.31 J cm^{-2} .

The IL patterns of polyOEGMA are a demonstration of nanofabrication. However, the period of the array patterns is too small for an accurate characterisation of them. AFM was sufficient enough to provide clear images and data of the topography of the patterned polymer, but is not able to clearly determine whether the area between the polymer regions is NPPOC-silane or just a thinner layer of polymer. Adsorption of proteins onto the IL patterns was not carried out because of the resolution of the patterned features were beyond the limits of detection by conventional confocal microscopy.

SNP Patterning

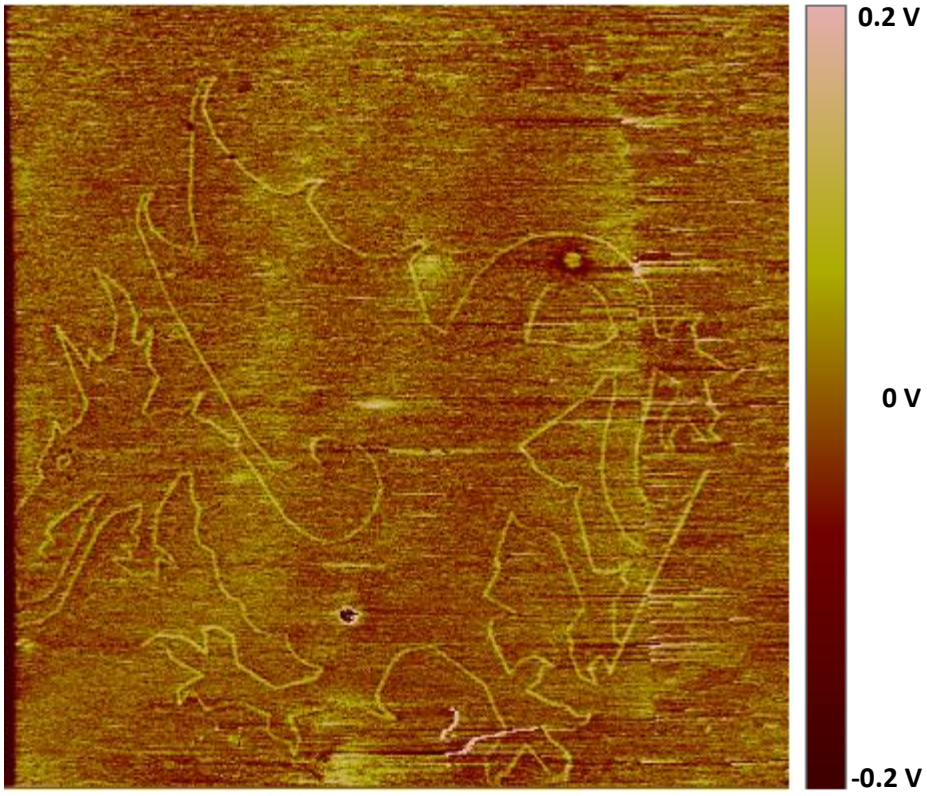

Figure 3.17: 60 µm x 60 µm FFM image of a dragon picture drawn by SNP into a NPPOC-silane film using 325 nm wavelengths at a scan speed of 100 nm s^{-1}. The line of deprotected NPPOC-silane was derivatised with adipoyl chloride to enhance the contrast difference.

From the previous experiments, in which polyOEGMA was grown from interference patterns recoded into the NPPOC-silane film, the nanoscale structures of polymer appeared to be much shorter than in the case of a micron scale structure of polymer. However, it was not determined accurately because the polymer lines were too close together, which made accurate measurements and determinations of the surface pattern imprecise. It was thought that if individual lines of polymer were fabricated, it would make the characterisation of the polymer more accurate. This was achieved with SNP using 325 nm wavelengths.

Prior to any polymerisation steps, an NPPOC-silane film was patterned by SNP and characterised by FFM as shown in Figure 3.17, in which an outline of a dragon has been drawn in the film. The resulting line of APS has been derivatised with adipoyl chloride to enhance the frictional contrast. The line width was measured to be approx. 300 nm. However,

the diameter of the aperture used for the experiment was specified as being in the region of 100 nm. Therefore, either the aperture was larger than the specified value, or a significant amount broadening in the exposed area has occurred during the photolithographic process. A relatively large distance between the probe and the surface during SNP could cause a broadening of the exposure area, by an interaction with the far-field as opposed to the near-field. Reflected light between the surface and the probe could also have caused a broadening of the exposure area, the extent of which would be affected by the probe-surface distance. The probe-surface distance was not known, but was controlled by a fixed applied force measured by the deflection in the cantilever, thus it was able to be kept constant for all scans. Therefore, all scans were assumed to have the same exposure width of 300 nm.

For patterns of polymer brush, it was a goal to fabricate individual lines for analysis, in order to investigate the structural properties of the nanoscale polymer structures - in particular, how they varied with the grafting density and lateral dimensions. Films with controlled, variable densities of initiators were fabricated by SNP. An advantage of the scanning probe technique utilised in this experiment is its ability to fabricate multifunctional patterns on the same area, so that direct correlations can be made between them. This is illustrated in Figure 3.18, which is an AFM tapping mode image showing the height contrast of parallel lines of polyOEGMA grown form two sets of line patterns, in which a different variable is being changed in each set. The left side of the image shows an array of 8 lines fabricated with increasing exposure (going from left to right), achieved by decreasing the scan speed. The lines also decrease in length, but this is not expected to change any properties of the polymer. It was used as a guide for the correct determination of each line. The right side of the image shows an array of 6 lines with increasing exposure widths (going from left to right), that was achieved by scanning an increasing number of lines separated by 100 nm (see schematic Figure 3.19). The distinctions for the two patterns have been clarified by the annotations in Figure 3.18.

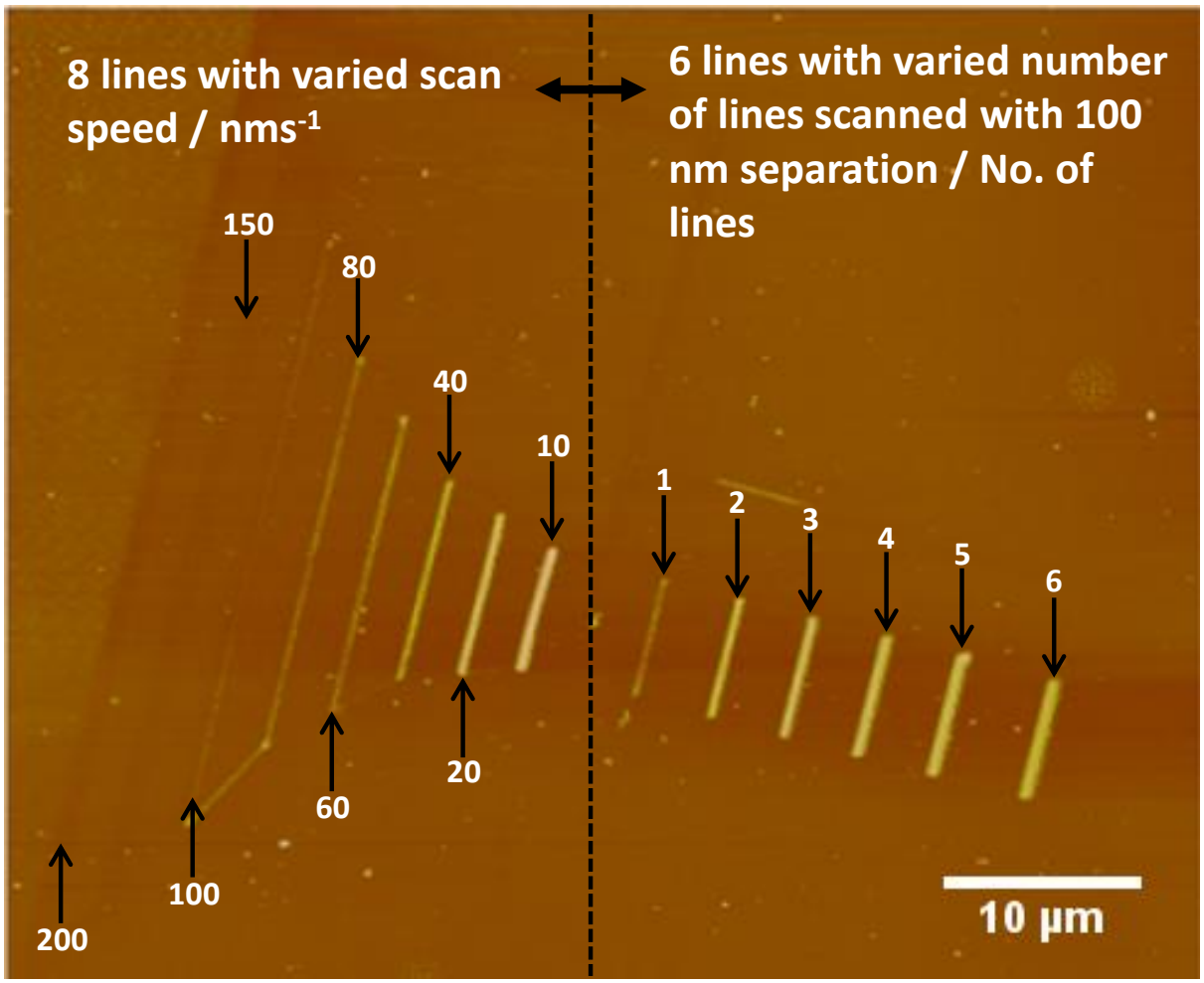

Figure 3.18: AFM tapping mode image showing the height contrast of an array of parallel lines of polyOEGMA, grafted from a bifunctional pattern fabricated by SNP into a NPPOC-silane film. The array of 8 line to the left of the image were scanned at different speeds; the array of 6 lines to the right of the image were scanned at a constant scan speed of 60 nm s^{-1}, a different number of times, with each scan within a line separated by 100 nm, e.g. the line to the far right of the image was produced by scanning 6 separate lines, each 100 nm apart. The annotations on the image show the relative scan speeds (left pattern) and number of scans (right pattern).

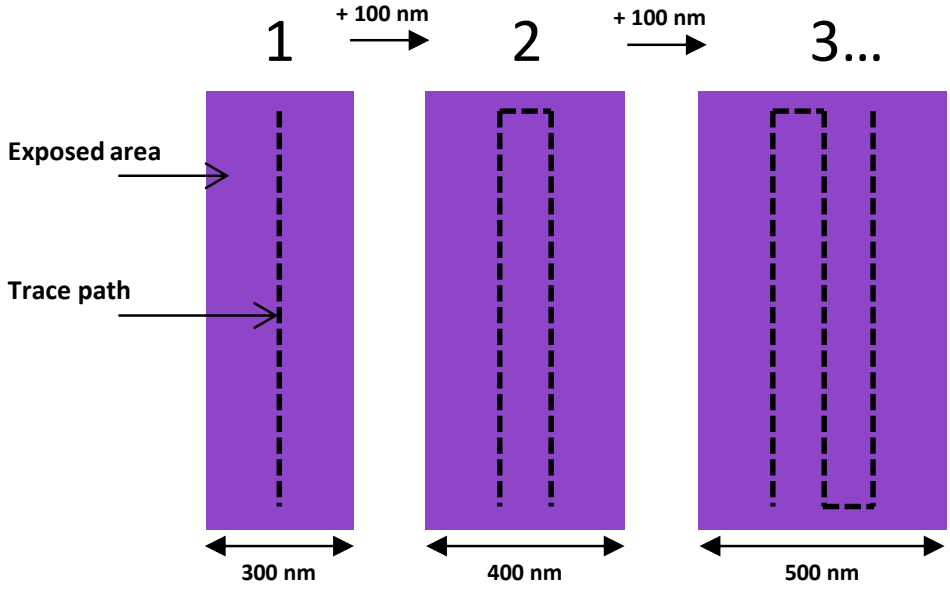

Figure 3.19: Schematic showing the trace path exposure width of the scanning probe for the pattern of 6 lines with increasing line width.

Figure 3.20 (a) and (b) are AFM tapping mode images and corresponding line-sections of the 8 line array scanned with varied speed, showing height and phase contrast respectively. From the known scan speeds it is possible to calculate the exposure dose applied to each line using equations **1** and **2** shown below.

$$t = \frac{A}{V} \quad (1)$$

$$D = \frac{P}{A} . t \quad (2)$$

Where **t** (s) is the exposure time, **A** (cm^2) is the area of the exposure (7.1×10^{-10} from 300 nm diameter), **V** ($cm\ s^{-1}$) is the scan speed, **P** (W) is the power measured by a photometer (3.0×10^{-10} W), and **D** ($J\ cm^{-2}$) is the exposure dose. The calculated exposure doses are given in Table 3.4.

Line length / µm	Line Height / nm	Scan Speed / nm s^{-1}	Exposure Dose / J cm^{-2}
6	68.6	10	12.73
8	55.9	20	6.37
10	30.6	40	3.18
15	15.1	60	2.12
20	8.3	80	1.59
30	1.5	100	1.27
40	0	150	0.85
50	0	200	0.64

Table 3.4: Data corresponding to the array of 8 lines scanned at varying speeds with 325 nm wavelength.

Line sections across and the heights of the features were measured. Figure 3.20 (a) shows that the line height decreased with decreasing exposure. This is because as the exposure decreases a smaller percentage of the NPPOC protecting groups are removed, which results in less initiator becoming bonded to the exposed region and hence a lower grafting density of polymer. It is thought that as the grafting density decreases there is less pressure on the individual chains, allowing them to coil and relax nearer to the surface, ultimately resulting in a reduction in height. Interestingly, the two fastest scanned lines, with exposures of 0.85 J cm^{-2} and 0.64 J cm^{-2}, do not show a positive height difference, suggesting that very little or no NPPOC was removed at these doses. However, the lines are still visible, because they exhibit a small negative height difference. This is thought to be caused by a compression of the silane film by the probe as it is traced over surface. This phenomenon is often observed when scanning an organic film with an AFM in contact mode. Further evidence of this hypothesis is given in the phase contrast shown in Figure 3.20 (b). The phase contrast is related to the local energy dissipation on the surface, in which brighter contrast usually corresponds to harder materials when the interaction between the tip and the surface is dominated by repulsive forces. In the phase image the lines containing polymer are clearly

displayed as dark contrast compared with the surrounding NPPOC-silane film. This can be explained by the thicker polymer film having more material to dissipate energy. The lines that were scanned at higher speeds appear as brighter contrast compared to the surrounding NPPOC-silane. This is constant with the compression of the organic film, thus making it super stiff compared to the uncompressed film surrounding the pattern. The brighter contrast can also be seen either side of the three lines in the centre of the pattern scanned with doses of 1.27 J cm^{-2}, 1.59 J cm^{-2} and 2.12 J cm^{-2}, in which the same effect of compression has occurred, but has only been partially covered by the polyOEGMA chains.

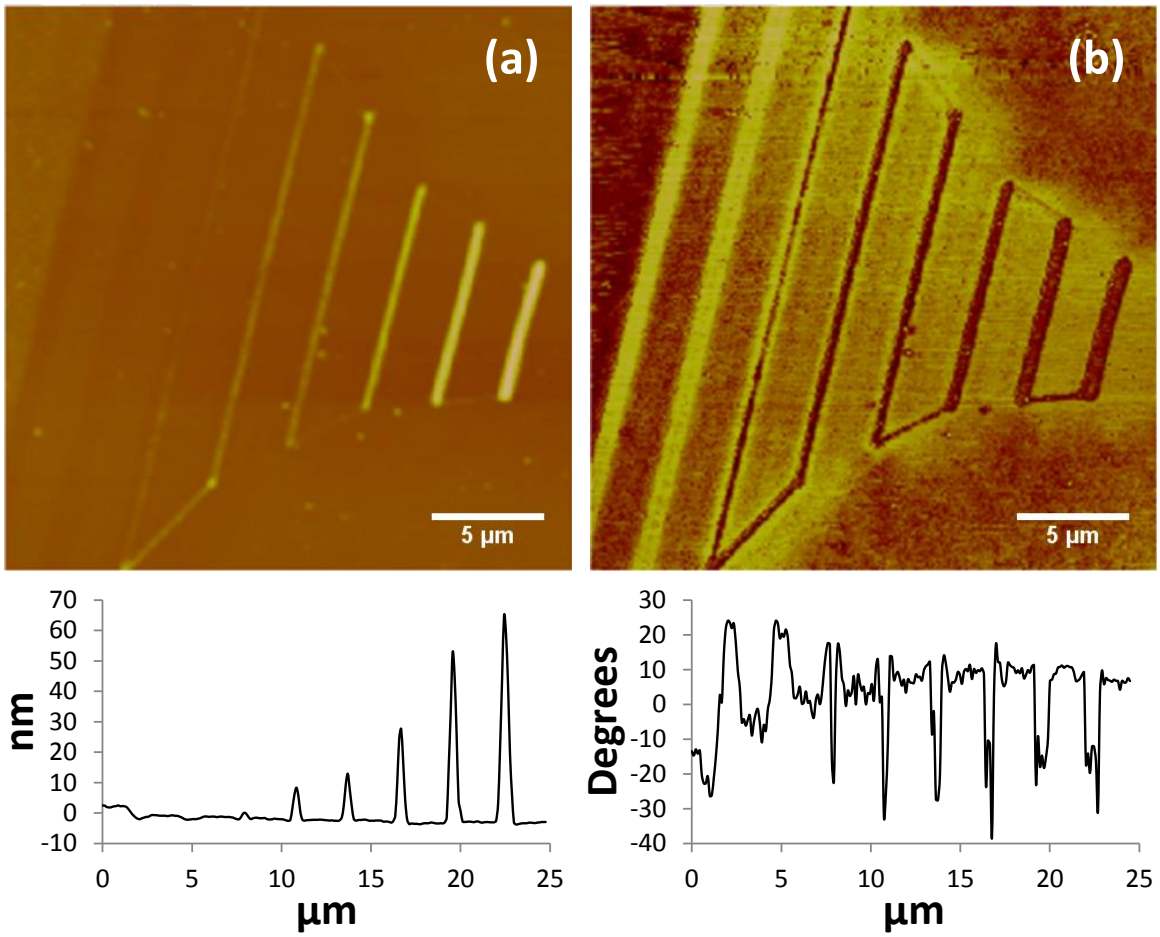

Figure 3.20: AFM tapping mode images and corresponding line-sections showing, (a) height and (b) phase contrasts of a set of 8 lines of polyOEGMA brush grown from lines drawn by SNP into an NPPOC-silane film with increasing scan speeds of 10, 20, 40, 60, 80, 100, 150 and 200 nm s^{-1} (going from right to left in the images)

Figure 3.21 shows the variation in the heights of the lines measured by AFM, and the percentage of photodeprotection of the NPPOC group (determined by water contact angle

measurements of samples exposed to 325 nm wavelengths, shown in Figure 3.4 (a)) as a function of exposure. The percentage of NPPOC removed approaches a limiting value at an exposure of 12.1 J cm^{-2}, indicating that all of the NPPOC is removed at this dose. For the AFM data, it was assumed that the highest features resulted from complete photodeprotection of the NPPOC-silane film, so they should be structurally identical with the features produces using macroscopic exposure at a dose of 12.1 J cm^{-2}. There is a remarkably good correlation between the two data sets, suggesting a linear relationship between the height of the polymer lines and the extent of deprotection. This is consistent with a systematic study that observed a linear relationship between initiator density and brush thickness[191].

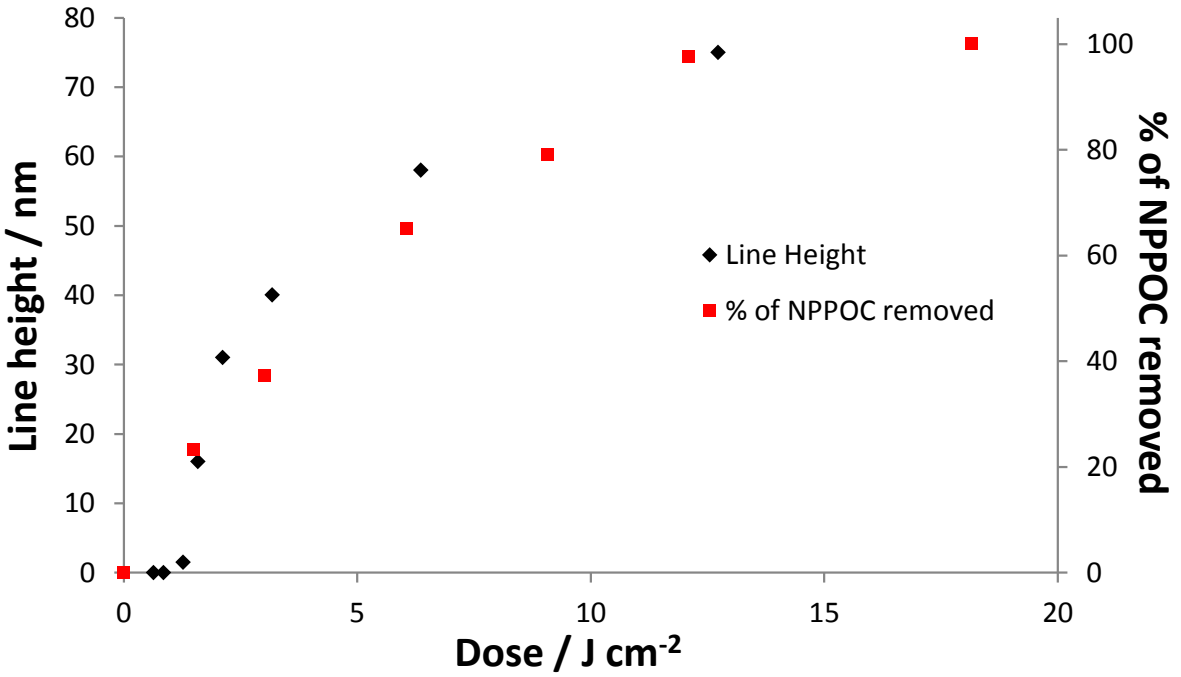

Figure 3.21: Graph of line heights measured by AFM plotted against exposure dose, for the sample of 8 lines scanned with varied speed (black diamonds); also showing the percentage of NPPOC removed (from water contact angle analysis, the percentage of NPPOC that has been removed was calculated by assuming at 0 J cm^{-2} 0% is removed and at 18.2 J cm^{-2} 100% is removed) plotted against exposure dose for an unpatterned sample.

Figure 3.22 (a) and (b) are AFM tapping mode images and corresponding line-sections of the array of 6 lines scanned a varying number of times with 100 nm separations. Since the exposed area of the scanning probe was 300 nm diameter, an offset of 100 nm would result in an overlap of 50 nm. This was done deliberately to ensure there was no gap between exposed

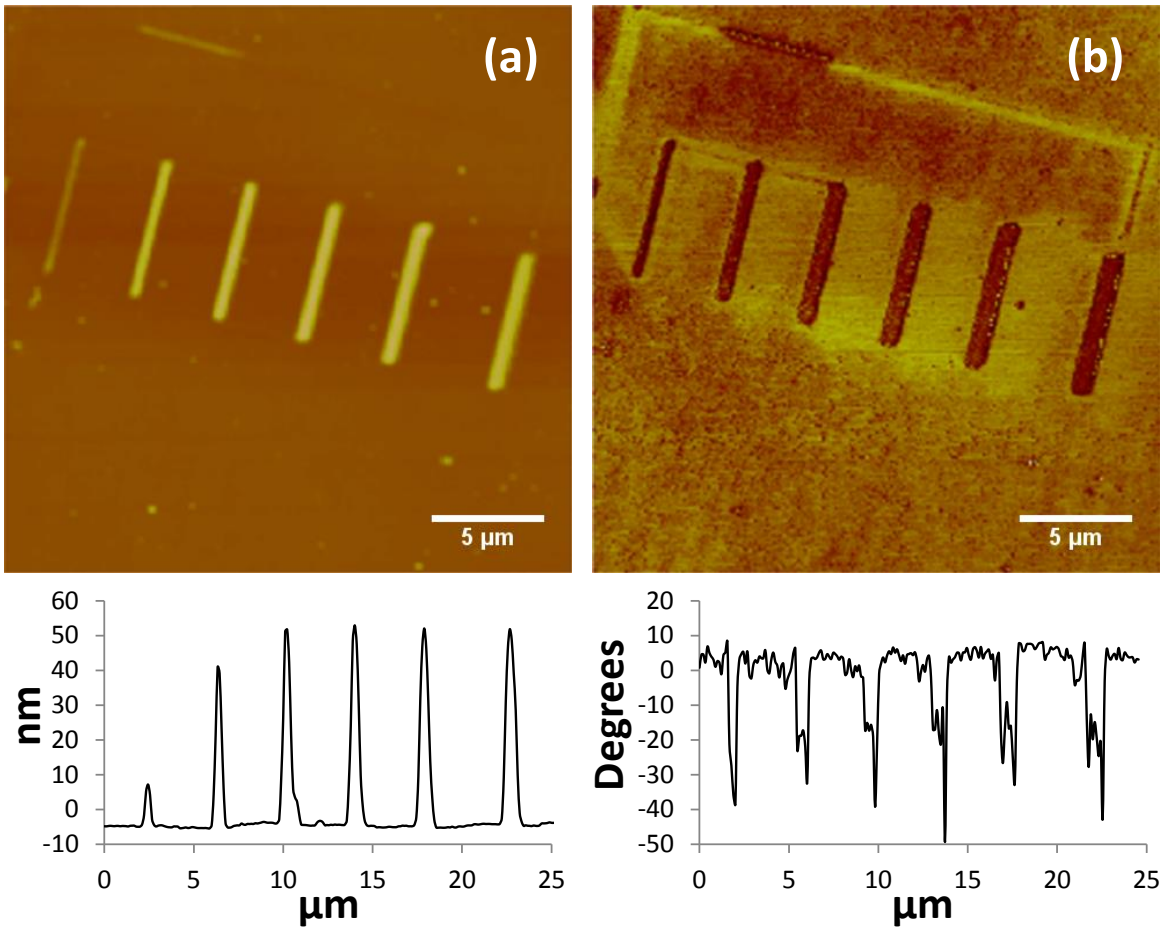

Figure 3.22: AFM tapping mode images and corresponding line-sections showing, (a) height and (b) phase contrasts of a set of 6 lines of polyOEGMA brush grown from lines drawn by SNP into an NPPOC-silane film with an increasing number of traces, each offset by 100 nm, from 1, 2, 3, 4, 5 and 6 lines (going from left to right).

regions of a set of multiple scans, resulting in lines with a continuous cross-section of grafting density. A scan speed of 60 nm s^{-1} was also maintained for all the scans. The purpose of this was to investigate whether the properties of the polymer structure changed with decreasing lateral resolution, with an aim to probe the transition between a bulk-structure of polymer and a nano-structure of polymer. From the line-section corresponding to Figure 3.22 (a), the line widths increase by approx. 100 nm for each addition trace, as expected. An increase in the height of the first three lines is observed and then remains fairly constant for the remaining three lines. However, this is most likely not caused by an increase in width and is a product of the overlapping exposures, as illustrated in Figure 3.23, which explains that for the first three lines an increase in exposure as well as width has also occurred, but for the following lines consisting of 3+ scans no more increase in exposure occurs, and hence no

significant height difference is measured. The similar heights, measured for the lines consisting of 3, 4, 5 and 6 scans, suggest that there is no effect of changing line width (within the range of 500 – 800 nm) with line height. It is likely that these length scales are an order of magnitude too large to observe a transition in the polymer structure. The same conclusion is drawn from the line-section of the phase contrast, corresponding to Figure 3.22 (b), where no significant change in phase is observed. The sharp spikes observed on the right edges of the peaks are caused by a sudden and significant change in height and should be disregarded.

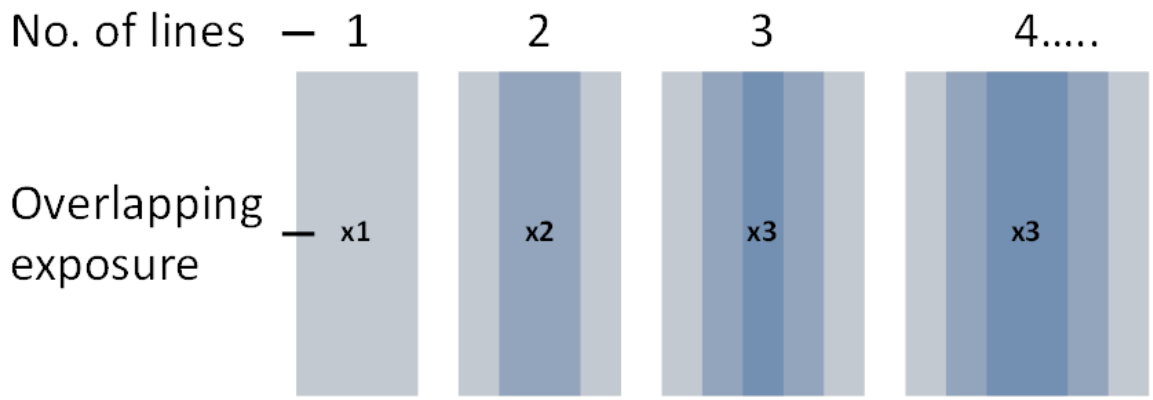

Figure 3.23: Schematic illustration of the effect of overlapping exposure when multiple lines are scanned with 100 nm separation.

3.4 Conclusion

Films of NPPOC-silane have been successfully formed. The photo-deprotection of the NPPOC group by irradiation with 325 nm and 244 nm wavelengths has been investigated. The results show an initial rapid loss of the NPPOC group when using 244 nm compared to using a wavelength of 325 nm. Irradiation with 244 nm also yields a more hydrophilic surface than observed with 325 nm exposures. Characterisation by XPS determined that complete removal of the NPPOC protecting group was achieved at 244 nm with a dose of 2.5 J cm^{-2}. XPS spectra also suggested that at high doses (> 2.5 J cm^{-2}), possible creation of polar species as well as photodegradation of the APS molecule could occur. Successful derivatisation of the deprotected surface with a radical initiator was determined by XPS. The subsequent growth of a polyOEGMA brush from the initiated surface in two different solvents was characterised by XPS, which determined that water gave the higher yield and rate of polymerisation and therefore was used in the subsequent patterning experiments.

Micro- and Nanoscale Fabrication of Non-Fouling Polymer Brushes by the Selective Deprotection of NPPOC-Silane Film

Micron patterns were produced by exposing the NPPOC-silane sample to 244 nm wavelengths through a TEM grid. PolyOEGMA brushes were selectively grown from the resulting grid patterns. Characterisation by AFM showed that the brushes grew from the exposed regions of the NPPOC-silane following an initiation step. IgG-FITC was adsorbed onto the micron patterned brush surface. The corresponding fluorescent micrographs showed that the polyOEGMA regions effectively inhibited the adsorption of the protein.

Two contrasting nano-photolithographic techniques were used to pattern a film of NPPOC-silane, from which polyOEGMA was grafted from the exposed areas by SI-ATRP. IL has demonstrated large area patterning of periodic features with lateral resolutions of 100 nm. Interference patterns were recoded into NPPOC-silane films and characterised by FFM. The frictional contrast between the exposed and unexposed lines was shown to increase with increasing exposure dose. PolyOEGMA was grown from both single and double exposures, in which the height contrast measured by AFM was shown to decrease with increasing exposure dose. This was thought to be mainly caused by a decrease in the separation between polymer lines, resulting in a smaller penetration depth of the AFM tip when probing between the lines. Overall, accurate characterisation of the polymer structures patterned by IL was not achievable because the proximity between the structures was too small. SNP has demonstrated serial patterning of non-periodic patterns with the ability to produce multifunctional patterns on the same surface. The lithographic technique was used to draw lines in an NPPOC-silane film, from which polyOEGMA was grafted from and characterised by AFM. A set of 8 lines with varied exposure doses, displayed a trend of decreasing exposure dose with decreasing line height, suggesting that the grafting density of the lines directly affected the dry thickness of the polymer. A set of 6 lines with varied widths showed no detectable change in the height or phase contrast between lines of 500 nm and 800 nm wide. A decrease in the line height was measured between lines 500 nm, 400 nm and 300 nm wide, but this was explained by an overlapping of the irradiated area rather than a consequence of the reducing line width.

Chapter Four

4 Using Nanoimprint Lithography to Indirectly form Functional Chemical Patterns on a Solid Surface for Protein Adsorption

4.1 Introduction

Fabricating patterns of SAMs using top-down and bottom-up approaches enables defined regions of a surface to be chemically patterned. These chemical patterns can allow for the controlled attachment and positioning of molecules or particles with a variety of functionalities on the surface. More specifically, these surface patterns can be used to control the immobilisation and organisation of biological molecules on a surface, which is becoming increasingly important for applications in biotechnology and medicine[203].

A variety of methods exist for patterning SAMs on solid surfaces such as photolithography[30-32], SPL[56, 67, 78, 80, 175], EBL[204] and μCP[83-85]. However, there are few techniques that offer the capability to pattern organic molecules on a surface with nanometre lateral resolution over a *macroscopic* area.

IL has been shown to be capable of patterning SAMs with sub-100 nm resolution over macroscopic areas. Turchanin *et al* used EUV-IL to produce lines of an alkylthiolate on gold, over an area of 0.2 cm^2, with a periods ranging from 2000 nm to 60 nm by photo-oxidation[205]. Tizazu et al used a simple Lloyd's mirror assembly to produce 60 nm diameter dots of an alkylphosphonic acid on titanium over an area of 0.5 cm^2 by photo-degradation[206]. However, the technique is limited to patterning systems in which the SAM can be either chemically altered or removed by exposure to a specific wavelength. It is also limited in its range of pattern geometry, as it can only fabricate periodic patterns.

DPN has the ability to pattern organic molecules on a surface with very high resolution, as low as 14 nm has been reported[57]. A variant known as massively parallel DPN, which incorporates 55000 tips moving in parallel across an area of 1 cm^2, has been reported to yield sub-100 nm dots of 1-octadecanethiol (ODT)[76]. Although DPN can offer high resolution patterning over macroscopic areas with negligible limitations of pattern geometry within 2D, it is confined to a finite group of 'ink' molecules that are compatible with the process. Additionally, the complexities of the massively parallel writing technique restrict its use.

NIL is a high-throughput, high-resolution technique that uses a hard mould, with pre-determined topographical features, to imprint a pattern into a polymer resist. Furthermore, the moulds are largely fabricated by EBL, so that a wide range of pattern geometries can be achieved. NIL does not pattern organic molecules on a surface directly. Instead, it forms a

topographical pattern in a polymer resist that can act as a template to direct the spatial arrangement of organic molecules on a surface as illustrated in Figure 4.1 and Figure 4.2.

The aim of the present chapter is to demonstrate the capabilities of NIL to fabricate chemically functional patterns of silanes on a SiO_2 surface. Films of PMMA will be imprinted and used as a template to produce a pattern of APTES and PEG-silane on a glass substrate. The resulting pattern will be exposed to a protein solution and its ability to control the proteins adsorption onto the surface will be analysed.

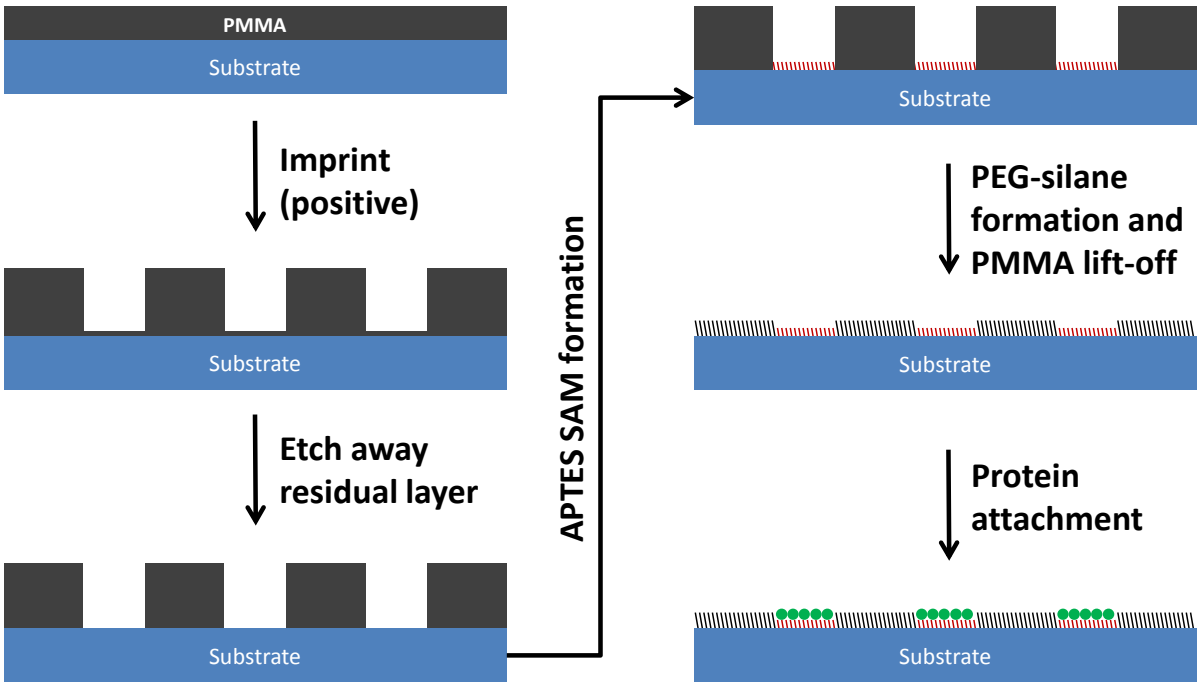

Figure 4.1: Schematic diagram showing the fabrication of patterns of silanes, for directed adsorption of proteins, using imprinting with positive moulds. After etching the residual layer, the remaining PMMA structures mask the substrate from an APTES coating. If using a positive mould, the trenches in the relief pattern will determine the regions of APTES and consequently the regions that will adsorb protein.

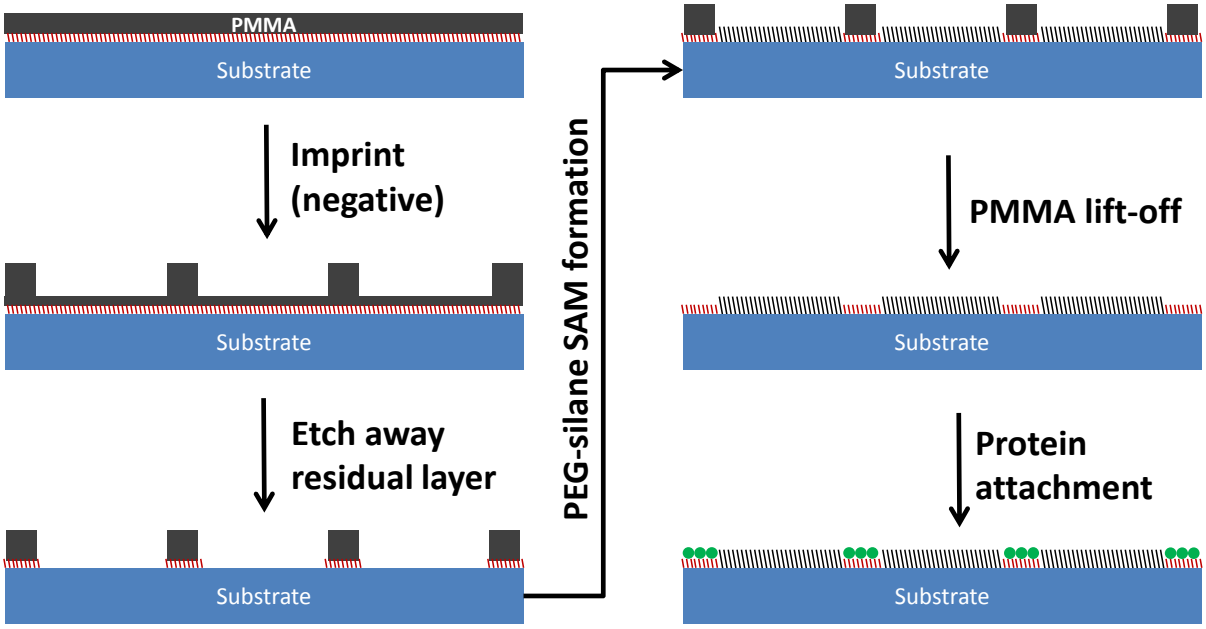

Figure 4.2: Schematic diagram showing the fabrication of patterns of silanes, for directed adsorption of proteins, using imprinting with negative moulds. Etching the residual layer also removes the film of APTES directly beneath. These regions of the substrate can then be coated with PEG-silane. If using a negative mould, the peaks of the relief pattern will determine the regions of APTES and consequently the regions of adsorbed protein.

4.2 Experimental

NIL Process

Silicon or glass substrates were cleaned with piranha and RCA solutions as described in section 2.3. A liquid PMMA precursor was then spin-coated on the surface of either an unmodified clean substrate or a substrate that had been functionalised with an APTES film. The PMMA precursors are supplied with pre-set viscosities so that spin coating at 3000 rpm for 30 s will produce the specified thickness on the surface.

The moulds were coated in an anti-adhesive layer before imprinting. To facilitate this, they were first cleaned by the same method implemented for the substrates. The clean and dry moulds were then placed into a vacuum desiccator along with an open vial containing 0.1 mL perfluorodecyltrichlorosilane (FDTS) and evacuated to a reduced pressure. The desiccator

was then sealed and left for 12 h to allow for a monolayer of FDTS to cover the entire surface of the mould.

Imprinting was carried out with an Obducat Eitre 6 imprint system, at a temperature of 150 ºC and a pressure of 50 bar, for a minimum of 300 s.

RIE

Sample Description (imprinted pattern / PMMA spin-coat thickness)	**RIE**		
	RF Power / W	**O_2 pressure / Torr**	**Time / s**
2 μm grating / 2 μm	250	110	60-120
2 μm grating / 1 μm	100	60	30
1 μm diameter holes / 0.3 μm	100	60	30
10 μm diameter holes / 1 μm	100	60	30
2 μm diameter pillars / 1 μm	90	60	600
0.5 μm diameter pillars / 0.3 μm	90	60	120
70 nm diameter pillars / 100 nm	40	40	80-100

Table 4.1: Parameters for RIE, used for the removal of the residual layer of different imprints.

Removal of the residual layer was carried out using RIE (Oxford Plasma Lab 80 plus) as described in section 2.9. The RIE parameters used for the different imprints are given in Table 4.1. The RIE parameter values were calculated based on prior knowledge within the group regarding dry etching of polymer materials.

Silane SAM Formation

APTES films were formed by submersing the substrate into a 1% aqueous solution for 30 min as described in section 2.4.

PEG-silane films were formed inside a glovebox with controlled moisture and oxygen levels. Samples were submerged into a dry toluene solution containing 1 mM PEG-silane, for 2 h, as described in section 2.4.

Protein Adsorption

Proteins were adsorbed onto either unmodified patterns of APTES or biotinylated patterns of APTES.

Biotinylation of the surface bound APTES molecules was carried out using a water soluble carbodiimide coupling agent, 1-ethyl-3-(3-dimethylaminopropyl)carbodiimide (EDC). Samples were submerged into an aqueous solution containing 10 mM of biotin and 10 mM EDC for 2 h. The samples were then rinsed with DI water and dried under a stream of nitrogen.

Wheat germ agglutinin-fluorescein (WGA-fluorescein) or streptavidin-Cy3 proteins were adsorbed onto the samples according to procedures described in section 2.7, for up to 24 h.

NIL Mould Distinction

Moulds were classified as either ‘positive’ or ‘negative’. The difference was defined by the percentage of raised areas being low for a positive mould and high for a negative mould. Moulds in which the percentage of raised areas was close or equal to 50% could be treated as either.

In order to produce the minimal feature sizes for protein patterning, two different fabrication routes were implemented depending on the type of mould (positive or negative) used. Figure 4.1 illustrates the process route carried out using positive moulds, whereas Figure 4.2 illustrates the process route carried out using negative moulds.

4.3 Results and Discussion

Initial imprints were carried out using a 2 μm grating mould and 2 μm thick PMMA spin-coated on silicon wafer. It was important to use a relatively simple mould, such as a 2 μm grating, to ensure the preliminary investigations into the imprint process and subsequent etching steps to remove the residual layer were consistent and straightforward. Figure 4.3 (a) is an SEM image taken of the cross-section through a 2 μm thick layer of PMMA after imprinting with a 2 μm grating mould. The image shows that the PMMA has been displaced by the mould as expected, producing a topographical replica. The interface between the silicon substrate and PMMA can be seen in the image as a pale line separating the two slightly different shades of grey. The residual layer is measured as the distance from the bottom edge of a trough in the imprint pattern to the interface between the PMMA and silicon substrate. In this case the residual layer was measured to be 1 μm, which was anticipated since the empty cross-sectional volume of the 2 μm grating is 1 μm^2, thus it will only consume the first 1 μm of the 2 μm thick PMMA during imprinting.

In order to functionalised regions of the surface with SAMs the residual layer must be completely removed to reveal the underlying native oxide of the substrate. Furthermore, the etching process should be anisotropic (in the vertical plane) to ensure the residual layer can be removed without completely etching away the imprinted structures. Therefore, RIE was used in all circumstances for the removal of the residual layer, because of its anisotropic qualities. During the RIE etching process two different mechanisms of etching take place, physical ablation of surface material by the bombardment of ions, and the chemical breakdown of surface material by the accumulation of reactive species on the surface. The former is highly anisotropic while the latter is highly isotropic. Changing the gas pressure and RF power determines which mechanism (physical or chemical) dominates during the RIE process. It was decided that an etch that is mostly physical in nature but also exhibited some chemical nature was required. The physical component was required to produce a highly anisotropic etch in order to retain the lateral dimensions of the imprinted structures. However, the chemical component was required to adequately remove small particles within the regions of the exposed substrate, yielding a clean surface prior to SAM formation. Figure 4.3 (b – d) are SEM images of the cross-sections taken after the imprinted samples had received etching times of 1, 2 and 3 min respectively, with an RF power of 250 W and gas pressure of 110 torr. After a 1 min etch time, it is observed that the thickness of the PMMA has reduced by

approx. 1 μm, resulting in the removal of almost the entire residual layer, with only a small reduction in the widths of the structures. After a 2 min etch time, the thickness of the PMMA has reduced by approx. 2 μm, resulting in the complete removal of the residual layer. However, the widths of the PMMA structures are reduced more significantly, consequently a greater area of substrate is exposed than initially determined by the dimensions of the imprinting mould. After a 3 min etch time, almost all of the PMMA has been removed from the surface and it is probable that the sample has been over-etched. From these images it can be seen that the RIE reaction conditions that were used etch the PMMA vertically at a rate of approx. 17.0 nm s^{-1} and horizontally at a rate of approx. 7.0 nm s^{-1}, illustrating to some extent the proportions of the physical and chemical components of the etch.

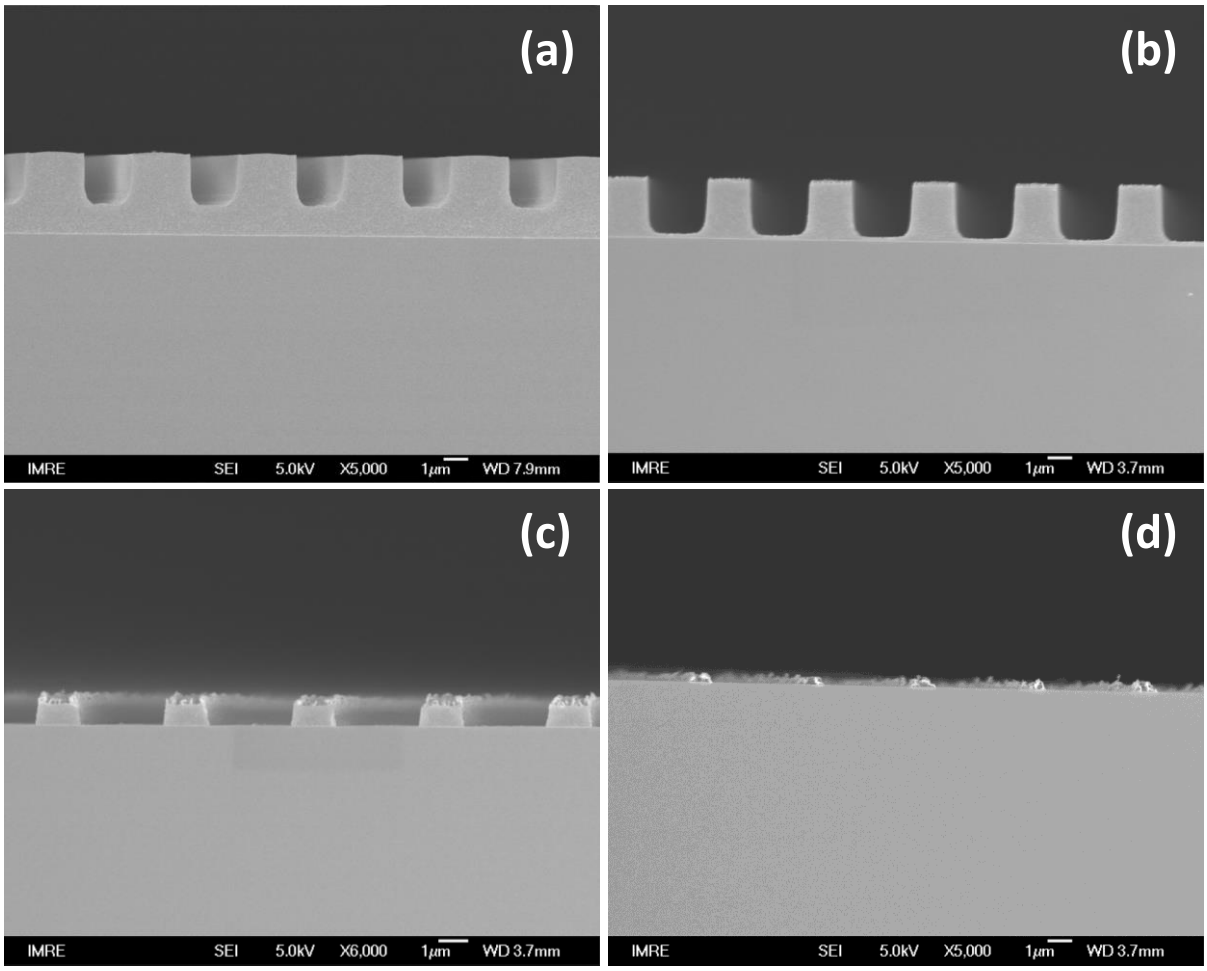

Figure 4.3: SEM cross-section images of a 2 μm thick layer of PMMA imprinted with a 2 μm grating mould after receiving an anisotropic etch with O_2 gas, for (a) 0 min, (b) 1 min, (c) 2 min and (d) 3 min.

Imprinting with Positive Moulds

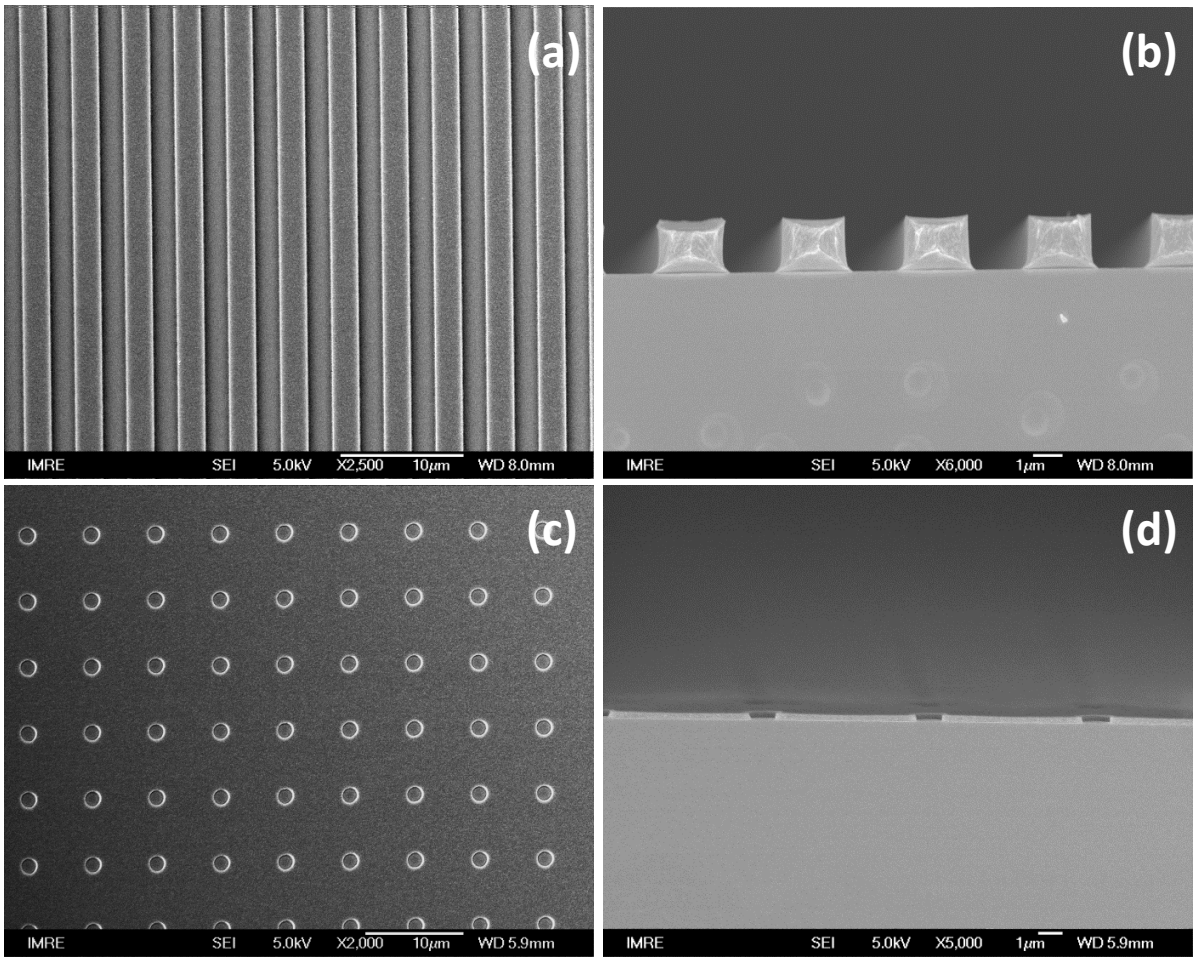

Figure 4.4: SEM images showing 2 different mould imprints. A 2 μm grating, imprinted into a 1 μm thick layer of PMMA, showing (a) the top view and (b) the cross-section. An array of holes 1 μm diameter , imprinted into a 0.5 μm thick layer of PMMA, showing (c) the top view and (d) the cross-section.

When using positive moulds it is undesirable to produce larger exposed regions of substrate by over etching the sample after the complete removal of the residual layer. This is because the size of the exposed areas will determine the size of the APTES regions within the pattern, which in turn will determine the size of the regions of adsorbed proteins. Therefore, to limit the degree of lateral expansion, imprints with minimal residual layer were produced to reduce the etching times. Figure 4.4 (a, b) are SEM images of a 1 μm thick layer of PMMA after imprinting with a 2 μm grating mould. Figure 4.4 (c, d) are SEM images of a 0.5 μm thick layer of PMMA after imprinting with a 1 μm diameter pillar mould. The cross-sections are shown in images (b) and (d), in which a residual layer less than 100 nm thick is observed.

With a much thinner residual layer compared to the imprint shown in Figure 4.3 (a), a much shorter etching time was going to be required. Using the previously calculated vertical etch rate of 17 nm s^{-1}, it would take 6 s to etch 100 nm. It was evaluated that 6 s was too short a time to give a controlled and consistent etch. Therefore, the RF power and gas pressure were reduced to 100 W and 60 torr respectively to slow the etching rate, resulting in a more controlled etch. SEM cross-section images of the 2 μm imprint before and after etching for 30 s are shown in Figure 4.5 (a) and (b) respectively. Because the residual layer is so thin, it is hard to detect it in Figure 4.5 (a). However, when image (a) and (b) are compared, the sloped edges present in the trough of the imprint in image (a) can no longer be observed in image (b), suggesting that any thin layer of PMMA between the structures has also been removed.

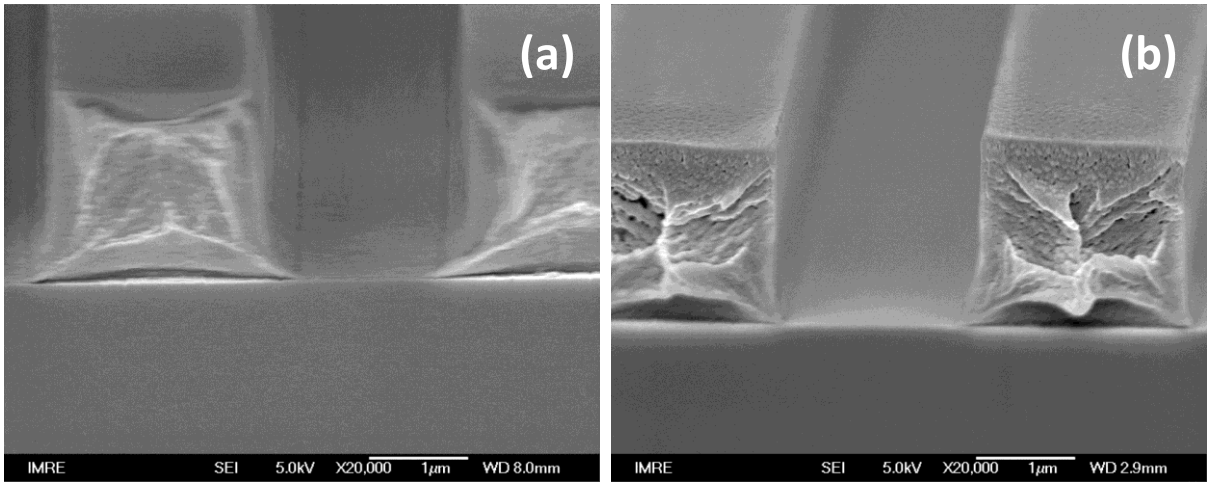

Figure 4.5: SEM images showing the cross-section of a 2 μm grating imprint, taken at a tilted angle relative to the plane (a) before etching and (b) after etching.

Following the removal of the residual layer, the exposed areas of the underlying substrate can be functionalised with a silane SAM. The PMMA structures remaining on the surface will mask their underlying substrate areas from any silane deposition. However, because PMMA can dissolve in most organic solvents, methods for SAM formation were limited to either using an aqueous medium or vapour deposition. For the deposition of APTES, it was established that the best results came when an aqueous medium was used. Once the APTES monolayer was formed on the exposed regions of the surface, the remaining PMMA structures were removed completely, using toluene at elevated temperatures. The newly revealed areas of substrate could then be derivatised with PEG-silane. Because of the

contrasting nature of APTES and PEG-silane towards proteins, the fabricated pattern can be used to direct the adsorption of proteins onto the APTES regions of the surface.

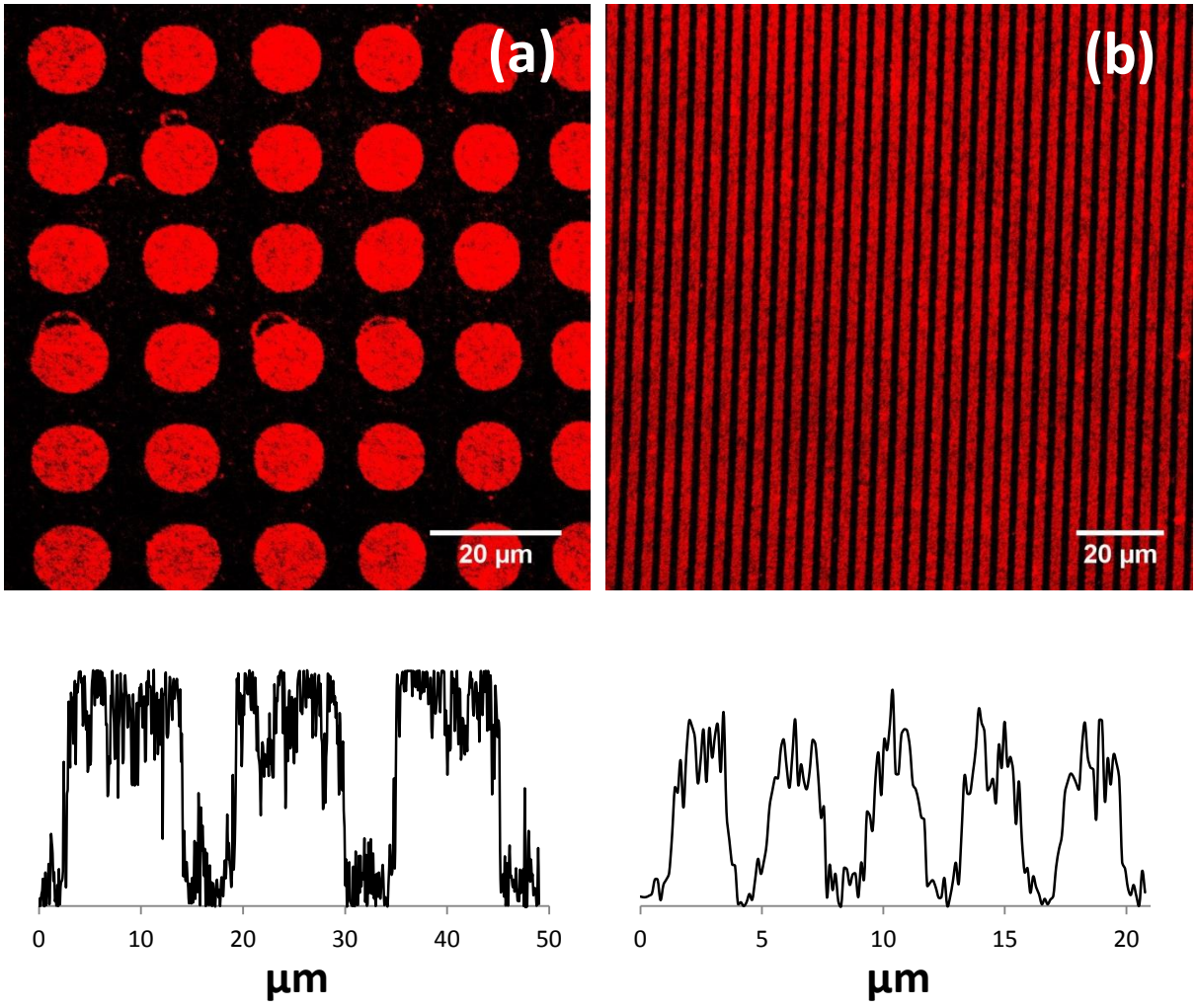

Figure 4.6: Fluorescent micrographs of streptavidin-Cy3 adsorbed onto regions of APTES surrounded by PEG-silane on (a) an array of 10 µm diameter dots and (b) an array of 2 µm lines. The corresponding intensity profiles are shown below each micrograph.

The ability of these surface patterns to immobilise proteins and the degree of control over the protein spatial organisation was characterised by scanning laser confocal microscopy. Figure 4.6 (a) is a fluorescent micrograph and corresponding intensity profile taken of a sample consisting of streptavidin-Cy3 adsorbed onto an array pattern of 10 µm diameter dots of APTES, surrounded by an expanse of PEG-silane. From the image, it is clear that, to a large extent, the protein has adsorbed onto the APTES dots while resisting attachment to the PEG-

silane functionalised regions of the surface. The intensity profile relays a similar situation, displaying high intensity signals from the dots which are separated by regions of low level fluorescence. From the micrograph, loop shaped bands of fluorescence are visible close to a few of the dots, which appear to be significant instances of non-specific adsorption of the protein. However, these are artefacts of the original imprint of PMMA, caused by trapped gas that produces cavities in the PMMA, exposing regions of the surface that get derivatised with APTES and consequently coated with protein. Some small bright points are observed on regions of PEG-silane. Because films of PEG-silane are well-known for their strong anti-fouling capability, the high intensity anomalies are likely caused by an incomplete PMMA lift-off, resulting in traces of PMMA masking the surface from the absorption of PEG-silane molecules. The low intensity anomalies observed within 10 μm diameter dots could simply be caused by an incomplete monolayer of protein being adsorbed. Alternatively, low intensity anomalies could have been caused by traces of contaminates or PMMA residue left on the exposed substrate surface after etching away the residual layer. These contaminants would then mask the underlying substrate from absorption of the APTES molecules, but could then be removed in hot toluene during the PMMA lift-off process, revealing bare regions of substrate that would be derivatised with PEG-silane and consequently resist protein adsorption. The flaws observed in Figure 4.6 (a), highlight the failings associated with a multi-step method such as the one used, in which faults and defects can be carried from one step to the next. Figure 4.6 (b) is a fluorescent micrograph and corresponding intensity profile taken of a sample consisting of streptavidin-Cy3 adsorbed onto a pattern of 2 μm lines of APTES separated by 2 μm lines of PEG-silane. The image clearly shows a pattern of fluorescent lines (red) approx. 2 μm in width, separated by 2 μm lines of low fluorescence (black). However, because the lines have the same width it can only be assumed that the red lines correspond to the APTES functionalised regions of the surface and the black lines correspond to the PEG-silane functionalised regions of the surface, consistent with the widely recognised characteristics of PEGylated molecules to resist protein adsorption. The intensity profile shows strong fluorescence across the APTES lines as expected. However, it also shows a low level of fluorescence across the PEG-silane lines. This is likely to be caused by reasons previously described for Figure 4.6 (a).

Imprinting with Negative Moulds

For reasons previously described, it is undesirable to produce large regions of APTES on the surface. It is more desirable to fabricate patterns that bind protein in small discrete regions on the surface. Therefore, when imprinting using negative moulds, the imprinted structures of PMMA should determine the regions of APTES on the surface as opposed to PEG-silane. This could not be achieved by following the same experimental procedure as used for positive moulds and simply changing the order in which the different silanes were absorbed onto the surface, because a film of PEG-silane could not be formed on the surface using either an aqueous medium or by vapour deposition. A novel solution was to absorb a film of APTES onto the substrate prior to spin-coating a layer of PMMA. After imprinting and removal of the residual layer, the exposed regions of the surface can be derivatised with PEG-silane. Subsequent removal of the remaining PMMA structures yields a chemical pattern of APTES and PEG-silane. Figure 4.7 (a – c) are SEM images of a 1 μm thick layer of PMMA spin-coated over an APTES monolayer, after imprinting with a 2 μm diameter hole, 12 μm period mould. No significant defects are observed in any of the images (a – c), suggesting that the APTES functionalised surface has not adversely affected the quality of the spin-coated PMMA or the imprinting process. Image (a) shows a top view of the imprint pattern, while image (b) shows a cross-section. From image (b), the height of the pillars was measured to be approx. 4 μm. Image (c) shows a high magnification cross-section view, from which the residual layer thickness was estimated to be between 100 – 200 nm. The relatively large height of the pillars in conjunction with the thin residual layer granted a large margin for error for the removal of the residual layer. It also allowed that the samples could be continually etched beyond the removal of the residual layer, resulting in the decrease of the diameter of the pillars, which ultimately reduces the size of the final protein dots. The size of the PMMA structures (ca. 2 μm diameter) permitted the removal of the residual layer to be characterised using a standard optical microscope. A visible colour change can be observed between the bare substrate and even an ultra-thin layer of PMMA. It was observed that the residual layer had been removed after an etching time of 5 min. However, the etching process was extended by a further 5 min.

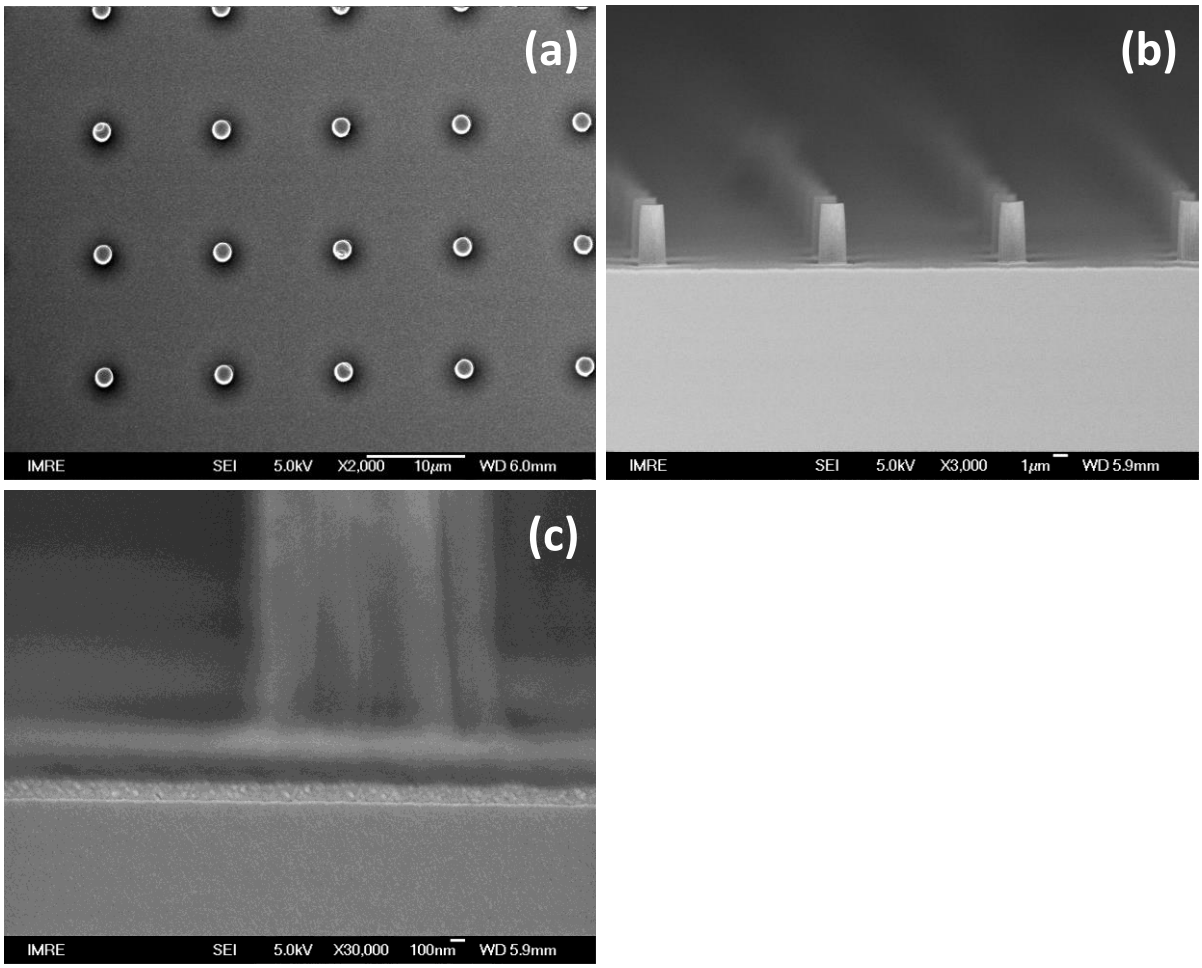

Figure 4.7: SEM images of an array of 2 μm diameter pillars imprinted into a 1 μm thick layer of PMMA, using a negative mould, showing (a) the top view, (b) the cross-section and (c) a high magnification of the cross-section measuring the residual layer to be approx. 150 nm thick.

After etching away the residual layer, a monolayer of PEG-silane was formed across the exposed regions of the surface and the remaining PMMA structures could be completely removed with toluene at elevated temperatures. Figure 4.8 (a, b) are AFM images and corresponding line sections (below) of a sample patterned with a 2 μm diameter hole mould. The dots in both images correspond to regions of APTES, the diameters of which should have been defined by the imprinted PMMA pillars of 2 μm diameter. However, the diameters of the dots have been reduced in size to approx. 1.5 μm, a consequence of the extended etching time.

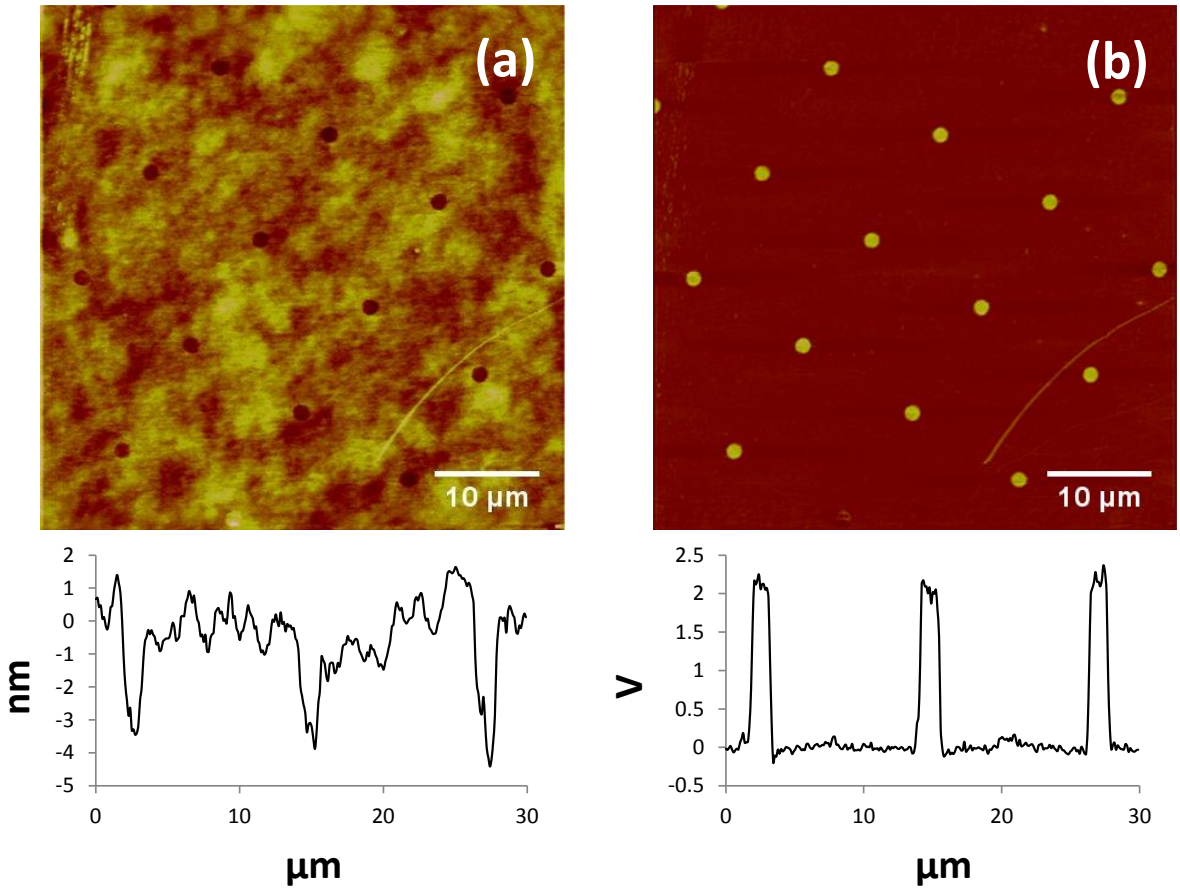

Figure 4.8: AFM (a) tapping mode height image and (b) contact mode subtracted (trace – retrace) friction image, measured from a surface patterned with 1.5 µm diameter dots of APTES surrounded by PEG-silane. Patterns were fabricated from a 1 µm thick layer of PMMA, imprinted by a 2 µm diameter hole mould. The corresponding line-sections are shown below each image.

The surface surrounding the dots corresponds to PEG-silane. Figure 4.8 (a) is a contact mode height image which clearly shows the dot shaped regions of APTES to be of a darker contrast, corresponding to a lower height, which is consistent with the shorter chain length of the APTES compared to the PEG-silane molecule. The line section (below image) shows the height difference to be in the region of 4 nm, which larger than the expected value of < 1 nm. This is possibly because of an increase in the thickness of the underlying native oxide of the substrate, caused by the bombardment of the surface by oxygen ions during the etching process. It could also be because of a multilayer formation of the PEG-silane rather than a monolayer. Figure 4.8 (b) is a subtracted (trace – retrace) friction image, which clearly shows a difference in contrast between the bulk surface and dots, suggesting a difference in surface

free energy between the two regions. The line section (below image) shows that the magnitude of the friction difference (approx. 2 V), is much larger than expected considering the relatively similar water contact angles (both between 40º – 50º) of the two surfaces. A possible explanation for the surprisingly large friction difference is a roughening of the surface of the substrate over the areas exposed by etching. During the RIE process, oxygen ions bombard the surface, which can lead to physical ablation of the surface, resulting in a much rougher surface. When comparing the interaction of the AFM tip with the APTES and PEG-silane surfaces, it will experience more frictional force, regardless of the molecular chemistry, from the flat APTES dots compared to the surrounding rougher PEG-silane surface, because it will contact much more of the flat surface.

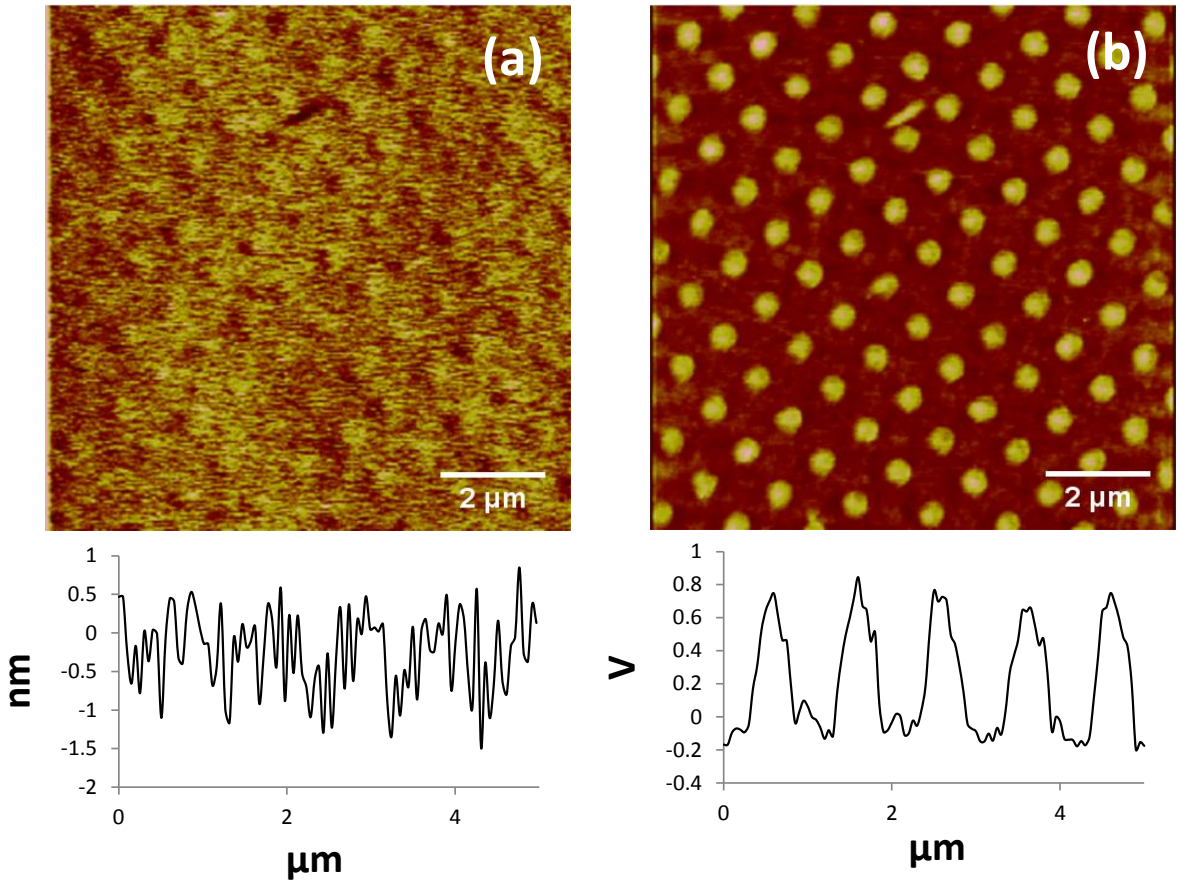

Figure 4.9: AFM (a) tapping mode height image and (b) contact mode subtracted (trace – retrace) friction image, measured from a surface patterned with 0.5 µm diameter dots of APTES surrounded by PEG-silane. Patterns were fabricated from a 0.3 µm thick layer of PMMA, imprinted by a 0.5 µm diameter hole mould. The corresponding line-sections are shown below each image.

A smaller and denser array pattern of APTES dots surrounded by PEG-silane was also fabricated, using a 0.5 μm diameter hole, 0.5 μm period mould to imprint a 0.3 μm thick layer of PMMA. The patterned silane surface was characterised by AFM and the images and corresponding line sections are shown in Figure 4.9. Figure 4.9 (a) is a contact mode height image, from which it is difficult to detect the array pattern in the contrast of the image. The corresponding line section does, however, show a faint repeating pattern of sections approx. 0.5 μm apart with a height difference of roughly 0.5 nm. The height difference measure is consistent with the expected value of < 1 nm. This is in contrast to what was observed for the 1.5 μm diameter dot pattern (Figure 4.8 (a)), in which a much larger height difference of 4 nm was measured. This is likely because the 0.5 μm diameter dot pattern was only etched long enough to remove the residual layer, whereas the 1.5 μm diameter dot pattern was etched for an extended time to achieve a reduction in the pillar diameters. This follows the previous hypothesis that the relatively large height difference measured for the 1.5 μm diameter dot pattern (4 nm) was caused by a growth of the native oxide on the areas of surface surrounding the APTES dots. Figure 4.9 (b) is a subtracted (trace – retrace) friction image, which clearly shows a difference in contrast between the bulk surface and the array of dots. A line section through the pattern measures the difference in friction force to be approx. 0.8 V. Comparing this data with the friction data for the 1.5 μm diameter dot pattern (Figure 4.8 (b)), a smaller difference in friction force is measured on the 0.5 μm diameter dot pattern, which can be explained by the extended etching time for the 1.5 μm diameter dot pattern causing a larger degree of surface roughening relative to the 0.5 μm diameter dot pattern. However the difference measures for the 0.5 μm diameter dot pattern is still larger than expected, which is possibly a result of some degree of surface roughening caused by the etching process.

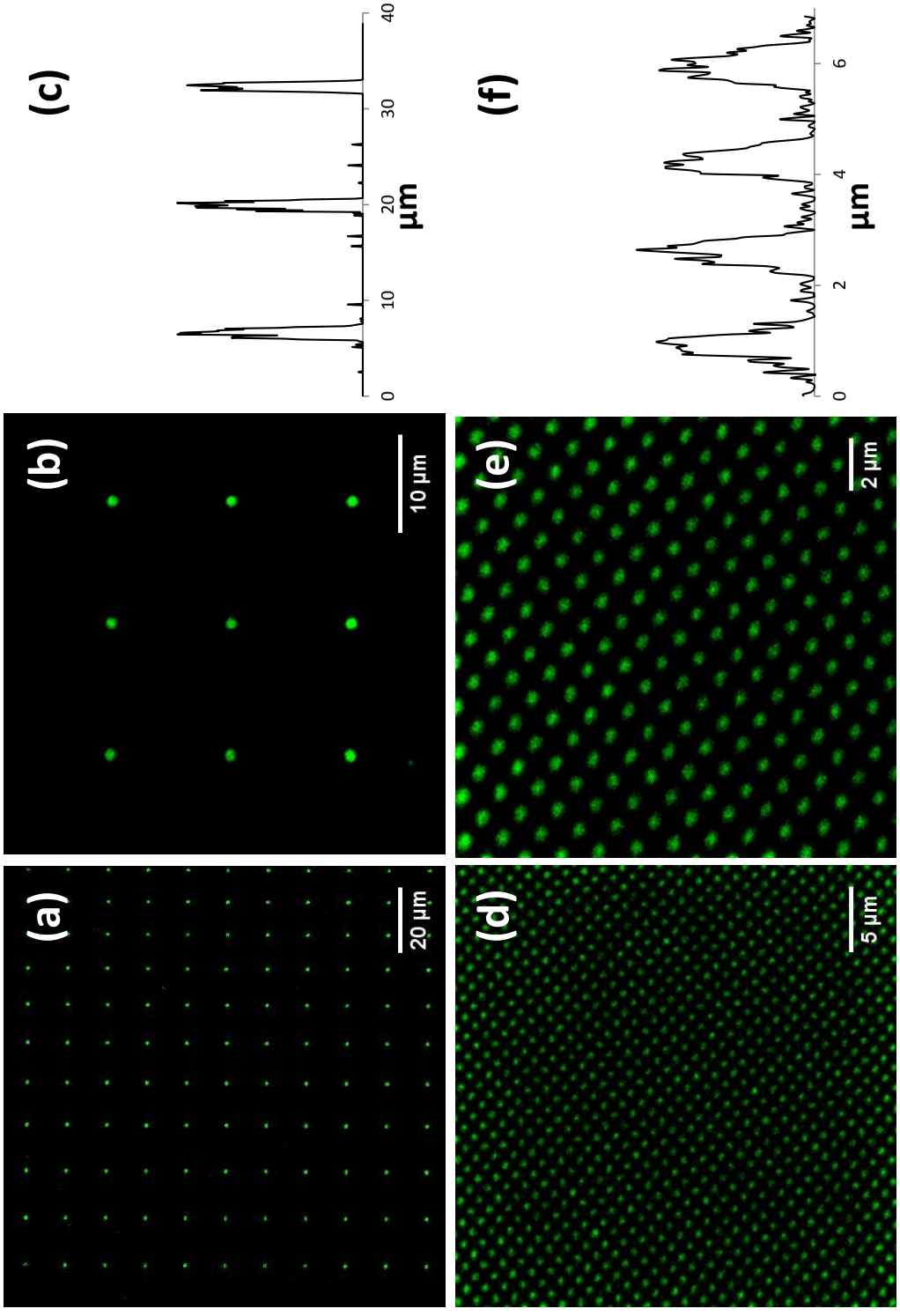

Figure 4.10: Fluorescent micrographs and intensity profiles of WGA-fluorescein adsorbed onto 1.5 µm diameter (a - c) and 0.5 µm diameter (d - f) dots of APTES. Intensity profiles (c) and (f) were taken from the higher magnification images (b) and (e) respectively.

The ability of these surface patterns to immobilise proteins and the degree of control over the proteins spatial organisation was characterised by scanning laser confocal microscopy. Samples of both 1.5 μm diameter and 0.5 μm diameter dot patterns were submerged into a solution containing WGA-fluorescein and the corresponding fluorescence micrographs and intensity profiles are shown in Figure 4.10. Figure 4.10 (a – c) are data acquired from a 1.5 μm diameter dot pattern and Figure 4.10 (d – f) are data acquired from a 0.5 μm diameter dot pattern. Fluorescence micrographs (a) and (d) were taken at relatively low magnification and illustrate the consistent uniformity in the fluorescence patterns over areas of 134 μm^2 and 33 μm^2 respectively. Fluorescent micrographs (b) and (e) were taken at relatively higher magnification and the intensity profiles (c) and (f) were measured from them. The intensity profile (c) shows that the 1.5 μm diameter dots exhibit a strong fluorescent signal with little or no signal detected between them. Similarly, intensity profile (f) shows that the 0.5 μm diameter dots exhibit a strong fluorescent signal, with a very low level of intensity detected between them. This suggests that the fabricated patterns have effectively bound the WGA-fluorescein with a very high degree of control over its spatial organisation on the surface.

Thus far the fabricated patterns of APTES and PEG-silane have successfully demonstrated the exceptional ability to direct protein adsorption onto regions of APTES functionalised surface. However, the justification for using APTES was not to promote protein adhesion, but was to allow for additional functionalities to be applied to the patterned dots by substitution reactions with the primary amine located at the tail end of the APTES molecule. Often when a protein adsorbs to a solid surface the interaction is erratic and reversible. Furthermore, the protein can undergo multiple configuration changes and lose its biological function. Molecules that specifically bind a protein can be used to immobilise that protein on the surface with retention of its biological function. Moreover, molecules that have a high binding affinity to a protein can be used to hold the protein to the surface making the surface-protein bond more robust and resistant to changes in conditions.

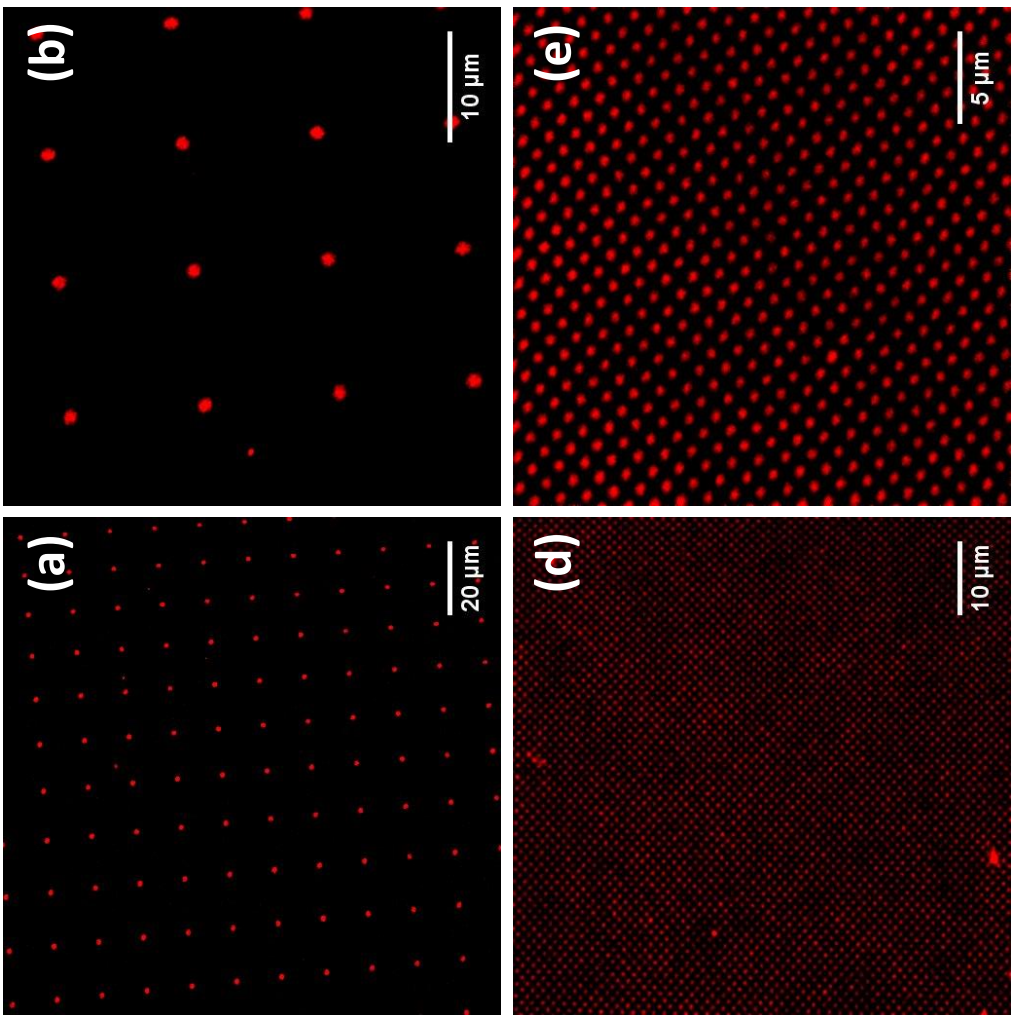

Figure 4.11: Fluorescent images and intensity profiles of streptavidin-Cy3 bound to 1.5 µm diameter (a - c) and 0.5 µm diameter (d - f) dots of biotin functionalised APTES. Intensity profiles (c) and (f) were taken from the higher magnification images (b) and (e) respectively.

A well-known molecule-protein interaction is the very strong affinity which exists between a molecule of biotin and a streptavidin protein. The patterned regions of APTES were firstly derivatised with biotin molecules and then submerged into a solution containing streptavidin-Cy3, the surface was then characterised by scanning laser confocal microscopy. The resulting fluorescent micrographs and intensity profiles for both the 1.5 μm diameter and 0.5 μm diameter dot patterns are shown in Figure 4.11. As expected the fluorescent micrographs of the different patterns show an array of fluorescing dots consistent with the configuration and dimensions of the surface APTES and PEG-silane measured by AFM, suggesting that the protein has effectively adsorbed to the regions of APTES derivatised with biotin, while resisting adsorption to the PEG-silane regions. A direct comparison with the data shown in Figure 4.10 cannot be made because a different protein and a different dye were used. 1.5 μm diameter dot patterns, that had not undergone biotinylation, were also immersed in a streptavidin-Cy3 solution. The fluorescent micrographs of streptavidin-Cy3 adsorbed onto spots of biotinylated APTES and unmodified APTES are shown in Figure 4.12 (a) and (b) respectively. No significant differences can be seen between the two micrographs. However, a difference in intensity can be seen between the intensity profiles of the biotinylated and non-biotinylated surfaces, which are shown in Figure 4.12 (c) and (d) respectively. Each graph is an overlay of four intensity profiles measures from separate micrographs. A dotted line has been drawn through what has been estimated as the average peak height of both the graphs. From the dotted lines it is clear that the average intensities of the protein dots are higher for the biotinylated sample compared to the non-biotinylated sample. The low level of fluorescence signal detected between the patterned dots appears constant in all the intensity profiles, suggesting that the increase in peak height observed for the biotinylated sample is not caused by changes in the characterisation method, but is likely to be caused by a higher binding affinity of the streptavidin-Cy3 towards the biotinylated dots compared to the unmodified APTES dots.

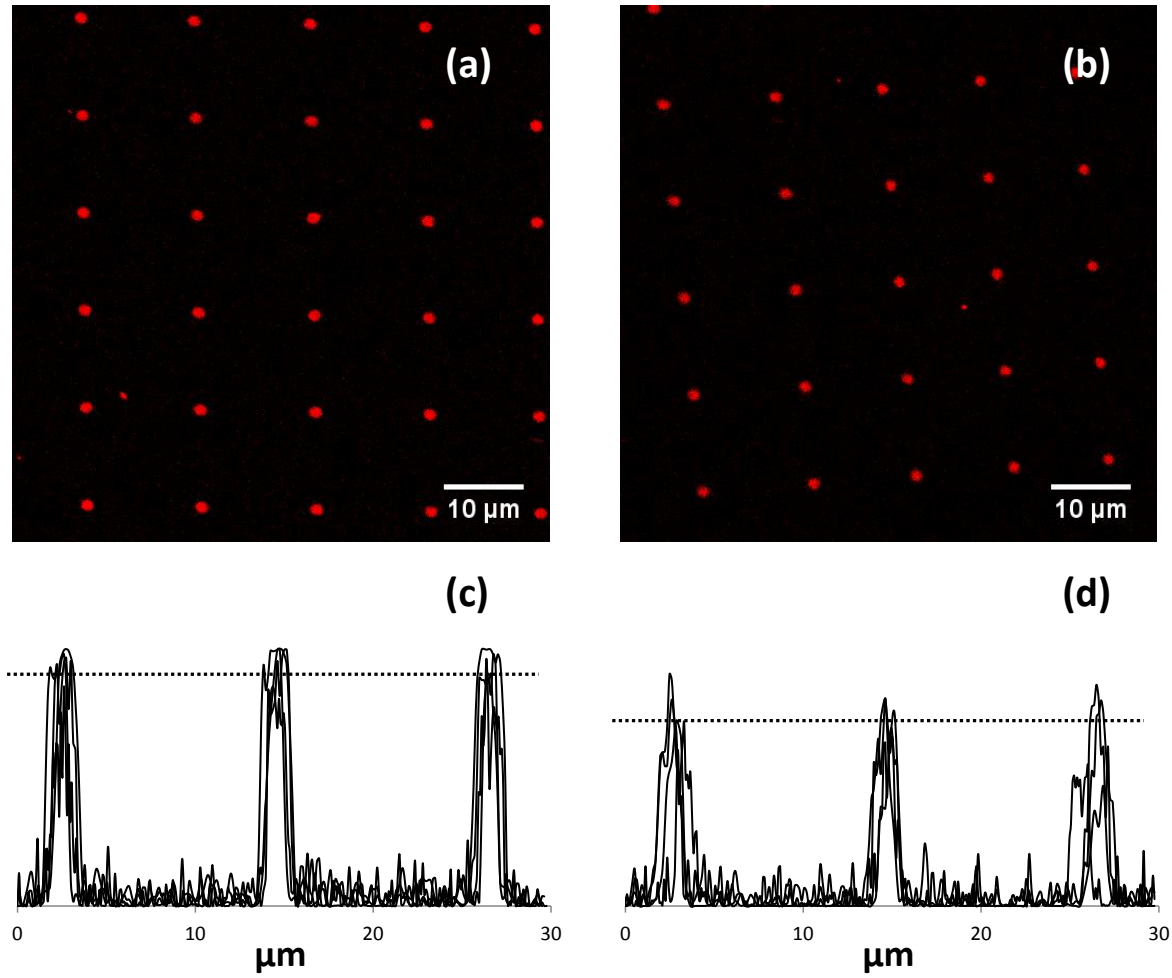

Figure 4.12: ***Top:*** *Fluorescent micrographs of a 1.5 µm diameter APTES dot patterned sample (a) with biotinylation and (b) without biotinylation, prior to adsorption of streptavidin-Cy3.* ***Bottom:*** *Four overlaid intensity profiles each measured from different fluorescent micrographs of 1.5 µm diameter dot pattern samples (a) with biotinylation and (b) without biotinylation, prior to adsorption of streptavidin-Cy3. A dotted line has been drawn through what was estimated to be the average heights of the intensity peaks, in both profiles, to make a comparison in intensities clearer.*

Nano-Scale Patterns

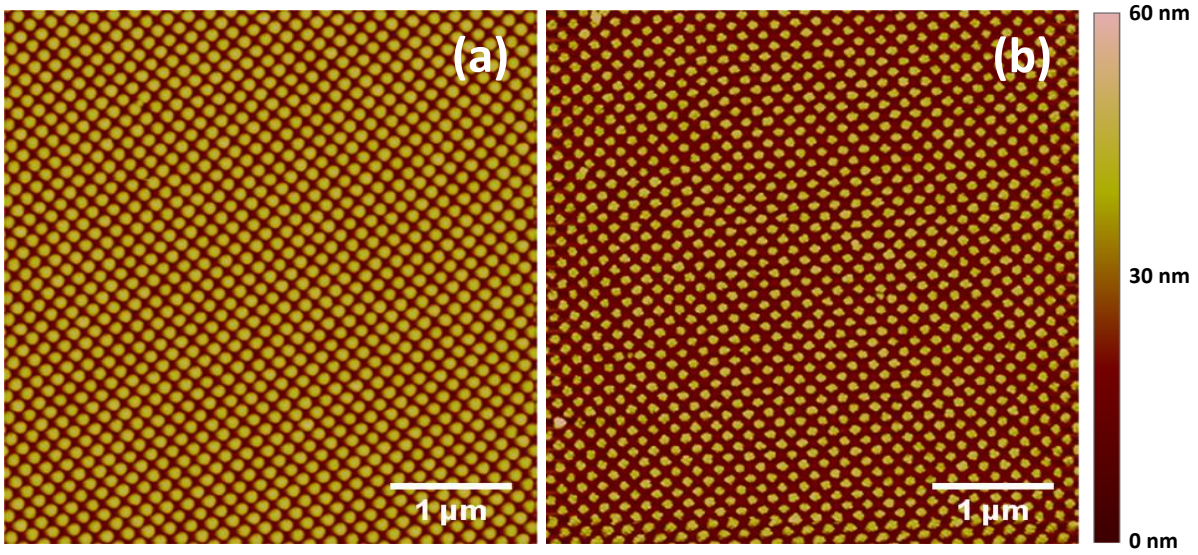

Figure 4.13: Tapping mode AFM height images of an array of 70 nm diameter pillars imprinted into a 100 nm thick layer of PMMA (a) before etching and (b) after etching.

One of the major advantages of using NIL is its inherent ability to pattern nanoscale structures over macroscopic areas. Imprinting the polymer layer to produce topographical features ranging from 10 nm to 10 µm is relatively straightforward. However, the accurate removal of the residual layer becomes much less simple for sub-100 nm structures. Here we used a mould consisting of an array of 70 nm diameter holes with 70 nm separations to imprint into a 100 nm thick layer of PMMA. Only AFM was used to characterise the surface since the features of the imprint were too small to be resolved clearly by any other technique available. Tapping mode height images of the imprinted PMMA surface before and after etching are shown in Figure 4.13 (a) and (b) respectively. The images show an array of bright spots, each spot corresponds to a 70 nm diameter pillar of PMMA. Both images demonstrate well defined nano arrays of PMMA structures. However, the scans only provide topographical data and cannot measure the thickness of the residual layer nor can it accurately distinguish between the substrate and the PMMA materials.

As stated previously, etching away the residual layer that surrounds each pillar of PMMA is not straightforward. Firstly the thickness of the residual layer cannot be measured and has to be estimated. Secondly, using RIE to etch such a thin film poses issues concerning the puncture depth of the ions bombarding the surface. For example, if the ions penetrate through

the PMMA with a depth that is equal to or greater than the height of the pillars (ca. 70 nm), then the pre-defined topographical pattern of PMMA structures will no longer act as a template for the silane patterns. Thirdly, characterising the imprinted surface by AFM provides no obvious distinction between the substrate and PMMA, thus determining the removal of the residual layer is vague.

The thickness of the residual layer can be estimated by using equations (1), (2) and (3) shown below, which assume that the original spin-coated layer of PMMA was 100 nm the depth of the holes in the mould is 70 nm and that 100% filling of the mould occurred during imprinting. The components of the three equations are illustrated in Figure 4.14, where $\boldsymbol{\chi^2}$ (15751.5 nm^2) is the area of the moulds surface within a repeat unit and $\mathbf{y^2}$ (3848.5 nm^2) is the area of the hole within that repeat unit, **a** (100 nm) is the thickness of the PMMA layer before imprinting, **b** (0.8) is the moulds surface to hole ratio (Eq. 1), **c** (70 nm) is the depth of the moulds holes, **d** is the thickness of the PMMA after imprinting (Eq. 2) and **r** is the thickness of the residual layer (Eq. 3). From these equations it was estimated that the maximum height of the PMMA after imprinting (**d**) was 156 nm and therefore the thickness of the residual layer (**r**) was 86 nm.

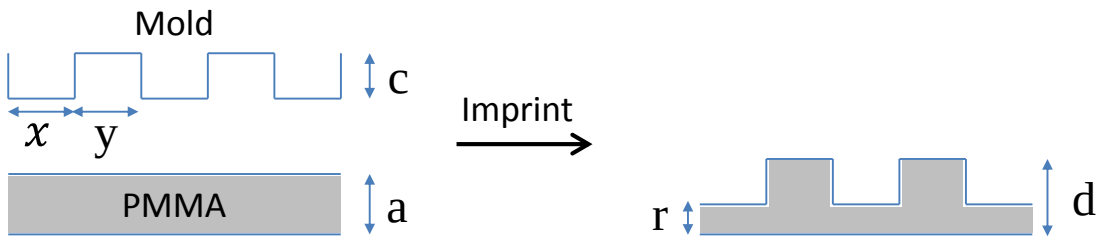

Figure 4.14: Diagram illustrating the components within the equations (1-3) used to estimate the residual layer of an imprint.

$$b = \frac{\chi^2}{(\chi^2 + y^2)} \quad (1)$$

$$d = a + bc \quad (2)$$

$$r = d - c \quad (3)$$

To ensure that the topography of the imprinted pattern is retained during the RIE process, the RF power was reduced to 40 W and the gas pressure was reduced by a lesser extent to 40 torr. The consequence of which are ions that bombard the surface with much less force, reducing the penetration depth of the ions. However, another consequence is that the anisotropic behaviour of the etch is also reduced.

To determine the removal of the residual layer surrounding the pillars of PMMA, the height of the pillars were measured by AFM before and after a range of etching times. It was assumed that the vertical etching rate of the PMMA would be constant over the topographical pattern, so that the heights of the pillar structures would remain unchanged until the residual layer had been etched away revealing the underlying substrate, at which point continued etching would result in a decrease in the height of the pillars. AFM tapping mode height images and corresponding line-sections of the 70 nm diameter pillar array at increasing etch times are shown in Figure 4.15. Figure 4.15 (a – d) show the surface topography after etching times of 0 s, 80 s, 90 s and 100 s respectively. The bright dots in the images correspond to the pillar structures. From image (a) to (d) a significant decrease in spot size is observed, the magnitude of which is caused by the reduction in the anisotropic nature of the etch process. Additionally, the uniformity of the pillar structures appears to decrease with increasing etch time. This is because the RIE process, although relatively uniform over microscopic areas, does not offer a high enough level of consistency on the nanometre scale. The corresponding line-sections (i – iv) to the right of the images clearly display a trend of decreasing peak heights, suggesting that the residual layer has been removed after 80 s. The line-section (i), corresponding to the 0 s etch sample, measures the pillars to be approx. 49 nm high, which is less than the expected value of 70 nm. This suggests that incomplete filling of the hole mould occurred during the imprinting process. When the average peak heights from the four line-sections are plotted against the etching time, as shown in Figure 4.16, it appears that the etching times of 80, 90 and 100 s form a linear trend. The etching time of 0 s lies off the linear trend because the thickness of the initial residual layer has not been taken into account. By extending the trend-line, it can be estimated that at an etching time of 55 s, parts of the substrate will start to become exposed at the thinnest regions of residual layer.

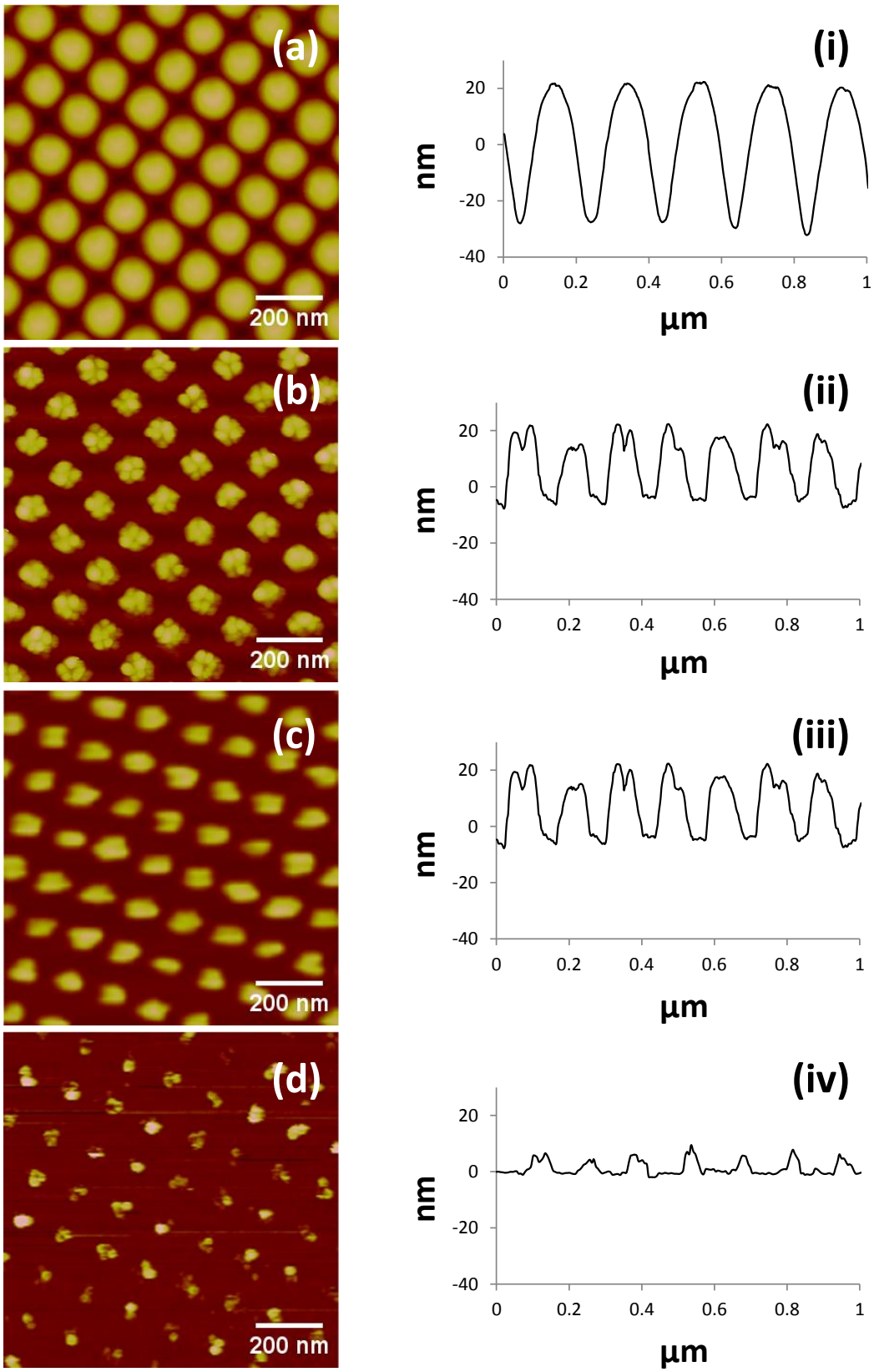

Figure 4.15: AFM tapping mode height images (right) and corresponding line sections (left) of an array of 70 nm diameter PMMA pillars (a) before etching, and after etching times of (b) 80 s, (c) 90 s and (d) 100 s.

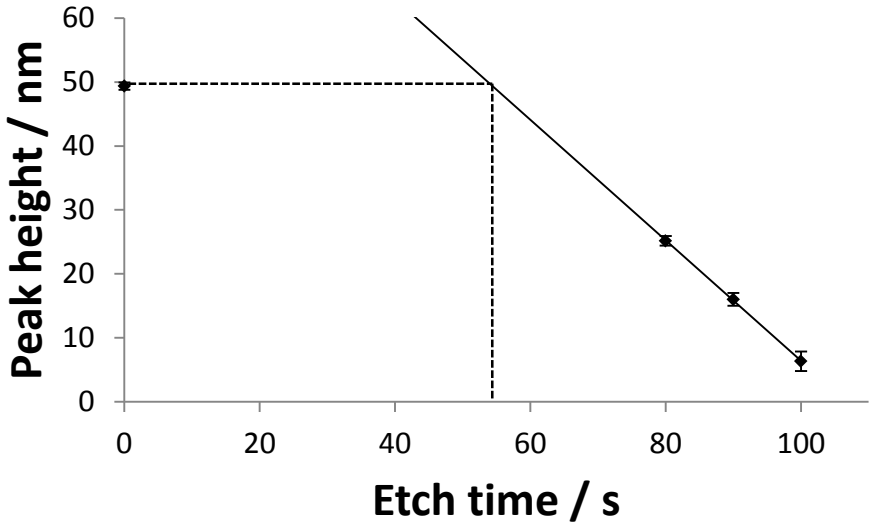

Figure 4.16: Graph of the average peak heights measured from AFM data against the etching time.

Following the complete removal of the residual layer, the area surrounding the PMMA pillars can be derivatised with PEG-silane, after which the pillars can be removed, yielding a surface pattern of APTES dots surrounded by PEG-silane. The surfaces were again characterised by AFM. Figure 4.17 (a) is a tapping mode AFM height image showing an array of darker dots approx. 70 nm diameter, which correspond to regions of APTES, with the surrounding PEG-silane displaying a lighter contrast. From the corresponding line-section (below image) the height difference between the regions of APTES and PEG-silane was measured to be approx. 3.5 nm, which is larger than expected. This same phenomenon was also observed for the 1.5 μm diameter dot pattern (Figure 4.8 (a)), and was explained by a vertical growth of the SiO_2 surrounding the PMMA pillar structures, caused by an extended etching time. This hypothesis could also apply here, because although there was not much of an extended etching time, the etching parameters were altered so that the physical component of the etch was extensively reduced, making the possible growth of the oxide layer by the chemical component of the etch more pronounced. Figure 4.17 (b) is a subtracted (trace – retrace) friction image of the same surface. The image shows an array of bright dots that correspond to APTES regions. From the line- section (below image) the frictional difference between the APTES and PEG-silane regions was measured to be approx. 60 mV, which is a relatively small value when compared to the micro- patterns.

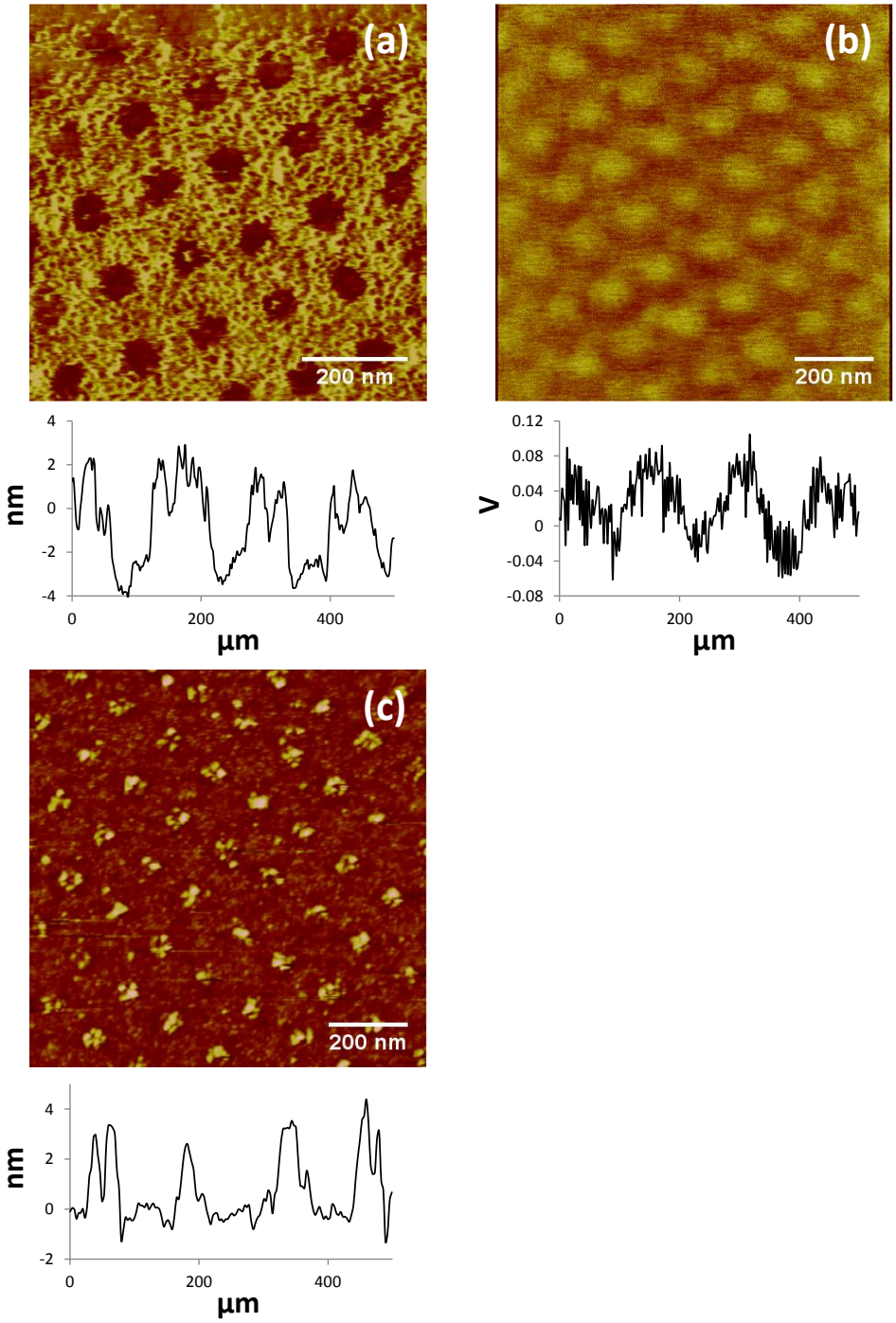

Figure 4.17: ***Top:*** *AFM (a) tapping mode height image and (b) contact mode subtracted (trace – retrace) friction image, measured from a surface patterned with 70 nm diameter dots of APTES surrounded by PEG-silane. Patterns were fabricated from a 100 nm thick layer of PMMA, imprinted by a 70 nm diameter hole mould.* ***Bottom:*** *(c) AFM tapping mode height image of the surface pattern after derivatisation of the APTES dots with biotin and subsequent absorption of streptavidin proteins. The corresponding line-sections are shown below each image.*

The nanoscale patterns of APTES dots were also used to bind streptavidin, and the resulting surface was characterised by AFM. The APTES was first derivatised with biotin, to increase the binding potential of the dots to the protein and also to add extra height to the subsequent dots of protein to aid their detecting by AFM. A tapping mode AFM height image of the surface is shown in Figure 4.17 (c), in which the dots of brighter contrast correspond to streptavidin immobilised on regions of biotinylated APTES. The diameters of the raised dots are ca. 60 nm, which is consistent with the fabricated dots of 70 nm diameter. The contrast observed in Figure 4.17 (c) shows an inversion in contrast compared to the surface pattern before biotinylation and protein adsorption (Figure 4.17 (a)), which is consistent with the addition of material on the APTES dots and not the surrounding surface of PEG-silane. The line-section (below image), measures the height difference between the dots and surrounding surface to be approx. 3.5 nm. When added to the value measured in Figure 4.17 (a), the height increase of the dots is estimated to be 7 nm, which is close to the value expected for an addition of a biotin molecule (ca. 1 nm) and a streptavidin protein (ca. 5 nm), suggesting that the APTES dots were successfully functionalised with biotin and then effectively bound streptavidin with nanometre control over the spatial organisation of the protein on the surface.

4.4 Conclusions

Topographical patterns of PMMA, fabricated by NIL on glass substrates, were successfully used to as a template for the surface patterning of APTES and PEG-silane. Two different methodologies were employed, enabling the use of both positive and negative moulds to produce arrays of APTES regions with defined dimensions. The resulting surface patterns were shown to bind proteins with high control over non-specific binding. The NIL process has demonstrated a simple, non-sequential way to produce micro- and nanoscale protein arrays over a macroscopic area.

Chapter Five

5 Reusable Micro and Nanoarrays for Protein Adsorption

5.1 Introduction

For many potential applications of nanotechnology in sensing and in fundamental studies of interfacial phenomena, methods are required that enable the fabrication of patterned proteins at the micro- and nanoscale over macroscopic areas[13, 35, 48, 67, 73, 207-210]. The most basic requirement is the ability to control the nonspecific adsorption of the protein. This problem has been addressed in a variety of ways most commonly by employing poly(ethylene glycol) (PEG), which resists the adsorption of proteins, in forms including SAMs[12-14, 126, 209-212], polymer brushers[184, 185], and hydrogels[107]. μCP has been used as a high throughput method to fabricate micron scale protein patterns over macroscopic areas[13, 91, 93, 213]. μCP uses an elastomeric stamp with surface relief structures to transfer an "inked" material onto a substrate. Additionally, low throughput, serial lithographic methods including SNP[35] and SPL[66, 67, 78, 214] have been used to pattern proteins with sub-100 nm spatial resolution. Furthermore, other high throughput methods such as massively parallel DPN and NIL have been used to pattern proteins over macroscopic areas with spatial resolution approaching 100 nm[76, 77, 215, 216]. However, even when high throughput methods are used the cost and speed of production for the fabrication of biocompatible surfaces is likely to struggle to meet the demands set by ever-advancing applications such as biosensing and proteomics. A solution would be to fabricate a reusable device, capable of patterning proteins, with the ability to then remove the adsorbed proteins simply, so that the device can be used again.

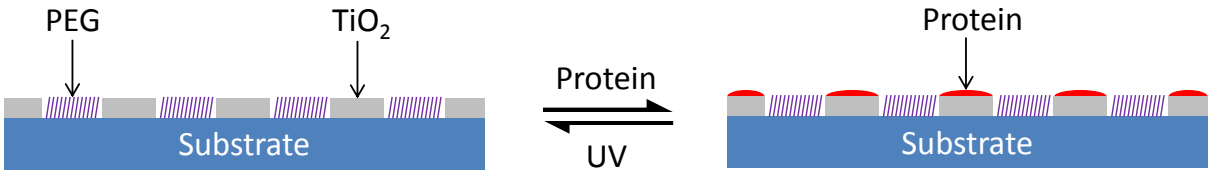

Figure 5.1: Schematic illustrating the TiO_2 structures as a switchable platform for protein adsorption and degradation.

TiO_2 was chosen as a suitable material for making a reusable biodevice, because it has been known to exhibit a strong effect of photocatalytic oxidation for decades[217]. The photocatalytic effect has since been used in applications including self-cleaning glass[218], water purification[219] and has also been shown to degrade SAMs[206, 220]. When the TiO_2 is irradiated with UV light, the electrons in the valence band are excited to the conduction band, resulting

in the formation of electron hole pairs, which then migrate to the surface of the solid. Positive holes present at the surface, oxidise surface bound water or organics, forming highly reactive hydroxyl radicals and CO_2 respectively. The hydroxyl radicals then go on to react with other nearby water or organic molecules. TiO_2 can exist in a number of different crystalline forms such as anatase and rutile, of which the anatase crystal structure exhibits the highest activity toward photocatalytic oxidation of organic pollutants[221]. TiO_2 adsorbs light predominantly within the UV-A (320 nm – 380 nm) region of the spectrum, with an absorbance maximum at approximately 340 nm.

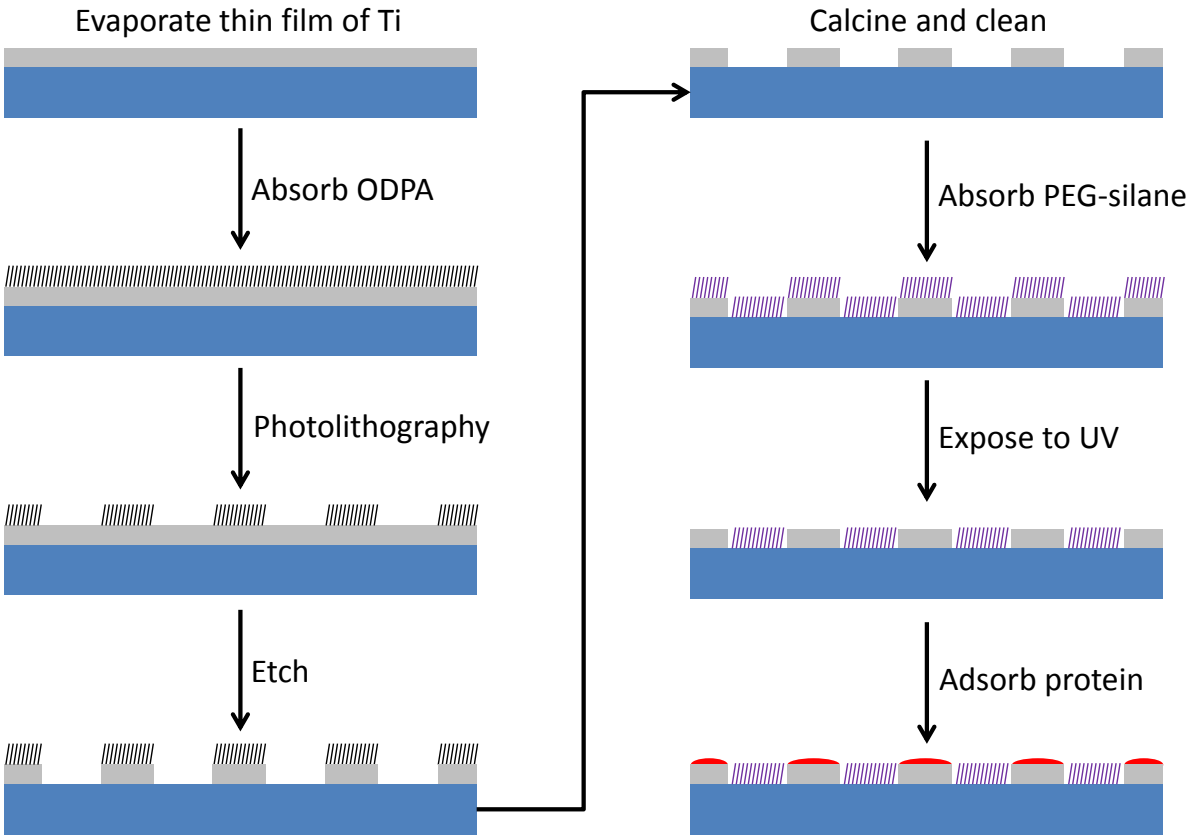

Figure 5.2: Schematic illustration of the steps involved in patterning the evaporated Ti layer. Octadecylphosphonic acid is used as a photoresist that can be patterned by exposure to a 244 nm beam of light, the subsequent exposed regions of titanium can be etched in a cool piranha solution. The patterned titanium substrate is then calcined at 400 ºC rendering it resistant to piranha etching and consequently a permanent structure that can be cleaned, functionalised, patterned, and cleaned again.

In the present chapter the use of photolithography and NIL to fabricate TiO_2 structures on glass substrates is explained. In particular, the goal was to explore the feasibility of using

TiO_2 structures as switchable platforms for protein adsorption and protein degradation (see schematic *Figure 5.1*). The surface of SiO_2 surrounding the TiO_2 structures is covered with a PEG terminated silane SAM to control nonspecific adsorption. Different lithographic methods were used to fabricate the functional surfaces, demonstrating the flexibility and ease of the fabrication process. *Figure 5.2* and *Figure 5.3* show schematically the processes used to fabricate TiO_2 structures functionalised with proteins by photolithographic methods and nanoimprinting respectively.

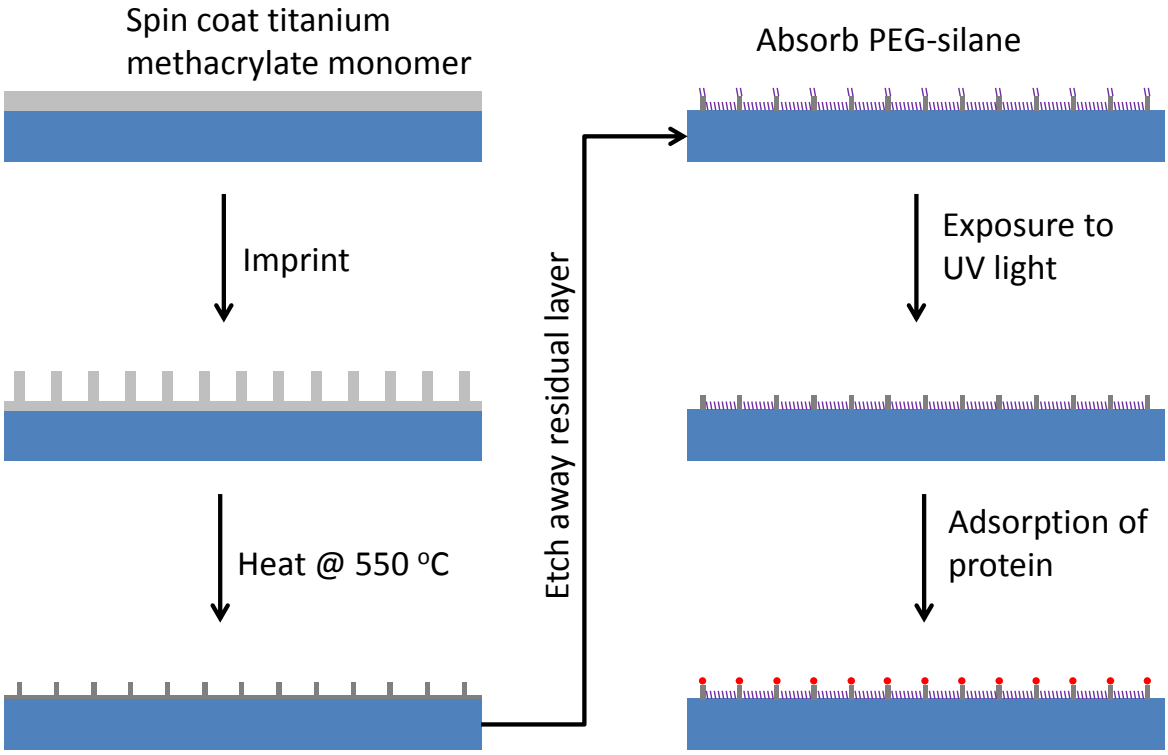

Figure 5.3: Schematic illustration of the steps involved in producing nano structured arrays of TiO_2 by NIL and RIE, including the subsequent derivatisation with PEG-silane for the formation of protein patterns.

5.2 Experimental

Photolithographic methods

A glass substrate was coated with a thin film of evaporated Ti. A SAM of ODPA was formed on the surface and exposed to UV light through a mask according to previously reported procedures[206]. Micron scale TiO_2 structures were fabricated by exposing the ODPA coated Ti

film to a focused laser beam (244 nm) through a TEM grid. Nano-scale TiO_2 structures were fabricated by IL using a Lloyd's mirror setup with a 244nm wavelength beam. Samples were etched, causing removal of Ti from areas exposed to UV light (where photocatalytic degradation caused removal of the SAM). After the etching step, samples were calcined in an oven at 400 ºC for 1 h and then cleaned with fuming piranha solution and rinsed with ultra-pure DI water. A PEG-silane film was formed over the sample and then removed from the TiO_2 structures by exposure to 325 nm wavelengths with an approx. dose of 8.6 J cm^{-2}. IgG-FITC or streptavidin-Cy3 proteins were then adsorbed onto the samples according to procedures described in section 2.7 for 2h. Subsequent removal of the protein was achieved by irradiating the sample at 325 nm wavelengths with an approx. dose of 14.4 J cm^{-2}.

Stencil Methods

Stencil lithography was carried out by using a TEM grid held in place on a clean glass slide. A thin film of Ti was evaporated onto the surface of the glass substrate through a mask. The Ti structures formed this way were calcined in an oven at 400 ºC for 1 h and then cleaned with fuming piranha solution and rinsed with ultra-pure DI water.

SAMs of PEG-silane were formed on the surfaces of the cleaned samples as described in section 2.4. The samples were then irradiated at 325 nm wavelengths by a He-Cd laser (IK3202R-D, Kimmon, Tokyo, Japan) with an approx. dose of 8.6 J cm^{-2}, to remove the PEG-silane molecules that were bound to the TiO_2 structures. Streptavidin-Cy3 proteins were then adsorbed onto the samples according to procedures described in section 2.7 for 2h.

Nanoimprinting

A solution of a Ti-containing methacrylate monomer was spin-coated onto glass substrate. The monomer film was imprinted with silicon moulds (NTT-AT, Japan) and cured by heating at 135 °C. The Ti-methacrylate (TiMA) resist was prepared according to previously reported procedures[222]. The Titanium (IV) *n* -butoxide (97%, Sigma Aldrich) was reacted with 2-(methacryloyloxy) ethyl acetoacetate (95%, Sigma Aldrich) in 1:2 molar ratio inside a glove box (<5% relative humidity) to form the chelated precursor with an alcohol as by product. Then, ethylene glycol dimethacrylate as a cross-linker was added to the chelated precursor followed by Benzoyl peroxide (BPO), an initiator for thermal free radical polymerization, purchased from Sinopharm Chemical Reagent. After the imprinting step, the samples were

calcined in an oven at 550 ºC for 1 h. The subsequent removal of the residual layer by RIE is described in section 2.9. The samples were then cleaned with fuming piranha solution and rinsed with ultra-pure DI water. SAMs of PEG-silane were formed on the surfaces of the cleaned samples as described in section 2.4. The samples were then irradiated by a UV-A lamp emitting wavelengths in the range 320 nm – 400 nm for 3 min to remove the PEG-silane molecules bound to the TiO_2 structures. Wheat germ agglutinin-fluorescein (WGA-fluorescein) or streptavidin-Cy5 proteins were then adsorbed onto the samples according to procedures described in section 2.7, for up to 24 h. Subsequent removal of the protein was achieved analogous to the removal of the PEG-silane, by irradiating the sample with a UV-A lamp for 3 min.

5.3 Results and Discussion

Fabrication by Photolithography

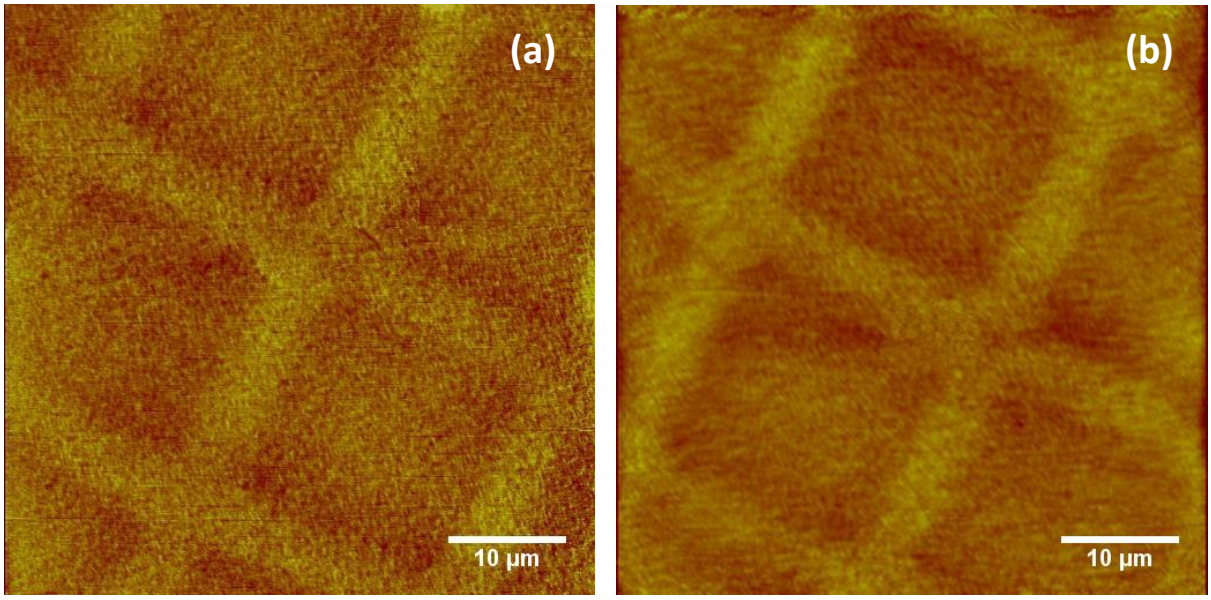

Figure 5.4: AFM images showing (a) height and (b) friction contrast measured on the surface of an ODPA coated titanium film after an exposure dose of 23 J cm^{-2} with 244 nm wavelength.

Figure 5.4 shows AFM height and friction images of an alkylphosphonate SAM on TiO_2 after exposure to UV light through a mask (a TEM grid). Both images exhibit a pattern of bright bars, corresponding to regions masked during exposure, and squares, where photocatalytic degradation has caused removal of the adsorbate. Visible mask patterns in both the surface

topography (a) and friction contrast (b) can be seen, suggesting some form of chemical modification has occurred. A cross-section of Figure 5.4 (a) (not shown) shows a height difference between the exposed (squares) regions and masked (bars) regions of approx. 2 nm, which is consistent with the loss of a monolayer such as ODPA.

By selectively removing regions of the ODPA monolayer, the underlying Ti film can be selectively etched away according to the predetermined photolithographic pattern. Piranha solution was used to etch exposed regions of the Ti film. For the TiO_2 patterns to be used as functional and reusable protein arrays it is essential that isolated Ti features are fabricated in the etching step. The optimum etch time yields complete removal of the Ti from exposed areas, while leaving masked (SAM-coated) regions intact, and was determined by a process of trial-and-error. By taking topographical profiles of the surface to measure the height of the Ti features the complete removal of the Ti in the exposed regions can be determined. Figure 5.5 shows two tapping mode height images and their corresponding cross-sections of exposed samples.

Figure 5.5 (a) shows the surface topography after 20 min immersion in piranha solution. The height of the lines was measured to be ca. 11 nm. After a further 5 min of etching, the height of the lines decreased to ca. 7 nm. Since the rate at which the Ti film is etched (vertically) should be constant over the whole pattern, a decrease in line height suggests over-etching, as a result of removal of some material from areas exposed to minima in the interferogram, suggesting that the Ti has been completely removed from areas exposed to maxima in the interferogram.

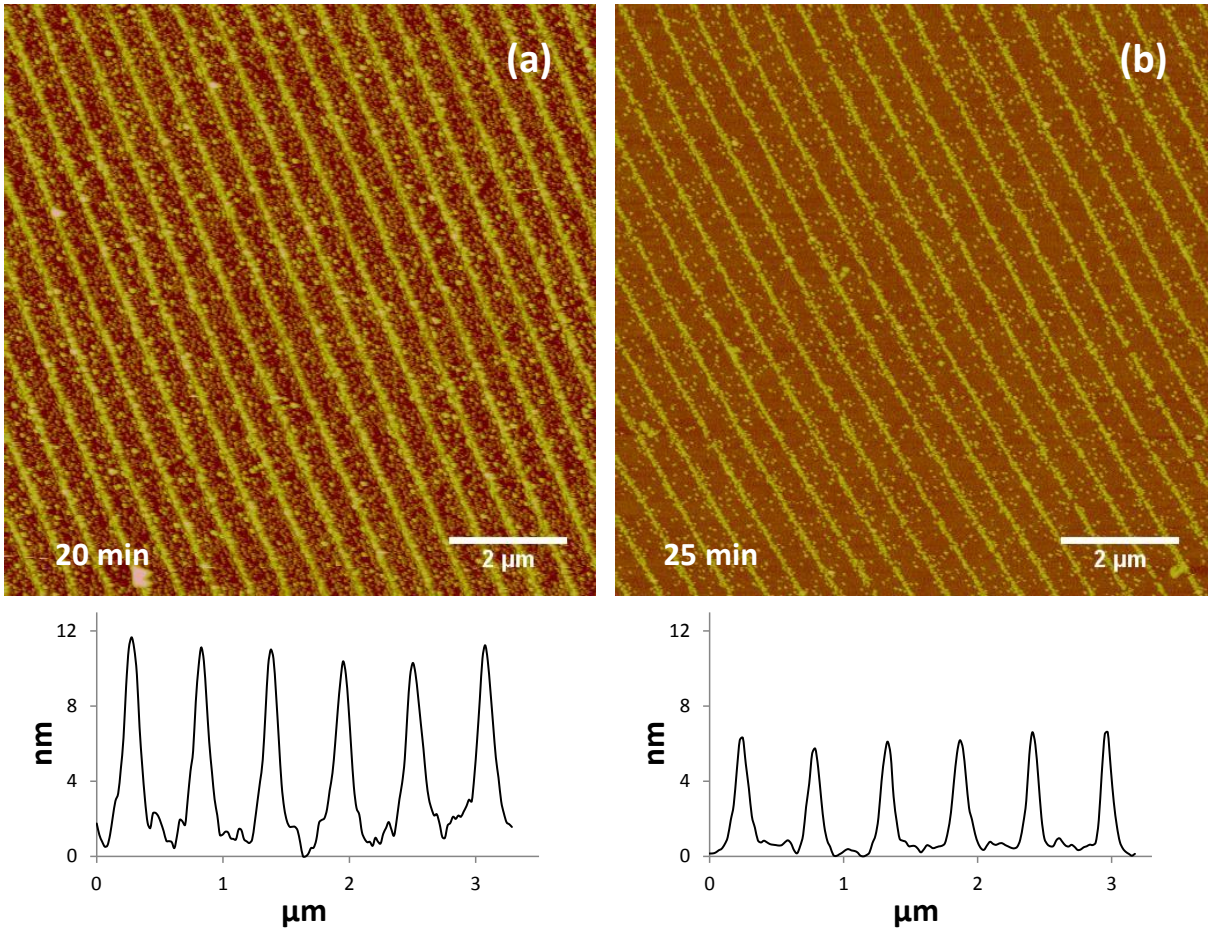

Figure 5.5: AFM tapping mode images and corresponding cross-sections below, of TiO_2 nano-lines patterned by IL, after etching times of (a) 20 min and (b) 25 min. Line widths measure 100 nm with a period of 550 nm for both etching times. The heights of the lines decreases from approx. 11 nm for a 20 min etch, to approx. 7 nm for a 25 min etch.

After calcination the Ti structures, consisting of Ti metal covered with a thin native oxide, are transformed into highly crystalline TiO_2. The resulting TiO_2 is known to possess superior photocatalytic oxidation activity, which is advantageous as it increases the rate at which it can degrade nearby organic material. It was observed that after calcination the TiO_2 structures were unaffected by immersion in piranha solution, even at temperatures close to 100 ºC. The apparent resistance to etching allows the samples of patterned TiO_2 to be cleaned using fuming piranha to remove any contaminants prior to the formation of a SAM on the surface.

For the application of patterning proteins, PEG-silane, was used because it is known to form densely packed films that prohibit the adsorption of biological material. PEG-silane was

coated onto the surface of the glass substrate and then was selectively removed from the TiO_2 structures by irradiating the sample to a wavelength of 325 nm. Photons with a wavelength of 325 nm have energies greater than the bandgap of TiO_2, so will induce photocatalytic oxidation and degrade the PEG-silane adsorbed on TiO_2 structures. However, exposure to 325 nm is not expected to affect the PEG-silane SAM that resides on regions of SiO_2. It was thus expected that immersion of the sample in a protein solution would lead to protein adsorption onto the TiO_2 structures, leaving the PEG-silane coated regions clean. Samples treated in this fashion were characterised by scanning laser confocal microscopy. Figure 5.6 (a) and (b) show two fluorescent images taken of micro patterned samples that have been immersed into a solution of IgG-FITC then rinsed and dried. The bright green bars correspond to TiO_2 structures coated in the fluorescently tagged protein, while the dark squares correspond to regions of surface between the Ti bars that are coated with protein-resistant PEG-silane. The strong contrast difference between the bar and the square regions confirms that the protein adsorbs strongly to the TiO_2, and is completely repelled from the PEG-silane. A control sample, which did not receive a dose of 325 nm light was analysed and exhibited no fluorescence. This suggests that the PEG-silane monolayer forms over the SiO_2 and TiO_2 and then is selectively removed with UV over the TiO_2 structures.

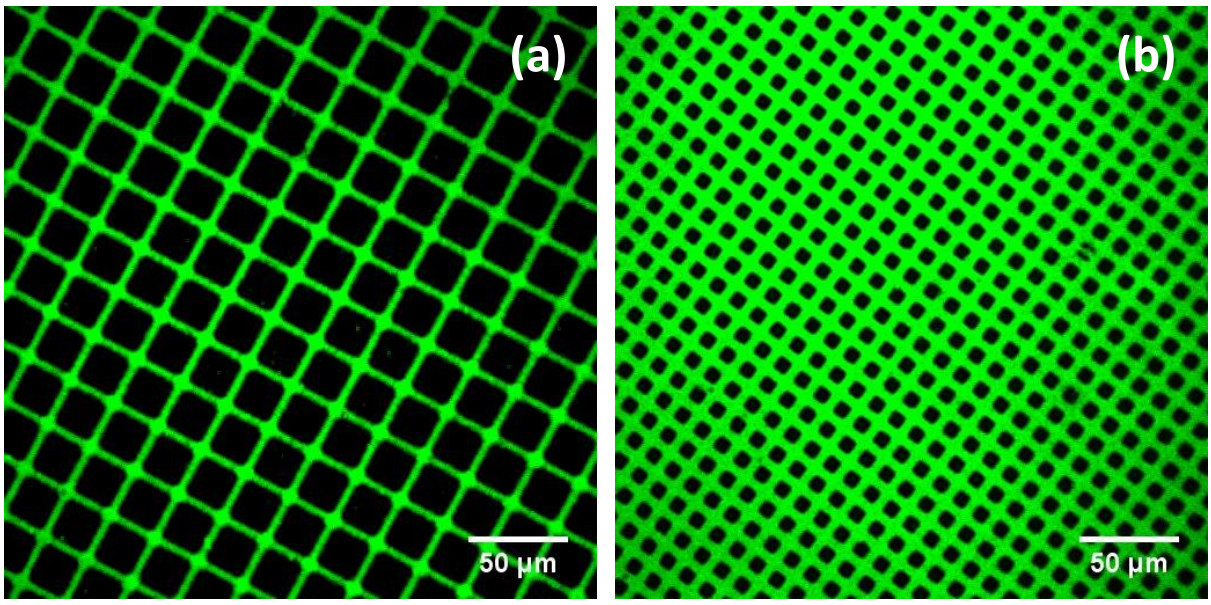

Figure 5.6: Fluorescent images of (a) 1000 mesh (b) 2000 mesh, grid patterns of IgG-FITC proteins adsorbed onto a template of TiO_2 structures fabricated on glass.

To demonstrate that these samples can be cleaned and reused to pattern a second protein, they were first exposed to 325 nm light and analysed by confocal microscopy. No fluorescence was observed confirming removal of all proteins. The samples were then immersed into a solution containing a second protein labelled with a fluorescent dye. The resulting fluorescent images of the surface are shown in Figure 5.7, where (a) and (b) are images of the same samples in Figure 5.6 (a) and (b) respectively, after UV exposure and immersion in a solution of streptavidin-Cy3. Both images show a good contrast in the fluorescent signal between the bars and the square regions suggesting that that the process has led effectively to the replacement of the first protein by the second one. The contrast seen in Figure 5.7 however is not as good as in Figure 5.6, as some red dots are seen within the square regions. However, this is likely to be noise because a lower intensity of fluorescence was exhibited by the Cy3 compared to the FITC giving a lower noise to signal ratio. An alternative explanation is that the PEG chains have been degraded by the exposure to UV, either directly by the light itself or indirectly by small deposits of TiO_2, which were not completely etched away, inducing photocatalytic oxidation; such an explanation cannot be discounted completely, although the evidence suggests the OEG degradation rates are low at 325 nm[212].

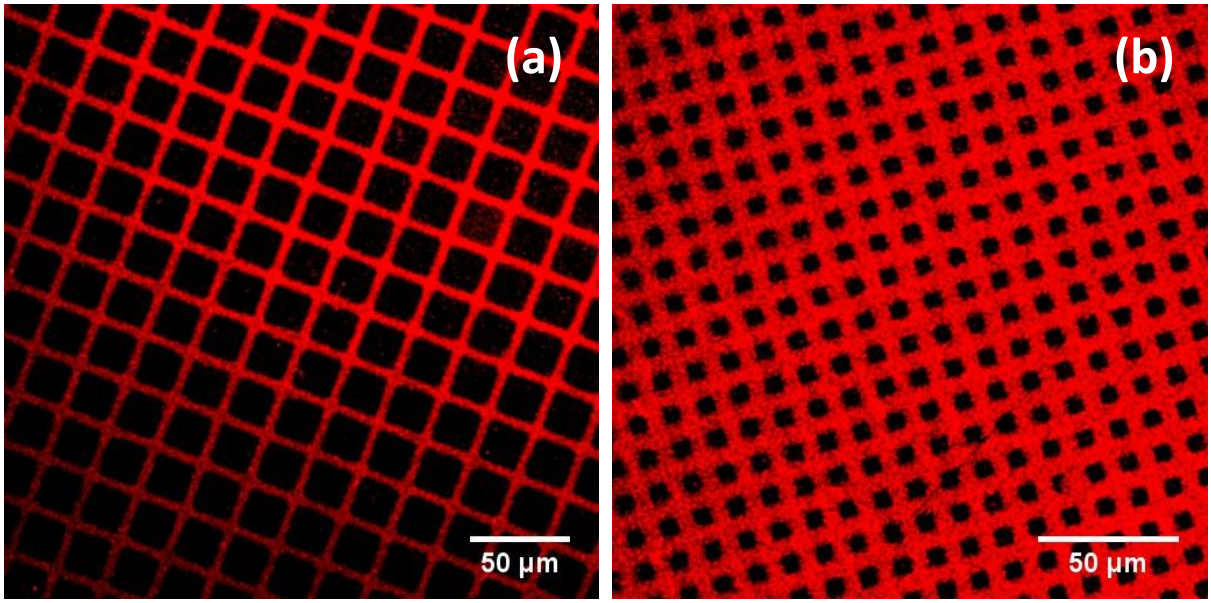

Figure 5.7: Fluorescent images of (a) 1000 mesh and (b) 2000 mesh, grid patterns of streptavidin-Cy3 proteins adsorbed onto a template of TiO_2 structures fabricated on glass. Images (a) and (b) are of the same samples shown in Figure 5.6 (a) and (b) respectively, after exposure to UV to remove the IgG-FITC and subsequent immersion in a streptavidin-Cy3 solution.

On inspection of the fluorescence images in Figure 5.8, which shows the samples after a third exposure to UV and subsequent immersion in an IgG-FITC solution, a similar level of contrast is observed between the bar and square regions, compared with the first protein adsorption shown in Figure 5.6.

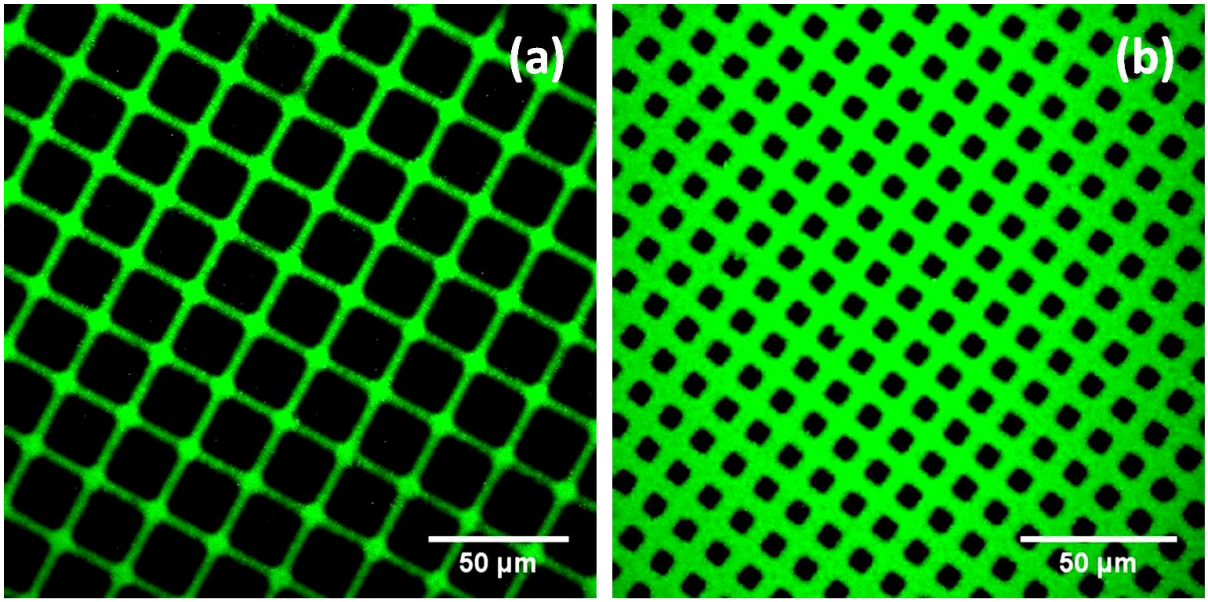

Figure 5.8: Fluorescent images of the same samples shown in Figure 5.6 Figure 5.7, following a third cycle of UV exposure and subsequent immersion in IgG-FITC solution.

Proteins were also adsorbed onto the patterns of TiO_2 nano lines fabricated by IL. Figure 5.9 (a) shows the fluorescence image of the surface after immersion in a solution of streptavidin-Cy3. Fluorescence parallel lines are observed from the sample consistent with the interference pattern. The difference in contrast between the exposed and masked lines is not clearly seen in the image. This is because the small width and spacing of the lines are at the limit of the imaging capabilities of the confocal microscope used for the analysis. However, distinction of the fluorescent lines becomes clearer when a cross-section of the intensity is taken as shown in Figure 5.9 (b). Individual peaks can be defined with a constant period of 550 nm, which is consistent with the period of TiO_2 nano lines measured by AFM (Figure 5.5). The presence or degree of non-specific adsorption between the nanolines cannot be accurately determined from this, but it is clear from the intensity profile that the majority of protein is adsorbed onto the TiO_2 lines.

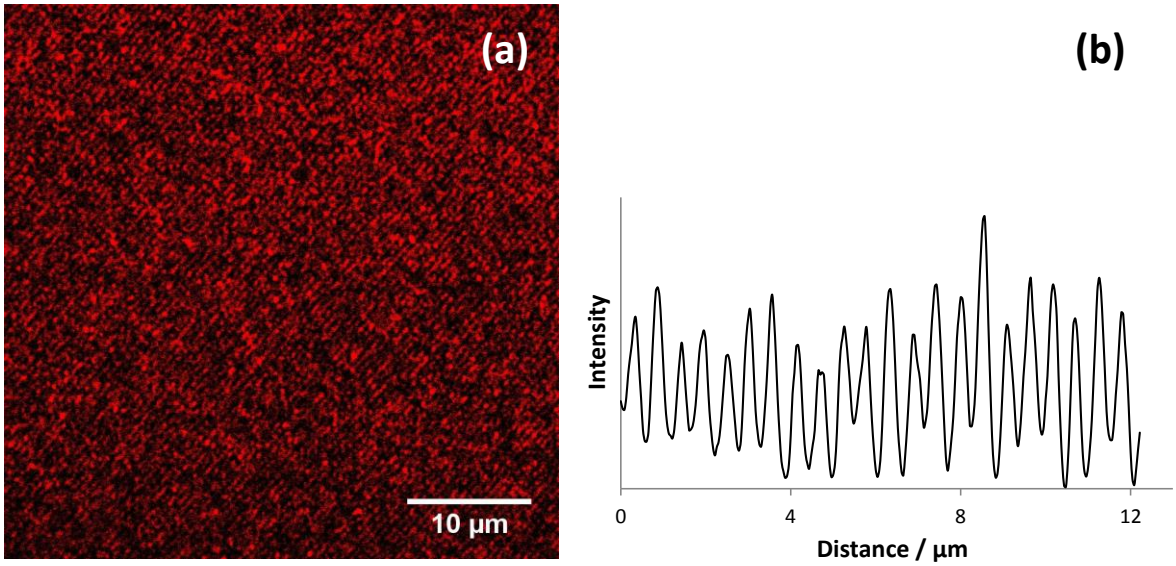

Figure 5.9: (a) Fluorescent image and (b) intensity profile cross-section, of streptavidin-Cy3 adsorbed onto TiO_2 nano lines. The peaks in the intensity profile have a period of approx. 550 nm, which is the same value as measured by AFM.

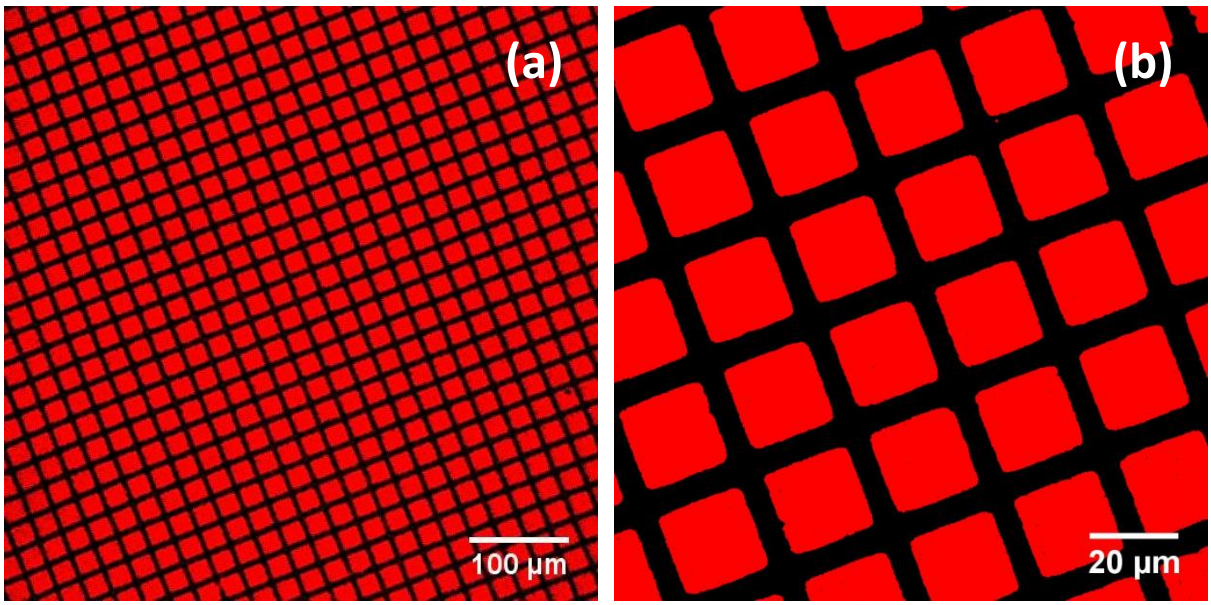

Figure 5.10: Fluorescent images of streptavidin Cy3 tag specifically bound to a sample of which has been patterned with TiO_2 and PEG-silane. Showing areas of (a) 600 μm^2 and (b) 130 μm^2.

Samples were also fabricated by stencil lithography, which does not require the use of ODPA as a photo-resist or an etching step. This was achieved by simply placing a TEM grid onto the substrate during the evaporation of the Ti. The areas of the substrate covered by the grid are

shielded from the depositing metal, thus yielding patterns of Ti directly onto the glass surface. The samples can then be calcined, cleaned and derivatised with PEG-silane as previously described. This process is obviously much faster and simpler than the processes carried out when using photolithographic methods. Most importantly, removal of the etching step makes the fabrication of the TiO_2 structures considerably more consistent and repeatable. However, this method is only suitable for micro- scale patterns because it is limited by the diffusion of the metal ions underneath the masked areas. Figure 5.10 shows fluorescent images of a sample, fabricated by stencil lithography, after immersion in a solution of streptavidin-Cy3. Figure 5.10 (a) was taken at low magnification and shows a relatively large area of the surface, which illustrates the high degree of pattern uniformity as well as the lack of defects. Figure 5.10 (b) was taken at a higher magnification, which illustrates the high degree of control over the protein organisation. Outstanding contrast is observed between the square (protein coated TiO_2) and bar (PEG-silane) regions, demonstrating that this method is a simple way to produce highly precise micron scale arrays of patterned proteins.

Fabrication by Nanoimprinting

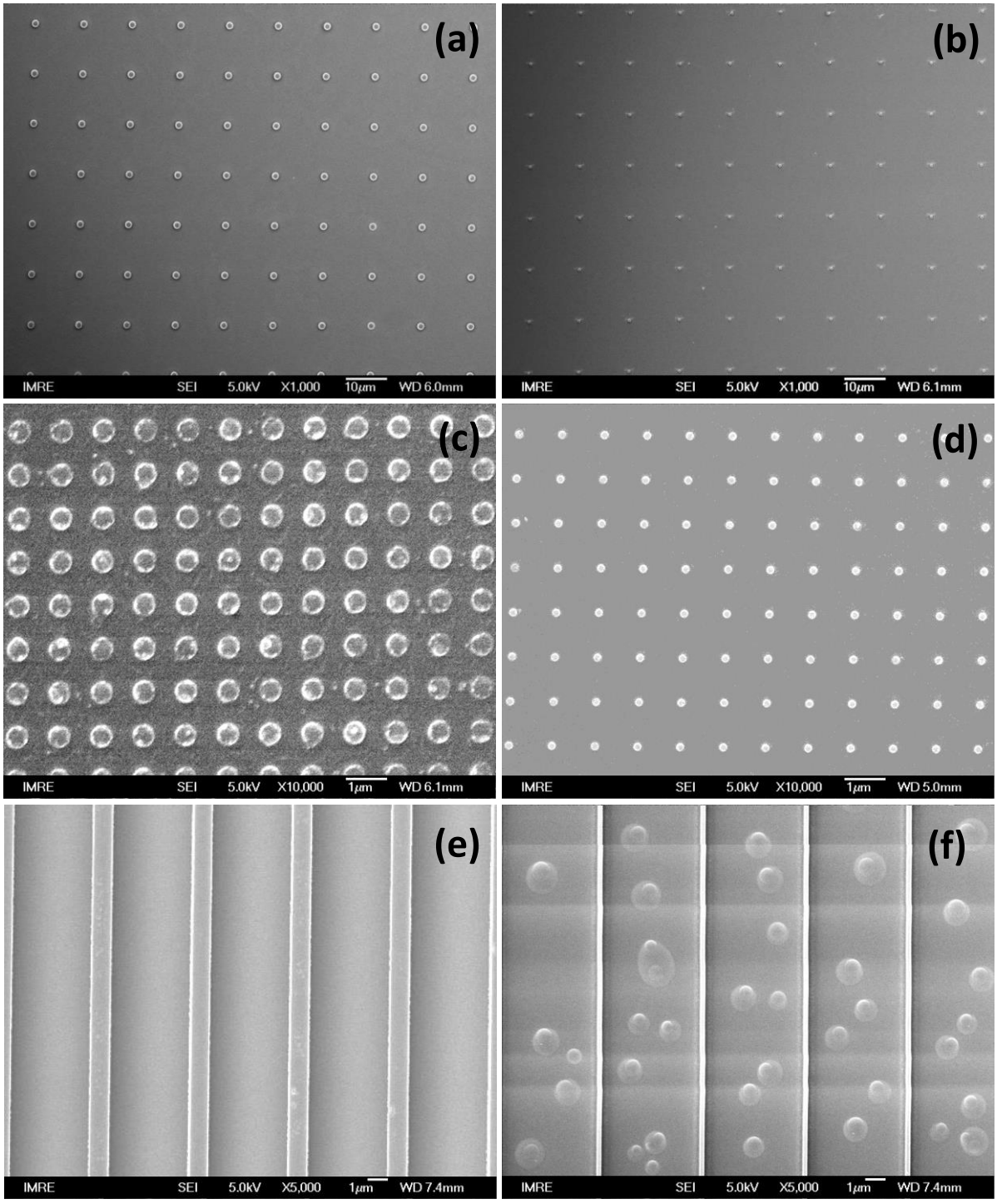

Figure 5.11: SEM images of imprinted pillar structures of Ti resist. Image (a), (c) and (e) show the structure before calcination and image (b), (d) and (f) show the structures after calcining at 550 ºC. The diameters of the pillars in images (a)-(d) are 2 µm, 0.6 µm, 0.5 µm and 0.2 µm respectively. The widths of the lines in images (e) and (f) are 1 µm and 0.25 µm respectively.

Spin coated films of Ti resist were imprinted with a variety of different moulds. The samples were then calcined to remove the organic material within the resist, forming a crystalline oxide. The heating process induces a shrinking effect on the imprinted structures due to the loss of the organic material. The degree of shrinkage can be analysed using SEM. *Figure 5.11* shows SEM images of imprinted pillar and line arrays before [(a), (c) and (e)] and after [(b), (d) and (f)] calcination. By comparing image (a) with (b) and image (c) with (d) it can be calculated that the pillar diameters have reduced from 2 µm to 0.6 µm (70% reduction) and 0.5 µm to 0.2 µm (60% reduction) respectively. And by comparing image (e) with (f) it can be calculated that the width of the lines has reduced from 1 µm to 0.25 µm (75% reduction).

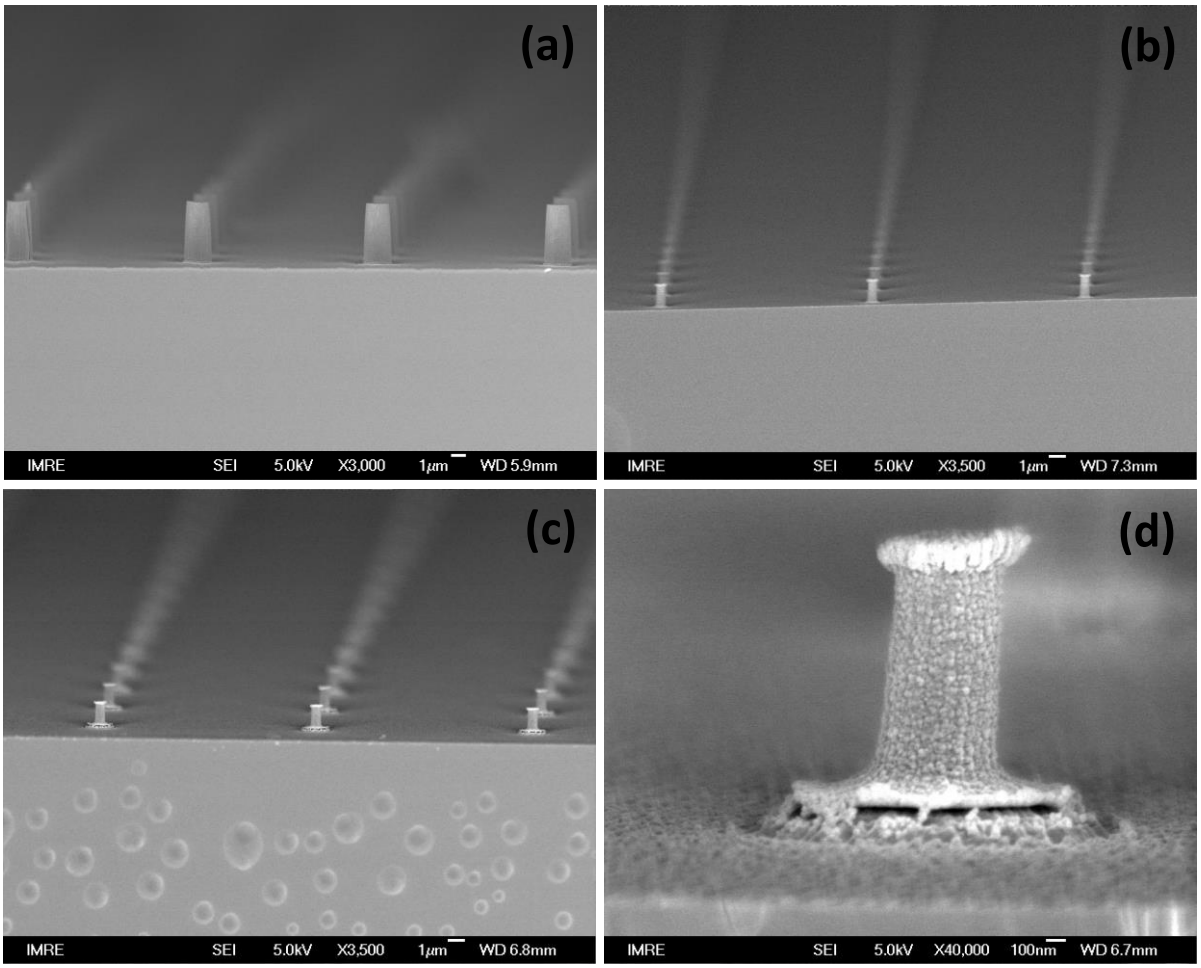

Figure 5.12: SEM cross-section images of (a) an array of imprinted Ti resist pillars, (b) after calcining at 550 ºC, (c) after reactive ion etching with SF_6 and Ar gasses and (d) a high magnification image showing complete removal of the TiO_2 residual layer

After the imprinting step a residual layer of Ti resist remains on the surface between the features. After calcination the thickness of the residual layer is also reduced and can appear to have been removed since it becomes too thin to resolve clearly with an SEM. However, it is likely that a thin film still remains, which must be removed in order to create isolated structures of TiO_2. The residual layer was removed by RIE, using a combination of SF_6 and Ar gasses. The gaseous mixture is able to etch the TiO_2, but will also etch the underlying SiO_2 so it is important to determine a precise etching time where the residual layer of TiO_2 is completely removed without over-etching and removing the TiO_2 structures.

The precise removal of the residual layer can be determined by imaging the cross-section of the imprinted structures by SEM. Figure 5.12 shows the stages from the initial imprint (a), after calcination (b) and after etching (c). Image (d) shows a high magnification view of a single pillar after the etching step. This image clearly shows the interface between the TiO_2 pillar structure and the SiO_2 below and surrounding it, with a definite edge to the TiO_2, suggesting it is an isolated TiO_2 structure.

Once the patterns of isolated TiO_2 have been fabricated, a SAM of PEG-silane is then formed across the surface. The PEG-silane will absorb to both the SiO_2 and TiO_2 regions and so in order to facilitate protein binding the PEG-silane is removed from the TiO_2 structures by exposure to a UV source. UV exposure yields a surface consisting of unmodified TiO_2 structures surrounded by anti-fouling PEG chains.

Protein patterns were made by immersing the sample in a protein solution, resulting in proteins spontaneously adsorbing exclusively onto the TiO_2 structures. Figure 5.13 shows fluorescent images of WGA-fluorescein adsorbed onto three different array patterns of TiO_2 structures fabricated by NIL. Figure 5.13 (a) and (b) show arrays of TiO_2 dots with diameters of approx. 600 nm and 200 nm, and periods of 12 µm, 1 µm respectively. Figure 5.13 (c) shows an array of TiO_2 lines with widths of approx. 250 nm and a period of 5 µm. The contrast in the images is excellent and no non-specific protein binding is observed, demonstrating the successful formation of a uniform PEG-silane SAM, and its subsequent removal from the TiO_2 structures. The dimensions of the fluorescent regions in the three images correlate well with the dimensions of the TiO_2 structures measured by SEM. This indicates that the TiO_2 residual layer has been sufficiently removed and that the protein has only adsorbed to the isolated TiO_2 structures.

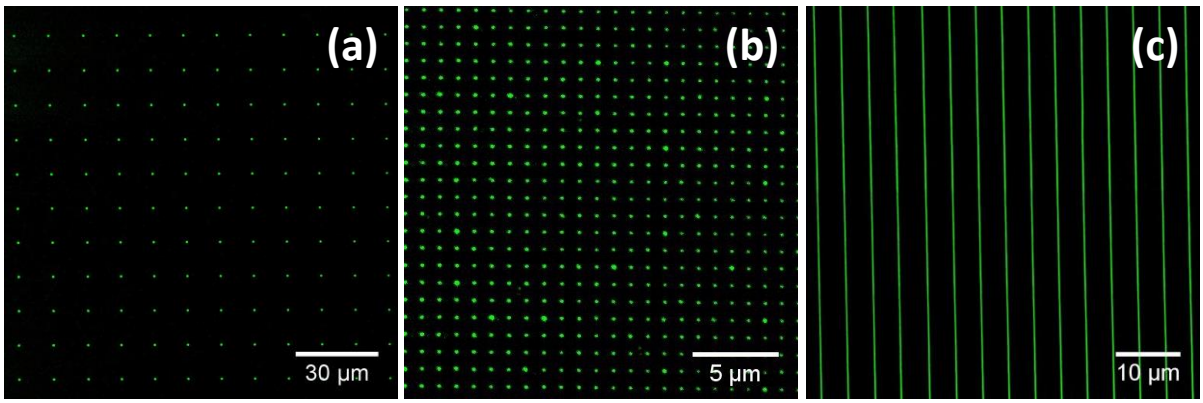

Figure 5.13: Fluorescent confocal images showing WGA-fluorescein adsorbed to TiO_2 patterns of (a) 0.6 µm dots, (b) 0.2 µm dots and (c) 0.25 µm lines.

To determine whether the samples were reusable, cycles of UV exposure followed by immersion in an alternating protein solution were carried out and characterised by scanning laser confocal microscopy. For this only the patterns of dot arrays shown in Figure 5.13 (a) and (b) were tested as these are the most appropriate configurations for protein nanoarrays. Figure 5.14 shows a collection of fluorescent images and their corresponding intensity profiles, taken on the same sample of 600 nm dots, after consecutive cycles showing the 1st to the 10th and final protein adsorption. The proteins were alternated from streptavidin-Cy5 (red) to WGA-fluorescein (green) from the 1st to the 10th cycle. On comparison of the fluorescent images, there is no noticeable difference in the degree of non-specific binding, size of the fluorescing dots or defects. Comparison of the 1st and 5th (both red), and 2nd and 10th (both green) cycles show no visible differences in contrast, however the contrast changes slightly between the green to red dots (better contrast seen for green dots), but this is because of the properties of the fluorescent dyes and not a consequence of any changes to the sample pattern itself. Comparison of the intensity profiles also shows no significant differences from the 1st to the 10th cycle. Because no noticeable decrease in sample performance was observed after 10 cycles, it was evaluated that this sample could continue being reused for a considerable number of times more.

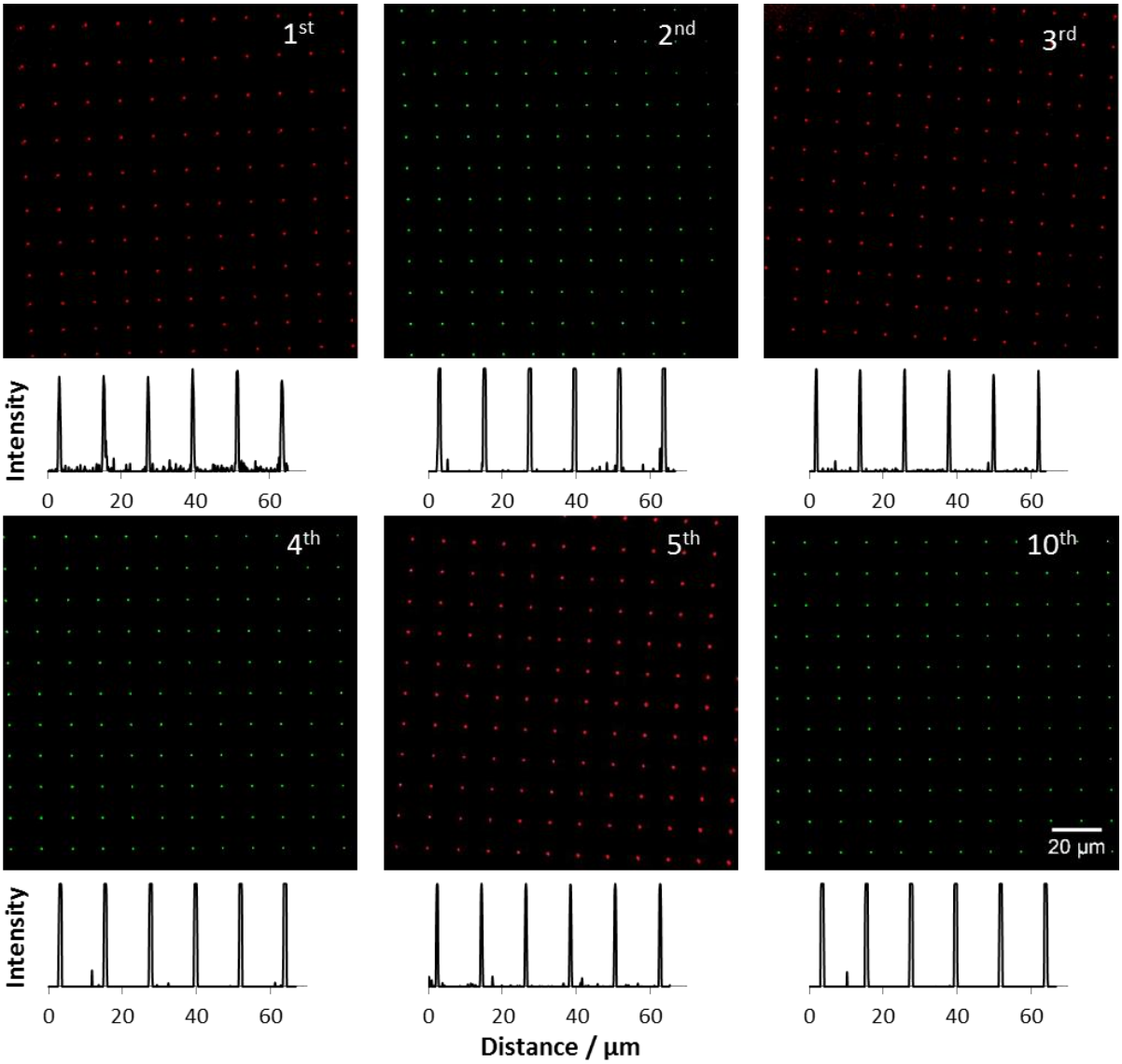

Figure 5.14: Fluorescent confocal images of the same 0.6 µm TiO_2 dot array sample after consecutive adsorption by emersion and removal by photocatalytic oxidation, of two alternating proteins, streptavidin-Cy5 (red) and WGA-fluorescein (green) with their corresponding intensity profiles below. The cycle of binding protein, then exposing to UV light then binding with a second protein was carried out 10 times on the same sample and showed no changes in fluorescent intensity. non-specific binding or sample quality. The scale bar show in the bottom right image is applicable to all the fluorescent images in the figure.

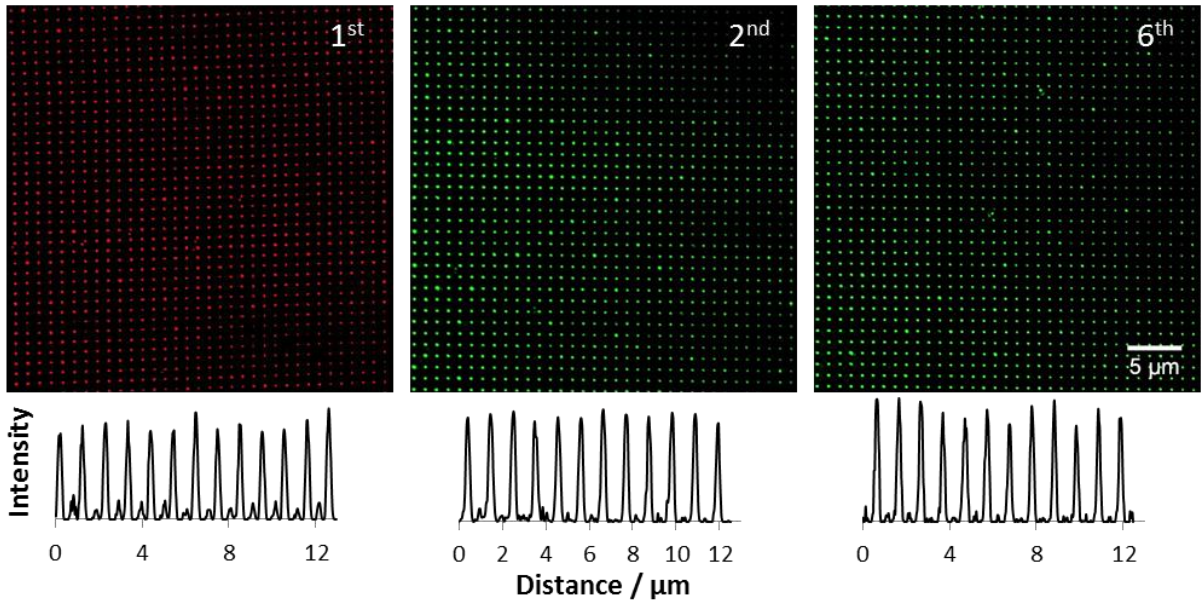

Figure 5.15: Fluorescent confocal images of the same 0.2 µm TiO_2 dot array sample after consecutive adsorption by emersion and removal by photocatalytic oxidation, of two alternating proteins, streptavidin-Cy5 (red) and WGA-fluorescein (green) with their corresponding intensity profiles below. The sample was cycled six times without showing any significant changes in fluorescent intensity or non-specific binding. The scale bar show in the bottom right image is applicable to all the fluorescent images in the figure.

Figure 5.15 shows a set of fluorescent images and their corresponding intensity profiles taken on the same sample of 200 nm dots, showing the 1st, 2nd and 6th cycles. On inspection of the fluorescent images and their corresponding intensity profiles, there are no significant changes in the intensity or diameter of the fluorescing dots. Moreover, little or no sign of non-specific protein adsorption is visible in any of the images. This sample was cycled 4 additional times and analysed after the 10th cycle. However, no determinable image of the dot array was acquired. When viewed through the microscope, the surface appeared patchy with fluorescence, but no clear pattern was visible. It was not determined at which point or how this happened, but at some point from the 6th to the 10th cycle, the sample lost its ability to function. Possible causes of the loss in function could include contamination of the surface, degradation of the PEG-silane molecule caused by a low level of TiO_2 still remaining between the pillar structures, or dislodgment of the pillar structures themselves caused by repetitive rinsing and handling of the sample. Despite the eventual loss in function, the sample of 200 nm dots has demonstrated that it can be reused up to 6 times and possibly

more, which is still impressive and a useful attribute compared to a conventional protein array that can only be used once.

5.4 Conclusions

Micron and nano scale patterns of TiO_2 were fabricated on glass substrates by photolithographic methods (mask and IL), stencil lithography and NIL. An anti-fouling monolayer of PEG-silane was used to coat the patterned surfaces and then was successfully removed from the TiO_2 structures by photocatalytic oxidation yielding a surface consisting of bare TiO_2 structures surrounded by a PEG-silane monolayer formed on the underlying SiO_2 surface. These patterns were then demonstrated to bind proteins with very high control over their spatial organisation on the surfaces.

For patterns generated by photolithographic methods, regions of Ti were shown to be etched away by immersion in cool piranha solution, producing Ti structures ranging from a few microns to sub-100 nm in size. Following protein adsorption, characterisation by confocal microscopy of the micron scale grid patterns, exhibited regions of densely packed proteins with no non-specific adsorption detected between the TiO_2 structures. Successive removal and re-adsorption of a different protein was carried out two times on the same sample. Fluorescent micrographs of the different proteins patterned showed no difference in the samples ability to bind and control the spatial organisation the protein. Patterns of TiO_2 nanolines were not clearly resolved by the confocal microscope. However, a pattern of lines could be seen in the fluorescent micrograph and the intensity cross-section of which, showed peaks with the correct period for the TiO_2 lines and troughs with intensity values close to 0. Subsequent removal of the protein and re-adsorption of a different protein was not carried out on the nano line sample because of time constraints. Additionally, patterns were fabricated by stencil methods, which demonstrated producing patterns that exhibited outstanding control over the proteins spatial organisation. Fluorescent micrographs showed intensely bright square regions with no sign of non-specific adsorption between them. Subsequent removal of the protein and re-adsorption of a different protein was not carried out because of time constraints.

For patterns fabricated by NIL, a spin-coated layer of TiMA monomer was imprinted with a variety of array patterns. Calcination of the imprinted resist was achieved and resulted in a decrease in structure sizes, ranging from 60% - 75%. The residual layer was shown to be

removed by RIE using a combination of SF_6 and Ar gasses producing isolated TiO_2 structures. With the addition of a patterned PEG-silane monolayer, characterisation by confocal microscopy showed that in all cases the protein adsorbed exclusively to the TiO_2 structures, producing fluorescent micrographs exhibiting high intensity from the TiO_2 structures, with no visible non-specific adsorption. Successive removal and re-adsorption of a different protein was carried out on 2 different pillar array patterns. A sample consisting of an array of pillars, 0.6 µm in diameter, was shown to be reused 10 times without exhibiting any loss in performance. No subsequent protein adsorptions were attempted. A sample consisting of an array of pillars, 0.2 µm in diameter, was shown to be reused 6 times without exhibiting any loss in performance. However, no determinable fluorescent micrograph was acquired for the sample after a 10^{th} cycle of being reused. The cause in the samples loss in function was not determined.

Chapter Six

6 Conclusions and Future Work

6.1 Conclusions

The present work has shown the potential of combining large-area nano-lithographic techniques with molecular self-assembly to produce nanostructured functional arrays over macroscopic areas. Moreover, the use of patterned siloxane films on glass substrates offers advantages in bionanotechnology because of their chemical stability, optical transparency and absence of fluorescence quenching. True demonstrations of top-down and bottom-up nano-fabrication have been demonstrated. Including the fabrication of a novel biosensor, that can be recycled using the phenomenon, photo-catalytic oxidation.

In chapter 3, photolithographic methods were used to pattern a photo-reactive film of NPPOC-silane. The resulting patterns were used to grow a non-fouling polymer brush (polyOEGMA) by SI-ATRP. IL demonstrated fabrication of periodic nanoscale polyOEGMA structures over a macroscopic area. It was observed that defined regions of polymer were only measured at low exposures, because of the high density of the pattern that caused an overlapping of the polymer at high exposures. SNP was used to fabricate multi-functional patterns in the NPPOC-silane film and polyOEGMA was grown from the patterns. A pattern of parallel lines with increasing scan-speed was employed to investigate the effects of initiator density on the growth and structure of the polymer. A linear increase in polymer height with increasing initiator density was measured. A better understanding of the growth and structural properties of biocompatible polymer brushes can lead to the fabrication of nano-channels defined by the brushes, which are able to direct and control proteins within a flowing solution as part of a biodevice.

In chapter 4, NIL was used to indirectly pattern films of APTES and PEG-silane for protein adsorption. A film of PMMA was imprinted; the resulting topographical pattern was used as a template for silane deposition. Micro- and nanoscale arrays were fabricated over macroscopic areas. These arrays of chemical patterns were demonstrated to adsorb proteins with control over the spatial organisation of the protein. An array of 70 nm diameter dots was fabricated. The dots of APTES were functionalised with biotin and then demonstrated to immobilise streptavidin proteins, confirmed by a change in height measured by AFM. This nano-scale array shows good control over the absorption of streptavidin and because of the relative flatness of the pattern area, the proteins and other biomolecules can be identified and probed, suggesting it would have many applications in proteomics.

In chapter 5, structures of TiO_2 were fabricated on a substrate by photolithographic methods and NIL. Both lithographic techniques demonstrated micro- and nanoscale patterns over macroscopic areas. Mask photolithography and IL methods were used to degrade a phosphonate SAM adsorbed onto a film of Ti. The patterned SAM acted as a resist during the etching of the Ti film, resulting in patterned Ti structures. After calcination of the sample it was observed that the Ti structures became resistant to etching, indicating a transformation to crystalline TiO_2. NIL was used to imprint a Ti-containing methacrylate polymer. Following calcination and etching, patterned strictures of TiO_2 were created. The patterned TiO_2 structures were used in combination with a molecular film of PEG-silane for the adsorption of proteins. It was observed that upon exposure to UV light, organic matter in contact with the TiO_2 was removed by photocatalytic oxidation. The patterns of TiO_2 structures were able to pattern an adsorbed protein, then the protein was removed my UV exposure, then a different protein was patterned. The cycle of protein adsorption and removal was carried out 10 times on the same sample with no increase in non-specific adsorption detected by fluorescence microscopy, demonstrating a method towards a reusable protein array. The work in this chapter has demonstrated the fabrication of a reusable protein array, which has the potential to be further developed into a fully functional biosensor able to detect a wide range of proteins and used over and over again by simple means, saving money and resources. The model of using nano-arrayed TiO_2 domains as switchable platforms for protein adsorption and degradation would have serious value in proteome expression and in future biodiagnostics.

6.2 Future Works

For the deprotection of the NPPOC-silane film at 325 nm and 244 nm, a large difference in the water contact angle of the fully deprotected film was observed. It was hypothesised that irradiation of the film at 244 nm could cause photo-oxidation or degradation of the molecules, resulting in a more hydrophilic surface. However, this was not fully investigated. Surface analysis techniques such as SIMS and XPS should be used to systematically examine the effects of exposure of the film at 244 nm to determine if any photo-oxidation or degradation occurs.

An issue of overlapping polymer regions was observed for polyOEGMA grown from interferograms. Alterations to the IL setup can be made to increase the period of the interferogram, resulting in a larger gap between polymer regions, therefore decreasing the amount of overlapping. Testing the patterns ability to pattern proteins should also be carried out.

SNP was used to produce a gradient in grafting density for a set of parallel lines of polyOEGMA. The structure of the polymer was examined by tapping mode AFM. However, the characterisation was done in air and not under aqueous conditions. The polymer behaves very differently when solvated in water and could better indicate a transition between the mushroom and brush regimes. Additionally, immersion of the sample in a fluorescent protein solution and subsequent characterisation by fluorescence microscopy could examine the polyOEGMA's ability to resist protein adsorption at varying grafting densities as well as varying lateral dimensions.

NIL demonstrate the fabrication of an array of nanoscale, biotin functionalised dots over a macroscopic area that were able to specifically immobilise streptavidin proteins. The size of the dots (ca. < 70 nm in diameter) are approaching the dimensions of some large biological molecules. Because of the nature of the NIL process, it is highly conceivable that even smaller arrays could be fabricated, leading to a pattern of immobilised biological molecules that can be characterised as single molecules.

Arrays of TiO_2 structures were fabricated on glass substrate and in combination with a PEG-silane film were shown to pattern proteins. However, the proteins were only physisorbed onto the TiO_2 structures. An additional step to functionalise the TiO_2 structures, before protein

adsorption, with molecules that specifically attach proteins through the formation of a phosphonic acid SAM, would add extra functionality to the device.

Chapter Seven

7 References

1. B. D. Gates, Q. B. Xu, J. C. Love, D. B. Wolfe and G. M. Whitesides, *Annu. Rev. Mater. Res.*, 2004, 34, 339-372.

2. G. M. Whitesides and D. J. Lipomi, *Faraday Discuss.*, 2009, 143, 373-384.

3. Y. Chen and A. Pepin, *Electrophoresis*, 2001, 22, 187-207.

4. B. D. Gates, Q. B. Xu, M. Stewart, D. Ryan, C. G. Willson and G. M. Whitesides, *Chem. Rev.*, 2005, 105, 1171-1196.

5. P. Fortina, L. J. Kricka, S. Surrey and P. Grodzinski, *Trends Biotechnol.*, 2005, 23, 168-173.

6. N. L. Rosi and C. A. Mirkin, *Chem. Rev.*, 2005, 105, 1547-1562.

7. P. O. Brown and D. Botstein, *Nature Genetics*, 1999, 21, 33-37.

8. J. N. Anker, W. P. Hall, O. Lyandres, N. C. Shah, J. Zhao and R. P. Van Duyne, *Nat. Mater.*, 2008, 7, 442-453.

9. R. Merkel, P. Nassoy, A. Leung, K. Ritchie and E. Evans, *Nature*, 1999, 397, 50-53.

10. T. E. Fisher, P. E. Marszalek and J. M. Fernandez, *Nat. Struct. Biol.*, 2000, 7, 719-724.

11. B. Rupp and F. Nedelec, *Lab on a Chip*, 2012, 12, 4903-4910.

12. K. L. Prime and G. M. Whitesides, *Science*, 1991, 252, 1164-1167.

13. G. P. Lopez, M. W. Albers, S. L. Schreiber, R. Carroll, E. Peralta and G. M. Whitesides, *J. Am. Chem. Soc.*, 1993, 115, 5877-5878.

14. E. Ostuni, R. G. Chapman, R. E. Holmlin, S. Takayama and G. M. Whitesides, *Langmuir*, 2001, 17, 5620.

15. B. Dong, S. Manolache, A. C. L. Wong and F. S. Denes, *Polym. Bull.*, 2011, 66, 517-528.

16. S. L. McArthur, K. M. McLean, P. Kingshott, H. A. W. St John, R. C. Chatelier and H. J. Griesser, *Colloids Surf., B*, 2000, 17, 37-48.

17. R. G. Chapman, E. Ostuni, M. N. Liang, G. Meluleni, E. Kim, L. Yan, G. Pier, H. S. Warren and G. M. Whitesides, *Langmuir*, 2001, 17, 1225-1233.

18. K. Ishihara, E. Ishikawa, Y. Iwasaki and N. Nakabayashi, *J. Biomater. Sci., Polym. Ed.*, 1999, 10, 1047-1061.

19. K. Ishihara, T. Hasegawa, J. Watanabe and Y. Iwasaki, *Artificial Organs*, 2002, 26, 1014-1019.

20. S. Herrwerth, W. Eck, S. Reinhardt and M. Grunze, *J. Am. Chem. Soc.*, 2003, 125, 9359-9366.

21. F. Rusmini, Z. Y. Zhong and J. Feijen, *Biomacromolecules*, 2007, 8, 1775-1789.

22. R. H. Stulen and D. W. Sweeney, *Quantum Electron.*, 1999, - 35, - 699.

23. M. D. Levenson, *Physics Today*, 1993, 46, 28-36.

24. G. J. Leggett, *Chem. Soc. Rev.*, 2006, 35, 1150-1161.

25. C. W. Gwyn, R. Stulen, D. Sweeney and D. Attwood, *J. Vac. Sci. Technol., B*, 1998, 16, 3142-3149.

26. F. N. Goodall, R. A. Lawes and G. G. Arthur, *Microelectron. Eng.*, 1990, 11, 187-195.

27. H. Sewell, J. McClay, P. Jenkins, B. Tirri, D. Flagello and J. Mulkens, *J. Photopolym. Sci. Technol.*, 2002, 15, 569-576.

28. R. L. Brainard, J. Cobb and C. A. Cutler, *J. Photopolym. Sci. Technol.*, 2003, 16, 401-410.

29. M. D. Levenson, N. S. Viswanathan and R. A. Simpson, *Electron Devices, IEEE Transactions on*, 1982, 29, 1828-1836.

30. S. Sun and G. J. Leggett, *Nano Lett.*, 2002, 2, 1227.

31. K. Critchley, L. Zhang, H. Fukushima, M. Ishida, T. Shimoda, R. J. Bushby and S. D. Evans, *J. Phys. Chem. B*, 2006, 110, 17174.

32. H. Sugimura, T. Hanji, O. Takai, T. Masuda and H. Misawa, *Electrochim. Acta*, 2001, 47, 107.

33. C. S. Dulcey, J. H. Georger, V. Krauthamer, D. A. Stenger, T. L. Fare and J. M. Calvert, *Science*, 1991, 252, 551-554.

34. J. H. Georger, D. A. Stenger, A. S. Rudolph, J. J. Hickman, C. S. Dulcey and T. L. Fare, *Thin Solid Films*, 1992, 210, 716-719.

35. S. Sun, M. Montague, K. Critchley, M.-S. Chen, W. J. Dressick, S. D. Evans and G. J. Leggett, *Nano Lett.*, 2006, 6, 33.

36. T. Griesser, J. Adams, J. Wappel, W. Kern, G. J. Leggett and G. Trimmel, *Langmuir*, 2008, 24, 12420-12425.

37. Patchorn.A, B. Amit and R. B. Woodward, *J. Am. Chem. Soc.*, 1970, 92, 6333.

38. S. P. A. Fodor, J. L. Read, M. C. Pirrung, L. Stryer, A. T. Lu and D. Solas, *Science*, 1991, 251, 767-773.

39. S. Y. Chou, P. R. Krauss and P. J. Renstrom, *Appl. Phys. Lett.*, 1995, 67, 3114-3116.

40. A. Rodriguez, M. Echeverria, M. Ellman, N. Perez, Y. K. Verevkin, C. S. Peng, T. Berthou, Z. B. Wang, I. Ayerdi, J. Savall and S. M. Olaizola, *Microelectron. Eng.*, 2009, 86, 937-940.

41. A. Yariv and M. Nakamura, *IEEE J. Quantum Electron.*, 1977, 13, 233-253.

42. W. W. Ng, C. S. Hong and A. Yariv, *IEEE Transactions on Electron Devices*, 1978, 25, 1193-1200.

43. S. R. J. Brueck, *J. Proc. IEEE*, 2005, 93, 1704.

44. C. Lu and R. H. Lipson, *Laser Photon. Rev.*, 2009, 1-13.

45. J. de Boor, D. S. Kim and V. Schmidt, *Opt. Lett.*, 2010, 35, 3450-3452.

46. T. M. Bloomstein, M. F. Marchant, S. Deneault, D. E. Hardy and M. Rothschild, *Opt. Express*, 2006, 14, 6434-6443.

47. S. Sun and G. J. Leggett, *Nano Lett.*, 2004, 4, 1381-1384.

48. M. Montague, R. E. Ducker, K. S. L. Chong, R. J. Manning, F. J. M. Rutten, M. C. Davies and G. J. Leggett, *Langmuir*, 2007, 23, 7328-7337.

49. R. E. Ducker and G. J. Leggett, *J. Am. Chem. Soc.*, 2005, 128, 392-393.

50. P. Vettiger, G. Cross, M. Despont, U. Drechsler, U. Durig, B. Gotsmann, W. Haberle, M. A. Lantz, H. E. Rothuizen, R. Stutz and G. K. Binnig, *IEEE Transact. Nanotech.*, 2002, 1, 39-55.

51. E. u. Haq, Z. Liu, Y. Zhang, S. A. A. Ahmad, L.-S. Wong, S. P. Armes, J. K. Hobbs, G. J. Leggett, J. Micklefield, C. J. Roberts and J. M. R. Weaver, *Nano Lett.*, 2010, 10, 4375-4380.

52. A. N. Broers, W. W. Molzen, J. J. Cuomo and N. D. Wittels, *Appl. Phys. Lett.*, 1976, 29, 596-598.

53. A. E. Grigorescu and C. W. Hagen, *Nanotechnology*, 2009, 20, 292001.

54. V. Sidorkin, E. van Veldhoven, E. van der Drift, P. Alkemade, H. Salemink and D. Maas, *J. Vac. Sci. Technol., B*, 2009, 27, L18-L20.

55. A. A. Tseng, *Small*, 2005, 1, 924-939.

56. R. D. Piner, J. Zhu, F. Xu, S. H. Hong and C. A. Mirkin, *Science*, 1999, 283, 661-663.

57. J. Haaheim, R. Eby, M. Nelson, J. Fragala, B. Rosner, H. Zhang and G. Athas, *Ultramicroscopy*, 2005, - 103, - 132.

58. S. H. Hong, J. Zhu and C. A. Mirkin, *Science*, 1999, 286, 523-525.

59. S. H. Hong and C. A. Mirkin, *Science*, 2000, 288, 1808-1811.

60. H. Jung, R. Kulkarni and C. P. Collier, *J. Am. Chem. Soc.*, 2003, 125, 12096-12097.

61. D. J. Pena, M. P. Raphael and J. M. Byers, *Langmuir*, 2003, 19, 9028-9032.

62. K. H. Kim, J. D. Kim, Y. J. Kim, S. H. Kong, S. Y. Jung and H. Jung, *Small*, 2008, 4, 1089-1094.

63. A. Noy, A. E. Miller, J. E. Klare, B. L. Weeks, B. W. Woods and J. J. DeYoreo, *Nano Lett.*, 2002, 2, 109-112.

64. B. W. Maynor, S. F. Filocamo, M. W. Grinstaff and J. Liu, *J. Am. Chem. Soc.*, 2002, 124, 522-523.

65. L. M. Demers, D. S. Ginger, S. J. Park, Z. Li, S. W. Chung and C. A. Mirkin, *Science*, 2002, 296, 1836-1838.

66. A. J. Senesi, D. I. Rozkiewicz, D. N. Reinhoudt and C. A. Mirkin, *ACS Nano*, 2009, 3, 2394-2402.

67. K. B. Lee, S. J. Park, C. A. Mirkin, J. C. Smith and M. Mrksich, *Science*, 2002, 295, 1702-1705.

68. E. Bellido, R. de Miguel, D. Ruiz-Molina, A. Lostao and D. Maspoch, *Adv. Mater.*, 2010, 22, 352.

69. Y. Cho and A. Ivanisevic, *J. Phys. Chem. B*, 2005, 109, 6225-6232.

70. J. C. Garno, Y. Y. Yang, N. A. Amro, S. Cruchon-Dupeyrat, S. W. Chen and G. Y. Liu, *Nano Lett.*, 2003, 3, 389-395.

71. G. Gundiah, N. S. John, P. J. Thomas, G. U. Kulkarni, C. N. R. Rao and S. Heun, *Appl. Phys. Lett.*, 2004, 84, 5341-5343.

72. L. Fu, X. G. Liu, Y. Zhang, V. P. Dravid and C. A. Mirkin, *Nano Lett.*, 2003, 3, 757-760.

73. D. S. Ginger, H. Zhang and C. A. Mirkin, *Angew. Chem. Int. Ed.*, 2004, 43, 30-45.

74. K. Salaita, Y. Wang and C. A. Mirkin, *Nat. Nanotech.*, 2007, 2, 145-155.

75. C.-C. Wu, D. N. Reinhoudt, C. Otto, V. Subramaniam and A. H. Velders, *Small*, 2011, 7, 989-1002.

76. K. Salaita, Y. Wang, J. Fragala, R. A. Vega, C. Liu and C. A. Mirkin, *Angew. Chem. Int. Ed.*, 2006, 45, 7220-7223.

77. S. Lenhert, P. Sun, Y. Wang, H. Fuchs and C. A. Mirkin, *Small*, 2007, 3, 71-75.

78. S. Xu and G.-y. Liu, *Langmuir*, 1997, 13, 129.

79. J. E. Headrick, M. Armstrong, J. Cratty, S. Hammond, B. A. Sheriff and C. L. Berrie, *Langmuir*, 2005, 21, 4122.

80. R. Maoz, E. Frydman, S. R. Cohen and J. Sagiv, *J. Adv. Mater.*, 2000, 12, 725.

81. Y. N. Xia and G. M. Whitesides, *Annu. Rev. Mater. Sci.*, 1998, 28, 153-184.

82. Y. N. Xia, J. A. Rogers, K. E. Paul and G. M. Whitesides, *Chem. Rev.*, 1999, 99, 1823-1848.

83. A. Kumar and G. M. Whitesides, *Appl. Phys. Lett.*, 1993, 63, 2002-2004.

84. Y. N. Xia, M. Mrksich, E. Kim and G. M. Whitesides, *J. Am. Chem. Soc.*, 1995, 117, 9576-9577.

85. D. W. Wang, S. G. Thomas, K. L. Wang, Y. N. Xia and G. M. Whitesides, *Appl. Phys. Lett.*, 1997, 70, 1593-1595.

86. L. B. Goetting, T. Deng and G. M. Whitesides, *Langmuir*, 1999, 15, 1182-1191.

87. U. Zschieschang, M. Halik and H. Klauk, *Langmuir*, 2008, 24, 1665-1669.

88. G. Csucs, R. Michel, J. W. Lussi, M. Textor and G. Danuser, *Biomaterials*, 2003, 24, 1713-1720.

89. T. Chen, R. Jordan and S. Zauscher, *Small*, 2011, 7, 2148-2152.

90. D. Arrington, M. Curry and S. C. Street, *Langmuir*, 2002, 18, 7788-7791.

91. C. D. James, R. C. Davis, L. Kam, H. G. Craighead, M. Isaacson, J. N. Turner and W. Shain, *Langmuir*, 1998, 14, 741-744.

92. A. Bernard, J. P. Renault, B. Michel, H. R. Bosshard and E. Delamarche, *Adv. Mater.*, 2000, 12, 1067-1070.

93. Z. Wang, P. Zhang, B. Kirkland, Y. Liu and J. Guan, *Soft Matter*, 2012, 8, 7630-7637.

94. S. A. Lange, V. Benes, D. P. Kern, J. K. H. Horber and A. Bernard, *Anal. Chem.*, 2004, 76, 1641-1647.

95. M. Mrksich, L. E. Dike, J. Tien, D. E. Ingber and G. M. Whitesides, *Exp. Cell Res.*, 1997, 235, 305-313.

96. S. A. Ruiz and C. S. Chen, *Soft Matter*, 2007, 3, 168-177.

97. A. Perl, D. N. Reinhoudt and J. Huskens, *Adv. Mater.*, 2009, 21, 2257-2268.

98. O. Cherniavskaya, A. Adzic, C. Knutson, B. J. Gross, L. Zang, R. Liu and D. M. Adams, *Langmuir*, 2002, 18, 7029-7034.

99. S. Y. Chou, P. R. Krauss and P. J. Renstrom, *J. Vac. Sci. Technol., B*, 1996, 14, 4129-4133.

100. H. Schmitt, M. Zeidler, M. Rommel, A. J. Bauer and H. Ryssel, *Microelectron. Eng.*, 2008, 85, 897-901.

101. T. Haatainen, J. Ahopelto, G. Gruetzner, M. Fink and K. Pfeiffer, in *Emerging Lithographic Technologies Iv*, ed. E. A. Dobisz, 2000, vol. 3997, pp. 874-880.

102. H. Tan, A. Gilbertson and S. Y. Chou, *J. Vac. Sci. Technol., B*, 1998, 16, 3926-3928.

103. E. A. Costner, M. W. Lin, W.-L. Jen and C. G. Willson, in *Annu. Rev. Mater. Res.*, 2009, vol. 39, pp. 155-180.

104. S. H. Kim, K.-D. Lee, J.-Y. Kim, M.-K. Kwon and S.-J. Park, *Nanotechnology*, 2007, 18.

105. X. Q. Fan, H. H. Zhang, S. Liu, X. F. Hu and K. Jia, *Microelectron. J.*, 2006, 37, 121-126.

106. H. Cao, Z. N. Yu, J. Wang, J. O. Tegenfeldt, R. H. Austin, E. Chen, W. Wu and S. Y. Chou, *Appl. Phys. Lett.*, 2002, 81, 174-176.

107. B. K. Lee, H. Y. Lee, P. Kim, K. Y. Suh, J. H. Seo, H. J. Cha and T. Kawai, *Small*, 2008, 4, 342-348.

108. M. Escalante, Y. P. Zhao, M. J. W. Ludden, R. Vermeij, J. D. Olsen, E. Berenschot, C. N. Hunter, J. Huskens, V. Subramaniam and C. Otto, *J. Am. Chem. Soc.*, 2008, 130, 8892.

109. S. Y. Chou, P. R. Krauss, W. Zhang, L. J. Guo and L. Zhuang, *J. Vac. Sci. Technol., B*, 1997, 15, 2897-2904.

110. Y. Hirai, Y. Onishi, T. Tanabe, M. Nishihata, T. Iwasaki, H. Kawata and Y. Iriye, *J. Vac. Sci. Technol., B*, 2007, 25, 2341-2345.

111. N. Bogdanski, M. Wissen, S. Moellenbeck and H.-C. Scheer, *Microelectron. Eng.*, 2008, 85, 825-829.

112. W.-c. Liao and S. L.-C. Hsu, *Nanotechnology*, 2007, 18, 065303.

113. J. Haisma, M. Verheijen, K. vandenHeuvel and J. vandenBerg, *J. Vac. Sci. Technol. B*, 1996, 14, 4124-4128.

114. M. Colburn, S. Johnson, M. Stewart, S. Damle, T. Bailey, B. Choi, M. Wedlake, T. Michaelson, S. V. Sreenivasan, J. Ekerdt and C. G. Willson, in *Emerging Lithographic Technologies Iii, Pts 1 and 2*, ed. Y. Vladimirsky, 1999, vol. 3676, pp. 379-389.

115. M. Colburn, I. Suez, B. J. Choi, M. Meissl, T. Bailey, S. V. Sreenivasan, J. G. Ekerdt and C. G. Willson, *J. Vac. Sci. Technol., B*, 2001, 19, 2685-2689.

116. D. Bratton, D. Yang, J. Dai and C. K. Ober, *Polym. Adv. Technol.*, 2006, 17, 94-103.

117. H.-J. Lee, H. W. Ro, C. L. Soles, R. L. Jones, E. K. Lin, W.-l. Wu and D. R. Hines, *J. Vac. Sci. Technol., B*, 2005, 23, 3023-3027.

118. M. T. Abramo, E. B. Roy and S. M. LeCours, 1992.

119. N. Gadegaard and D. McCloy, *Microelectron. Eng.*, 2007, 84, 2785-2789.

120. C. M. Sotomayor Torres, S. Zankovych, J. Seekamp, A. P. Kam, C. Clavijo Cedeño, T. Hoffmann, J. Ahopelto, F. Reuther, K. Pfeiffer, G. Bleidiessel, G. Gruetzner, M. V. Maximov and B. Heidari, *Mater. Sci. Engin. C*, 2003, 23, 31.

121. E. Delamarche, B. Michel, C. Gerber, D. Anselmetti, H. J. Guentherodt, H. Wolf and H. Ringsdorf, *Langmuir*, 1994, 10, 2871.

122. D. K. Schwartz, *Annu. Rev. Phys. Chem.*, 2001, 52, 107-137.

123. R. G. Nuzzo and D. L. Allara, *J. Am. Chem. Soc*, 1983, 105, 4483.

124. J. Sagiv, *J. Am. Chem. Soc.*, 1980, 102, 92-98.

125. C. D. Bain, E. B. Troughton, Y. T. Tao, J. Evall, G. M. Whitesides and R. G. Nuzzo, *J. Am. Chem. Soc*, 1989, 111, 335.

126. M. Mrksich and G. M. Whitesides, *Annu. Rev. Biophys. Biomol. Struct.*, 1996, 25, 55-78.

127. J. Huang and J. C. Hemminger, *J. Am. Chem. Soc*, 1993, 115, 3343.

128. R. Banga, J. Yarwood, A. M. Morgan, B. Evans and J. Kells, *Langmuir*, 1995, 11, 4399.

129. H. Hoffmann, U. Mayer and A. Krischanitz, *Langmuir*, 1995, - 11, - 1312.

130. D. L. Angst and G. W. Simmons, *Langmuir*, 1991, - 7, - 2242.

131. J. Y. Kim, P. Seidler, L. S. Wan and C. Fill, *J. Colloid Interf. Sci.*, 2009, 329, 114-119.

132. M. J. Stevens, *Langmuir*, 1999, 15, 2773.

133. P. Silberzan, L. Leger, D. Ausserre and J. J. Benattar, *Langmuir*, 1991, 7, 1651.

134. N. Rozlosnik, M. C. Gerstenberg and N. B. Larsen, *Langmuir*, 2003, 19, 1182-1188.

135. C. P. Tripp and M. L. Hair, *Langmuir*, 1992, 8, 1126.

136. I. Haller, *J. Am. Chem. Soc*, 1978, 100, 8055.

137. J. B. Pendry, *Phys. Rev. Lett.*, 2000, 85, 3966-3969.

138. N. Fang, H. Lee, C. Sun and X. Zhang, *Science*, 2005, 308, 534-537.

139. X. Zhang and Z. Liu, *Nat. Mater.*, 2008, 7, 435-441.

140. Z. Jacob, L. V. Alekseyev and E. Narimanov, *Opt. Express*, 2006, 14, 8247-8256.

141. Z. Liu, H. Lee, Y. Xiong, C. Sun and X. Zhang, *Science*, 2007, 315, 1686-1686.

142. Z. Wang, W. Guo, L. Li, B. Luk'yanchuk, A. Khan, Z. Liu, Z. Chen and M. Hong, *Nat Commun*, 2011, 2, 218.

143. E. T. F. Rogers, J. Lindberg, T. Roy, S. Savo, J. E. Chad, M. R. Dennis and N. I. Zheludev, *Nat. Mater.*, 2012, 11, 432-435.

144. J. G. White, W. B. Amos and M. Fordham, *J. Cell Biol.*, 1987, 105, 41-48.

145. S. W. Hell and J. Wichmann, *Opt. Lett.*, 1994, 19, 780-782.

146. T. A. Klar, S. Jakobs, M. Dyba, A. Egner and S. W. Hell, *Proc. Natl. Acad. Sci.*, 2000, 97, 8206-8210.

147. V. Westphal and S. W. Hell, *Phys. Rev. Lett.*, 2005, 94, 143903.

148. M. J. Rust, M. Bates and X. Zhuang, *Nature Methods*, 2006, 3, 793-795.

149. X. Zhuang, *Nature Photonics*, 2009, 3, 365-367.

150. M. Bates, B. Huang, G. T. Dempsey and X. Zhuang, *Science*, 2007, 317, 1749-1753.

151. L. Bergmans, P. Moisiadis, B. Van Meerbeek, M. Quirynen and P. Lambrechts, *International Endodontic Journal*, 2005, 38, 775-788.

152. B. Erickson, *Anal. Chem.*, 1997, 69, 749A-752A.

153. G. Binnig, H. Rohrer, C. Gerber and E. Weibel, *Appl. Phys. Lett.*, 1982, 40, 178-180.

154. C. J. Chen, *Introduction to Scanning Tunneling Microscopy*, Oxford University Press, 1993.

155. G. Binnig, C. F. Quate and C. Gerber, *Phys. Rev. Lett.*, 1986, 56, 930.

156. A. Lewis, M. Isaacson, A. Harootunian and A. Muray, *Ultramicroscopy*, 1984, 13, 227-231.

157. D. W. Pohl, W. Denk and M. Lanz, *Appl. Phys. Lett.*, 1984, 44, 651-653.

158. J. C. Vickerman, *Surface Analysis-The Principal Techniques*, John Wiley & Sons, 1997.

159. H. Takano, J. R. Kenseth, S.-S. Wong, J. C. O'Brie and M. D. Porter, *Chem. Rev.*, 1999, 99, 2845-2890.

160. A. de Lozanne, *Science*, 2001, 291, 2561-2562.

161. A. R. Burns and R. W. Carpick, *Appl. Phys. Lett.*, 2001, 78, 317-319.

162. S. Grafstrom and et al., *Nanotechnology*, 1993, 4, 143.

163. J. L. Wilbur, H. A. Biebuyck, J. C. MacDonald and G. M. Whitesides, *Langmuir*, 1995, 11, 825-831.

164. E. H. Synge, *Philosophical Magazine*, 1928, 6, 356-362.

165. E. H. Synge, *Philosophical Magazine*, 1931, 11, 65-80.

166. A. Lewis, M. Isaacson, A. Harootunian and A. Muray, *Ultramicroscopy*, 1984, 13, 227-231.

167. R. C. Dunn, *Chem. Rev.*, 1999, 99, 2891-2928.

168. E. T. Vandenberg, L. Bertilsson, B. Liedberg, K. Uvdal, R. Erlandsson, H. Elwing and I. Lundstrom, *J. Colloid Interface Sci.*, 1991, 147, 103-118.

169. K. R. Bhushan, C. DeLisi and R. A. Laursen, *Tetrahedron Lett.*, 2003, 44, 8585-8588.

170. S. A. A. Ahmad, L. S. Wong, E. Ul-Haq, J. K. Hobbs, G. J. Leggett and J. Micklefield, *J. Am. Chem. Soc.*, 2009, 131, 1513-1522.

171. K. Matyjaszewski, P. J. Miller, N. Shukla, B. Immaraporn, A. Gelman, B. B. Luokala, T. M. Siclovan, G. Kickelbick, T. Vallant, H. Hoffmann and T. Pakula, *Macromolecules*, 1999, 32, 8716-8724.

172. R. l. Barbey, L. Lavanant, D. Paripovic, N. Schuwer, C. Sugnaux, S. Tugulu and H.-A. Klok, *Chem. Rev.*, 2009, 109, 5527.

173. M. Husseman, E. E. Malmström, M. McNamara, M. Mate, D. Mecerreyes, D. G. Benoit, J. L. Hedrick, P. Mansky, E. Huang, T. P. Russell and C. J. Hawker, *Macromolecules*, 1999, 32, 1424-1431.

174. J. F. Watts and J. Wolstenholme, *An Introduction to Surface Analysis by XPS and AES*, Wiley, 2003.

175. J. Shi, J. Chen and P. S. Cremer, *J. Am. Chem. Soc.*, 2008, 130, 2718.

176. R. Maoz, E. Frydman, S. R. Cohen and J. Sagiv, *Adv. Mater.*, 2000, 12, 424.

177. S. Walbert, W. Pfleiderer and U. E. Steiner, *Helv. Chim. Acta*, 2001, 84, 1601-1611.

178. C. G. Bochet, *J. Chem. Soc., Perkin Trans. 1*, 2002, 125-142.

179. B. D. Ratner and S. J. Bryant, *Annu. Rev. Biomed. Eng.*, 2004, 6, 41-75.

180. R. S. Kane, P. Deschatelets and G. M. Whitesides, *Langmuir*, 2003, 19, 2391.

181. L. Li, S. Chen, J. Zheng, B. D. Ratner and S. Jiang, *J. Phys. Chem. B*, 2005, 109, 2934-2941.

182. S. J. Sofia, V. Premnath and E. W. Merrill, *Macromolecules*, 1998, 31, 5059-5070.

183. A. A. Brown, N. S. Khan, L. Steinbock and W. T. S. Huck, *Eur. Polym. J.*, 2005, 41, 1757-1765.

184. H. W. Ma, D. J. Li, X. Sheng, B. Zhao and A. Chilkoti, *Langmuir*, 2006, 22, 3751-3756.

185. H. W. Ma, M. Wells, T. P. Beebe and A. Chilkoti, *Adv. Funct. Mater.*, 2006, 16, 640-648.

186. J. D. Jeyaprakash, S. Samuel, R. Dhamodharan and J. Ruhe, *Macromol. Rapid Commun.*, 2002, 23, 277-281.

187. W. J. Brittain and S. Minko, *Journal of Polymer Science Part a-Polymer Chemistry*, 2007, 45, 3505-3512.

188. L. Wenning, M. Muller and K. Binder, *Europhys. Lett.*, 2005, 71, 639-645.

189. T. Wu, K. Efimenko and J. Genzer, *J. Am. Chem. Soc.*, 2002, 124, 9394-9395.

190. T. Wu, K. Efimenko, P. Vlcek, V. Subr and J. Genzer, *Macromolecules*, 2003, 36, 2448-2453.

191. D. M. Jones, A. A. Brown and W. T. S. Huck, *Langmuir*, 2002, 18, 1265-1269.

192. S. Edmondson, V. L. Osborne and W. T. S. Huck, *Chem. Soc. Rev.*, 2004, 33, 14-22.

193. M. Beier and J. D. Hoheisel, *Nucleic Acids Res.*, 2000, 28, E11-E11.

194. W. Eck, V. Stadler, W. Geyer, M. Zharnikov, A. Golzhauser and M. Grunze, *Adv. Mater.*, 2000, 12, 805-808.

195. A. Golzhauser, W. Eck, W. Geyer, V. Stadler, T. Weimann, P. Hinze and M. Grunze, *Adv. Mater.*, 2001, 13, 806.

196. R. N. Wenzel, *J. Phys. Colloid Chem.*, 1949, 53, 1466-1467.

197. D. Quéré, *Physica A*, 2002, 313, 32-46.

198. H. Sugimura, N. Saito, N. Maeda, I. Ikeda, Y. Ishida, K. Hayashi, L. Hong and O. Takai, *Nanotechnology*, 2004, 15, S69-S75.

199. S. A. Ahmad, G. J. Leggett, A. Hucknall and A. Chilkoti, *Biointerphases*, 2011, 6, 8-15.

200. D. Briggs, *Surface Analysis of Polymers by XPS and Static SIMS*, Cambridge, 1998.

201. B. D. Beake and G. J. Leggett, *Langmuir*, 1999, 16, 735-739.

202. G. J. Leggett, N. J. Brewer and K. S. L. Chong, *PCCP*, 2005, 7, 1107-1120.

203. F. Meiners, I. Plettenberg, J. Witt, B. Vaske, A. Lesch, I. Brand and G. Wittstock, *Anal. Bioanal. Chem.*, 2013, 405, 3673-3691.

204. N. Ballav, A. Terfort and M. Zharnikov, *Langmuir*, 2009, 25, 9189-9196.

205. A. Turchanin, M. Schnietz, M. El-Desawy, H. H. Solak, C. David and A. Goelzhaeuser, *Small*, 2007, 3, 2114-2119.

206. G. Tizazu, O. El-Zubir, S. R. J. Brueck, D. G. Lidzey, G. J. Leggett and G. P. Lopez, *Nanoscale*, 2011, 3, 2511-2516.

207. A. S. Blawas and W. M. Reichert, *Biomaterials*, 1998, 19, 595-609.

208. G. Y. Liu and N. A. Amro, *Proc. Natl. Acad. Sci. U.S.A.*, 2002, 99, 5165-5170.

209. R. E. Ducker, S. Janusz, S. Sun and G. J. Leggett, *J. Am. Chem. Soc.*, 2007, 129, 14843.

210. G. Tizazu, O. el Zubir, S. Patole, A. McLaren, C. Vasilev, D. J. Mothersole, A. Adawi, C. N. Hunter, D. G. Lidzey, G. P. Lopez and G. J. Leggett, *Biointerphases*, 2012, 7.

211. S. A. A. Ahmad, L. S. Wong, E. ul-Haq, J. K. Hobbs, G. J. Leggett and J. Micklefield, *J. Am. Chem. Soc.*, 2011, 133, 2749-2759.

212. S. A. Ahmad, A. Hucknall, A. Chilkoti and G. J. Leggett, *Langmuir*, 2010, 26, 9937-9942.

213. R. Chelmowski, A. Prekelt, C. Grunwald and C. Woll, *J. Phys. Chem. A*, 2007, 111, 12295-12303.

214. D. J. Zhou, X. Z. Wang, L. Birch, T. Rayment and C. Abell, *Langmuir*, 2003, 19, 10557-10562.

215. J. D. Hoff, L. J. Cheng, E. Meyhofer, L. J. Guo and A. J. Hunt, *Nano Lett.*, 2004, 4, 853-857.

216. D. Falconnet, D. Pasqui, S. Park, R. Eckert, H. Schift, J. Gobrecht, R. Barbucci and M. Textor, *Nano Lett.*, 2004, 4, 1909-1914.

217. S. N. Frank and A. J. Bard, *J. Phys. Chem.*, 1977, 81, 1484-1488.

218. R. Wang, K. Hashimoto, A. Fujishima, M. Chikuni, E. Kojima, A. Kitamura, M. Shimohigoshi and T. Watanabe, *Nature*, 1997, 388, 431-432.

219. R. Thiruvenkatachari, S. Vigneswaran and I. S. Moon, *Korean J. Chem. Eng.*, 2008, 25, 64-72.

220. H. Haick and Y. Paz, *J. Phys. Chem. B*, 2001, 105, 3045-3051.

221. J. Augustynski, *Electrochim. Acta*, 1993, 38, 43-46.

222. S. S. Dinachali, M. S. M. Saifullah, R. Ganesan, E. S. Thian and C. He, *Adv. Funct. Mater.*, 2013, 23, 2201-2211.